ILMATIETEEN LAITOS
METEOROLOGISKA INSTITUTET
FINNISH METEOROLOGICAL INSTITUTE

155
CONTRIBUTIONS

METEOROLOGICAL CONDITIONS AFFECTING RENEWABLE ENERGY

MINTTU TUONONEN

FINNISH METEOROLOGICAL INSTITUTE
CONTRIBUTIONS

No. 155

METEOROLOGICAL CONDITIONS AFFECTING RENEWABLE ENERGY

Minttu Tuononen

Institute for Atmospheric and Earth System Research / Physics
Faculty of Science
University of Helsinki
Helsinki, Finland

ACADEMIC DISSERTATION in meteorology

To be presented, with the permission of the Faculty of Science of the University of Helsinki, for public criticism in auditorium A110, Chemicum, A. I. Virtasen aukio 1, on November 8th, 2019, at 12 noon.

Finnish Meteorological Institute
Helsinki, 2019

Supervisors Tenure-track professor Ewan O'Connor, Ph.D.
Atmospheric Composition Research
Finnish Meteorological Institute, Finland

Docent Victoria Sinclair, Ph.D.
Institute for Atmospheric and Earth System Research
University of Helsinki, Finland

Professor Heikki Järvinen, Ph.D.
Institute for Atmospheric and Earth System Research
University of Helsinki, Finland

Reviewers Professor Ian Brooks, Ph.D.
Institute for Climate & Atmospheric Science
University of Leeds, United Kingdom

Doctor Frank Beyrich, Ph.D.
Deutscher Wetterdienst
Meteorologisches Observatorium Lindenberg, Germany

Custos Professor Heikki Järvinen, Ph.D.
Institute for Atmospheric and Earth System Research
University of Helsinki, Finland

Opponent Professor Gunilla Svensson, Ph.D.
Department of Meteorology
Stockholm University, Sweden

ISBN 978-952-336-082-2 (paperback)
ISBN 978-952-336-083-9 (pdf)
ISSN 0782-6117

Edita Prima Oy
Helsinki 2019

ILMATIETEEN LAITOS
METEOROLOGISKA INSTITUTET
FINNISH METEOROLOGICAL INSTITUTE

Published by Finnish Meteorological Institute
(Erik Palménin aukio 1), PL 503
00101 Helsinki

Series title, number and report code of publication
Finnish Meteorological Institute
Contributions 155, FMI-CONT-155
Date October 2019

Author
Minttu Tuononen

Title
Meteorological conditions affecting renewable energy

Abstract

Synoptic situation and different meteorological phenomena can highly affect renewable energy production. Investigating different phenomena will give new information on the occurrence and characteristics of specific phenomena and their impacts on renewable energy applications. Different observational data sets and numerical models can be widely used in different phases of renewable energy projects; from planning of the project to help with the operation and the maintenance of the existing wind or solar field.

In this thesis a meteorological phenomena, a low-level jet, is investigated. Thesis comprises analysis of the climatological occurrence of low-level jets, their characteristics and forcing mechanisms, as well as numerical model capability to capture the phenomena. In addition, solar radiation forecasts obtained from the operational numerical weather prediction model are evaluated and the role of cloud cover forecast skill in solar radiation forecast error is investigated. Long data sets of observational data: mainly Doppler wind lidar, ceilometer, and solar radiation observations, are used, in addition to reanalysis and operational numerical weather prediction model data.

A low-level jet is a wind phenomenon that can affect wind energy production. Nighttime low-level jets are a commonly known boundary-layer phenomenon occurring during stably stratified conditions over flat terrain. In this thesis, new information on the occurrence, characteristics, and forcing mechanisms of a low-level jet was gained in different conditions: in Northern Hemisphere mid-latitude and polar regions based on reanalysis data and at two different sites in Finland and Germany based on long-term Doppler lidar observations. The low-level jet identification algorithms developed in these studies can be used to repeat the studies by using different models covering different areas or at any site operating a Doppler lidar. The low-level jet identification algorithm for Doppler lidar data can also be applied to operationally detect low-level jets, which is useful information for example from wind energy point-of-view.

Solar radiation and cloud cover forecasts were evaluated at one site in Finland based on long time-series of solar radiation and ceilometer observations. The role of cloud cover forecast in solar radiation forecast error is investigated. The solar radiation and cloud cover forecasts were obtained from operational numerical weather prediction model that can be used to predict the expected power production at solar field day-ahead. It was found that there is a positive bias in the forecast incoming solar radiation even if the cloud cover forecast is correct. The study can guide model improvements as the bias is likely due to underestimation in the forecast cloud liquid water content or incorrect representation of cloud optical properties. The methods created in this study can be applied to hundreds of sites globally. In addition, the algorithms developed in this study can be further used in different applications in the field of renewable energy, for example to detect potential in-cloud icing conditions.

Publishing unit
Finnish Meteorological Institute

Classification (UDC)	Keywords
551.521 551.55	Wind energy, solar energy, low-level jet, clouds, solar radiation, algorithm, remote sensing, Doppler lidar, ceilometer, numerical models, reanalysis

ISSN and series title
0782-6117 Finnish Meteorological Institute Contributions

ISBN	Language	Pages
ISBN 978-952-336-082-2 (paperback), 978-952-336-083-9 (pdf)	English	113

ILMATIETEEN LAITOS
METEOROLOGISKA INSTITUTET
FINNISH METEOROLOGICAL INSTITUTE

Julkaisija
Ilmatieteen laitos
(Erik Palménin aukio 1), PL 503
00101 Helsinki

Julkaisun sarja, numero ja raporttikoodi
Finnish Meteorological Institute
Contributions 155, FMI-CONT-155
Julkaisuaika Lokakuu 2019

Tekijä
Minttu Tuononen

Nimike
Meteorologisten ilmiöiden vaikutuksista uusiutuvaan energiaan

Tiivistelmä

Vallitseva säätila ja paikalliset meteorologiset ilmiöt voivat selvästi vaikuttaa tietyllä alueella havaittavaan tuulisuuteen ja pilvisyyteen ja näin ollen mahdollisen tuuli- tai aurinkoenergian tuotantoon. Meteorologisia ilmiöitä tutkimalla saadaan lisätietoa niiden esiintyvyydestä ja ominaisuuksista, ja tätä tietoa voidaan edelleen käyttää ilmiöiden vaikutusten arviointiin uusiutuvan energian näkökulmasta. Erilaisia meteorologisia havaintoaineistoja ja numeerisia malleja voidaan hyödyntää uusiutuvan energian käyttöön tähtäävän projektin eri vaiheissa mahdollisen uuden tuuli- tai aurinkovoimalan suunnittelusta olemassa olevan voimalan operatiivisen toiminnan tukemiseen.

Tässä väitöskirjatutkimuksessa on tarkasteltu uusiutuvan energian tuotantoon vaikuttavan meteorologisen ilmiön, alatroposfäärin suihkuvirtauksen, esiintyvyyttä, ominaisuuksia, syntymekanismeja sekä numeerisen mallin kyvykkyyttä ilmiön mallintamisessa. Lisäksi tutkittiin operatiivisen sääennustusmallin kyvykkyyttä auringonsäteilyn ja pilvisyyden ennustamisessa sekä pilvisyysennusteiden roolia säteilyennusteiden ennustevirheissä. Väitöskirjassa on käytetty pitkiä meteorologisia havaintosarjoja: Doppler lidar -tuulimittauksia, ceilometrillä tuotettuja pilvisyysmittauksia, säteilyhavaintoja, sekä numeerilla malleilla tuotettuja aineistoja: uusanalyysiä ja operatiivisen sääennustusmallin tuottamia säteily- ja pilvisyysennusteita.

Alatroposfäärin suihkuvirtaus on tuuli-ilmiö, joka on yleisesti tunnettu erityisesti stabiilin yöllisen rajakerroksen tilanteessa. Ilmiötä on tämän väitöskirjan osatutkimuksissa tutkittu numeerisen mallin ja laajan havaintoaineiston yhdistelmän, uusanalyysin, perusteella pohjoisen pallonpuoliskon keskileveys- ja napa-alueella, sekä kahdella eri mittausasemalla Doppler lidar -tuulimittausten perusteella. Tutkimuksissa havaittiin, että alatroposfäärin suihkuvirtaus esiintyy usein modernien tuuliturbiinien vaikutusalueella lisäten turbulenssin aiheuttamaa stressiä, sekä paikallisesti alueilla, joilla ilmiötä ei ole aiemmin tutkittu. Tutkimuksissa kehitettyjen algoritmien avulla alatroposfäärin suihkuvirtauksien tutkiminen ja operatiivinen havainnoiminen on mahdollista aiempaa laajemmassa mittakaavassa Doppler lidar -havaintoja käyttäen.

Pilvisyysennusteiden vaikutusta auringonsäteilyennusteisiin tutkittiin käyttämällä pitkiä havaintosarjoja pilvisyydestä ja auringonsäteilystä, ja vertaamalla havaintoja operatiivisiin pilvisyys- ja säteilyennusteisiin. Tutkimuksessa selvitettiin kuinka hyvin säteily- ja pilvisyysennusteet toteutuvat yhdellä mittausasemalla Suomessa. Oikein ennustetuissa pilvisyystilanteisssa havaittiin positiivinen ennustevirhe maan pinnalle saapuvassa auringonsäteilyssä. Todennäköinen syy tähän positiiviseen säteilyennustevirheeseen liittyy pilvien vesisisällön aliarvioimiseen tai heikkouksiin pilvien optisten ominaisuuksien mallintamisessa. Tutkimuksessa kehitettyjen menetelmien avulla on mahdollista laajentaa tutkimus koskemaan satoja mittauasemia ympäri maailmaa.

Julkaisijayksikkö
Ilmatieteen laitos

Luokitus (UDK)
551.521
551.55

Asiasanat
Tuulienergia, aurinkoenergia, alatroposfäärin suihkuvirtaus, pilvet, auringon säteily, algoritmi, kaukokartoitus, Doppler lidar, ceilometri, numeeriset mallit, uusanalyysi

ISSN ja avainnimike
0782-6117 Finnish Meteorological Institute Contributions

ISBN
ISBN 978-952-336-082-2 (nid.), 978-952-336-083-9 (pdf)

Kieli
Englanti

Sivumäärä
113

Preface

I want to thank my supervisors Ewan O'Connor and Victoria Sinclair - without you this thesis would have never happened. Victoria, thanks for believing me since the very beginning of my studies and encouraging me during all of the difficulties. Ewan, thanks for continuous support and hours spent to help and educate me. Thanks for fun moments. I thank my other co-authors Timo Vihma and Ville Vakkari for all of the help and discussions. Thank you Tobias Marke for working with me. Thanks for other colleagues for all of the support and discussions in science-related matters.

I want to thank Lauri Laakso for taking me in his group jointly with Eija Asmi in 2015 when I started my PhD work. I thank Antti Hyvärinen for letting me focus on my PhD research and for continuously supporting my work. I want to thank Finnish Meteorological Institute (FMI) for offering me everything I needed to conduct this research. I am grateful for Juha Paldanius and Samuli Laukkanen from Vaisala for taking me into their groups and supporting with the beginning, continuing and finishing my PhD. I thank Maj & Tor Nessling foundation for supporting my PhD research over three years. In addition, I thank FMI, University of Helsinki, and Vaisala for financially supporting many inspiring travels to participate in courses, and to show my results and to meet talented scientists in international conferences.

I am highly grateful to Gunilla Svensson to be as an opponent for my thesis, Heikki Järvinen to serve as a custos and Ian Brooks and Frank Beyrich for pre-examining this thesis.

I sincerely thank my friends at FMI, University of Helsinki and Vaisala for continuous peer-support and lighting my working days. You have always been one of the most important source of strength to continue this process. I want to thank my family and beloved friends for all of the support and love. I want to thank my parents for always encouraging me to study and my father for reminding me that *"opissa se on variksenpoika tuulessa"*. Thanks Merri for endless walks where countless practical issues were figured out.

Finally, I do not have enough words for the most important people in my life - those who continuously believed in me, no matter what, and even when I did not.
Thank you.

Minttu Tuononen
Helsinki, April 2019

Contents

List of original publications

I Tuononen, M., Sinclair, V. A., and Vihma, T., 2015: A climatology of low-level jets in the mid-latitudes and polar regions of the Northern Hemisphere. *Atmospheric Science Letters*, **16**, 492–499, doi:10.1002/asl.587

II Tuononen, M., O'Connor, E. J., Sinclair, V. A., and Vakkari, V., 2017: Low-level jets over Utö, Finland, based on Doppler lidar observations. *Journal of Applied Meteorology and Climatology*, **56**, 2577–2594, doi:10.1175/JAMC-D-16-0411.1

III Marke, T., Crewell, S., Schemann, V., Schween, J. H., and Tuononen, M., 2018: Long-term observations and high-resolution modeling of midlatitude nocturnal boundary layer processes connected to low-level jets. *Journal of Applied Meteorology and Climatology*, **57**, 1155–1170, doi:10.1175/JAMC-D-17-0341.1

IV Tuononen, M., O'Connor, E.J., Sinclair, V.A., 2019: Evaluating solar radiation forecast uncertainty, *Atmospheric Chemistry and Physics*, **19**, 1985–2000, doi:10.5194/acp-19-1985-2019

List of acronyms

ASR Arctic System Reanalysis

DBS Doppler Beam Swinging

ECMWF European Center for Medium Range Weather Forecasts

DHI Diffuse Horizontal Irradiance

DNI Direct Normal Irradiance

GOS Global Observing System

GHI Global Horizontal Irradiance

IFS Integrated Forecast System

IPCC Intergovernmental Panel on Climate Change

IRENA International Renewable Energy Agency

LES Large-Eddy Simulation

LIDAR Light Detection and Ranging

LLJ Low-Level Jet

LWP Liquid Water Path

NWP Numerical Weather Prediction

ME Mean Error

TOA Top Of Atmosphere

SODAR Sound Detection and Ranging

VAD Velocity Azimuthal Display

1. Introduction

Climate change has increased the attention towards renewable energy. The Paris agreement set an ambitious goal to the world's nations, which is to limit the global mean 2 m temperature increase to well below 1.5°C, thus pursuing the path of effectively limiting greenhouse gas emissions. According to the Intergovernmental Panel on Climate Change (IPCC), the global net anthropogenic CO_2 emissions should reach net-zero around 2050 to limit the global mean warming at the surface to 1.5°C above pre-industrial levels (IPCC, 2018). To reach the net-zero level, the use of fossil fuels should be substituted with cleaner energy production, including renewable energy sources.

After hydropower, the main renewable energy sources are wind and solar (IRENA, 2019). Wind is converted to electricity by wind turbines where the kinetic energy of wind (air flow) is turned to mechanical power by the rotating wind turbine blades and furthermore to electricity by the generator of the wind turbine. Solar energy, in turn, is converted to electricity by solar panels (photovoltaic effect) or heat by concentrating the sunlight with mirrors or lenses. According to the International Renewable Energy Agency (IRENA), the installed wind and solar energy capacities globally at the end of 2018 were 564 GW and 486 GW, respectively, with consistently growing trend over time (IRENA, 2019).

Both wind and solar resources are highly variable and dependent on geographical location, season, time-of-day and weather. Atmospheric science is a crucial scientific field when discussing wind and solar energy. It includes atmospheric physics and chemistry, climatology and meteorology – all being important and closely related to each other when trying to understand the highly variable nature of wind and solar resources. Wind and solar energy resources can be estimated by using meteorological knowledge, meteorological observations and numerical weather prediction models. In addition, the understanding of meteorological conditions and phenomena helps with estimating weather-related risks affecting renewable energy projects, comprising both safety and profitability aspects.

The focus of this thesis is on renewable energy meteorology. The general aim of this thesis has been to increase our understanding on how different meteorological conditions affect wind and solar energy. This general aim is addressed in four research articles, through more specific research questions and aims:

1. **Low-level jets are a potentially valuable wind resource but they may also harm the wind turbines. How well can we observe and characterise low-level jets, and can we map this resource using reanalysis data?**
   In papers I-III, the aim was to derive a climatology of low-level jets based

on reanalysis data (paper I) and Doppler lidar observations (papers II, III). Automated algorithms were developed and applied to data in papers I, II, and III to objectively identify low-level jets from gridded reanalysis output, and high temporal and vertical resolution Doppler wind lidar observations, also enabling real-time detection. The occurrence and characteristics of low-level jets were investigated in papers I-III.

2. **The amount of clouds and incoming solar radiation are highly variable in nature. How well can operational numerical weather prediction model predict clouds and incoming solar radiation at the surface?**
   In paper IV algorithms were created for ceilometer data to detect liquid cloud layers, ice clouds, precipitation and fog. The aim was to evaluate the operational short-term cloud cover and solar radiation forecasts by comparing day-ahead forecasts of cloud cover and surface solar radiation against ceilometer and pyranometer observations.

3. **How observational systems can help numerical weather prediction model development?**
   The aim has been to create automated algorithms that are easily applicable to different sites operating similar instruments. A detailed comparison of model output to quality-controlled observations are needed for model evaluation, and furthermore model development. The model evaluation may reveal deficiencies of a model's capability to represent specific conditions accurately and these aspects are discussed in all papers.

The introduction to this thesis is structured as follows: in section 2 the background of this thesis is discussed. Data and methods used in this thesis are briefly described in section 3 followed by the main results in section 4. Section 5 contains the review of papers and author's contribution. Finally, the discussion and conclusions are presented in section 6. The four published papers are printed in order of their publication at the end of this thesis.

2. Background

2.1. Renewable energy meteorology

The energy received from the sun drives the Earth's renewable energy sources. The amount of solar radiation received at the top of the atmosphere depends on the Earth's tilt towards the sun, and in addition, the amount of solar energy received at the surface depends on the solar radiation absorbed and reflected by the clouds and the atmospheric gases and aerosols. The uneven distribution of sunlight at the Earth's surface and the rotation of the Earth result in differences in atmospheric pressure and consequently large-scale atmospheric circulation. Although windiness depends fundamentally on the large-scale circulation, local effects, such as topography and coastal effects also affect the wind field and are important in determining the local wind resources.

As renewable energy resources are highly variable in nature, it is crucial for renewable energy applications to determine and understand the local wind and solar resources and how different meteorological conditions affect them. Long-term variability (yearly and monthly variation) must be determined in the planning phase of a renewable energy project and short-term variability (diurnal and hourly variation) must be known for the operational purposes. These can be obtained by using different meteorological data: long-term meteorological observations and reanalyses for long-term variability, and real-time observations and forecast models for short-term variability.

There are different meteorological conditions that affect the available amount of wind and solar resources. For example, the increased wind speed due to favorable atmospheric conditions may ramp up the wind energy production locally. Similarly, clear-sky periods due to high pressure situations are favorable conditions for solar energy production resulting in more available solar energy. In addition, different meteorological conditions, such as atmospheric icing and increased wind shear and turbulence, may harm the equipment, for example decreasing the life time of wind turbines. Therefore, the occurrence and characteristics of meteorological phenomena affecting renewable energy is crucial to understand before the design and construction of a new renewable energy project. Meteorological conditions and different phenomena determine and influence the selection of the site location, what equipment to be used (such as turbine type), and layout of the project, but also the operation of the existing wind or solar site.

2.2. Meteorological data in renewable energy

Different meteorological data sets can be widely utilized in different phases of the renewable energy projects. For instance, accurate site assessment is required before building a wind or solar farm to ensure the profitability of the project. In the operational phase of the existing wind or solar energy site, accurate wind or solar radiation forecasts and real-time observations are requested. Therefore, a range of different data sets are required. This includes gridded meteorological data which resolve large-scale phenomena as well as site specific observations of relevant meteorological variables. The optimum data set for each application highly depends on the application, for example on the required accuracy and desired length of the data set.

Observations

The Global Observing System (GOS), guided and coordinated by the World Meteorological Organization, and operated on a national and international level, provides an extensive amount of meteorological observations of the atmosphere and ocean surface. Every day, billions of observations – including data from traditional in-situ point observations, single-profile measurements (radiosoundings and ground-based remote sensing), more complex profiling (cloud radars and weather radars), satellite-based remote sensing, ships and aircraft – are gathered, stored and used. Meteorological observations play a fundamental role in Numerical Weather Prediction (NWP) as they are used in determining the initial condition of the atmosphere that is necessary for obtaining accurate forecasts ahead in time. Meteorological observations are also used in NWP model development, and in monitoring the real-time conditions and obtaining advisory and warning systems of weather-related conditions.

Different observational data sets are used across a wide range of renewable energy applications. For example the accurate resource assessment of incoming solar radiation at a specific site requires at least one year of quality-controlled solar radiation measurements to determine the seasonal variation. However, preferably, several years of observations should be used to understand the year-to-year variation. Solar radiation at the surface is typically measured with in-situ pyranometers and pyrheliometers, to obtain all of the solar radiation components usable in solar energy applications: Global Horizontal Irradiance (GHI), Direct Normal Irradiance (DNI) and Diffuse Horizontal Irradiance (DHI).

The same requirement for long observational data sets described above for solar energy applications applies to wind energy applications. Wind measurements are conventionally done with wind sensors located at different heights on a meteorological

mast, using different in-situ wind sensors: cup anemometers and wind vanes or sonic anemometers. However, the wind energy industry is moving towards the use of ground-based remote sensing instruments to obtain wind profile measurements with higher temporal and vertical resolution, especially using Light Detection and Ranging (lidar) and Sound Detection and Ranging (sodar) instruments. In addition to improved vertical resolution over the appropriate height range of modern wind turbine, the lidar and sodar instruments are easy to relocate, which enables measurements from several locations, for example within the site. This is a huge advantage compared to conventional meteorological masts that are deployed in one location only and are in practise unprofitable to relocate.

Doppler lidars have become very popular in the field of wind energy (Banta et al., 2002; Pichugina et al., 2012; Hasager et al., 2013; Banta et al., 2013). The basic principle of a Doppler wind lidar in retrieving the wind profile is the detection of the movement of aerosol particles that are transported by the air flow. The movement detection relies on measuring the Doppler shift (shift in received versus transmitted laser frequency) when the transmitted laser signal is backscattered from the moving particles. One beam direction gives the line-of-sight velocity information and the wind speed and direction (three-dimensional quantity) is obtained by transmitting a laser beam in at least three different directions to resolve the three-dimensional wind vector. This calculation assumes horizontal homogeneity in the scanning volume. The wind field is usually not horizontally homogeneous which affects the data quality and the detection of moving particles requires aerosols to follow. The latter is a problem in clean conditions when there is not enough signal to retrieve the wind information. In addition, it should be kept in mind that the lidar signal attenuates in thick cloud layers, and no information is available above. These measurement principles result in limitations in terms of data availability.

Doppler lidars can obtain the wind profile by using different scanning schemes (Werner, 2005), for example using Velocity Azimuthal Display (VAD) or Doppler Beam Swinging (DBS) scans. The measurement volume and the vertical resolution of the wind profile is determined by the scan settings used, such as the elevation angle of the laser beam. The aspects of the desired vertical resolution, temporal resolution, data quality and measurement volume should be taken into account when determining the optimal scanning pattern of the instrument for each application.

The information obtained by transmitting a laser pulse and receiving the backscattered signal is also used in other meteorological applications than wind profile measurements. Cloud profiling can be done by using a simpler lidar system, a ceilometer. The detection of clouds with lidar ceilometer requires a light pulse pointed only into one direction, and it does not require Doppler shift detection. The cloud measurement relies on receiving the backscattered laser signal from the cloud droplets

and ice crystals. Ceilometers can also be used to detect the aerosol layers (and to obtain mixing layer height; Wiegner et al., 2014) and precipitation. Traditionally ceilometers are used at airports to detect the cloud base height and sky condition information, and therefore there is a dense network of ceilometers distributed around the world (Illingworth et al., 2019). This is a notable benefit compared to other cloud profiling instruments (such as cloud radars, research lidars) which are not as densely distributed. The limitation of ceilometers is that they usually see only up to the lowest liquid cloud layer, as the lidar signal attenuates rapidly when passing through a liquid cloud.

Obtaining profile data has advantages in the renewable energy field. For the wind energy industry, it is beneficial to obtain wind speed profiles up to several hundred meters above the surface, as the modern commercial wind turbine rotor diameter and hub height now exceed 160 m. For solar energy purposes, and especially observing clouds, profiling instruments (or a combination of them) are the most useful as more information on the cloud properties, such as presence of liquid cloud layers, can be obtained when using the attenuated backscatter profile information compared to traditional cloud base height and sky condition retrievals (Illingworth et al., 2007).

Numerical models

For the general public, the most well-known product from the field of meteorology is a weather forecast, produced by NWP models. NWP models are mathematical models where the evolution of the atmospheric state can be predicted through resolving the equations representing the atmospheric dynamic and thermodynamic state, and parameterizating the physical processes too small to be resolved, ahead in time. Dynamic and thermodynamic equations solve the atmospheric flow and thermodynamic state, whereas physical parameterizations are used to derive radiation, clouds, convection, turbulence, and other sub-grid size phenomena. NWP models can be used to produce a range of different forecasts and simulations from nowcasting to seasonal predictions and over a range of spatial scales from regional to global. For example, the European Centre for Medium-Range Weather Forecasts (ECMWF), produces medium-range forecasts twice a day with a forecast horizon of up to 15 days, extended-range forecasts twice a week up to 46 days and long-range forecasts once a month up to 7 months. There are global forecasting systems, such as the ECMWF Integrated Forecast System (IFS) model, and higher resolution regional NWP models covering a limited area, such as HIRLAM and HARMONIE. The grid resolution can vary considerably between different NWP models. For example, the spatial resolution of the operational IFS model is approximately 9 km and in the vertical there are 137 levels from ground to the top of atmosphere whereas HARMONIE-AROME has 2.5 km horizontal resolution and 65 vertical levels.

NWP models use real-time observations gathered through GOS to determine

the most realistic atmospheric state in a procedure called data assimilation. In this step, the model initial state is represented relying on the real-time measurements and given to the equations solving the atmospheric dynamic and thermodynamic state, and to forecast ahead in time. In the case of ensemble forecasts, the initial state is perturbed to get slightly different initial states for each ensemble member. The spread between the ensemble members can then be used to estimate the uncertainty of the prediction (probabilistic forecast). The deterministic forecast does not itself include any information on the probability. NWP models resolve the evolution of large-scale circulation, and synoptic and mesoscale features, i.e. they resolve the atmospheric flow and movements of frontal systems. However, they may not always capture small-scale phenomena correctly, such as coastal effects, due to the deficiencies in resolution or incorrect parameterization, resulting in decreased skill in predicting certain meteorological conditions. Overall, the skill of NWP models has been considerably improved with the increase in computational power allowing for a better grid resolution, improved parameterizations and the amount of real-time data (mainly satellite data) assimilated in to the model (Bauer et al., 2015).

In the field of renewable energy, NWP models can be used for example to predict the amount of incoming solar radiation for the day-ahead to guide the solar energy markets. Similarly, wind speed forecasts are used to predict the potential wind energy production over different time windows. Therefore, there are certain needs for the accuracy of the NWP model also in the renewable energy perspective.

Large-Eddy Simulation (LES) models are high-resolution numerical models that are used to resolve the turbulent flow with a range of time and length scales. In comparison to LES models, NWP models do not directly resolve the turbulent eddies, as the turbulent motions are parameterized. LES models can be used for research purposes to investigate different phenomena in detail over a certain area, for example in boundary-layer studies. However, as LES models require very high resolution in time and space, they are computationally extremely expensive. Therefore, LES models are not suitable for operational use. The information gained from LES can provide valuable information to deeply understand the physical processes that are acting, such as forcing mechanisms of a low-level jets or structure of clouds smaller than usual grid size.

Reanalysis

Reanalysis is a combination of meteorological observations and a numerical model, resulting in gridded data set covering areas from regional to global scales and typically spanning historical time windows of several decades. Reanalysis is produced by using a NWP model and adding the information content of historical meteorological observations in the data assimilation process. Thus, running the NWP model

over times when meteorological observations are available, and repeating the data assimilation process with all of the available observations for each time step and grid point, the resulting data set is seen as the best estimate of the state of the atmosphere in gridded form, possibly spanning the whole globe from ground to the top-of-atmosphere over tens of years. One of the advantages of reanalysis data is that they are produced based on the latest NWP model cycle (at the production time), thus the aim is to use the most skillful model for the whole historical time window, and incorporate more observations than are available for the operational forecast. Therefore, the reanalysis data is also free of changes due to NWP model development, i.e. increase in model's skill over time.

There are different reanalysis data sets covering the whole globe (e.g. ERA5, ERA-Interim, MERRA) and some limited area (e.g. COSMO-REA, ASR). The single-level and model-level variables can be obtained from any grid point and over a large time window, therefore enabling e.g. climatological studies investigating seasonal variations or trend analysis. The horizontal resolution may vary considerably between different data sets, usually being coarser for global data sets. For example, the newest global reanalysis dataset ERA5 by ECMWF (ERA5, 2019) has spatial resolution of 30 km with 137 vertical levels, and the newer version of ASR (ASRv2, Bromwich et al., 2018), covering limited area, has 15 km spatial resolution with 71 model levels. Most of the global reanalysis datasets span multiple decades, usually starting from 1979 (or before) to almost real-time with temporal resolutions varying from hourly to 3-hourly or coarser. Additionally, many of these data sets are freely available, which makes them easily accessible for wide usage.

In renewable energy applications, reanalysis can be used to estimate the incoming solar radiation at the surface, wind speed at different levels, as well as investigating relevant meteorological phenomena derived from the reanalysis output. Reanalysis data are useful for a wide range of applications; however, these data may not be suitable for detailed investigation of a phenomenon at a certain location due to the deficiencies in the temporal and spatial resolution.

Algorithms

An algorithm is a recipe or a decision tree which describes a process in a mathematical or logical form. Usually algorithms contain separate tasks that are solved by a computer. For example, a simple algorithm could find the number of hours when the averaged wind speed exceeds $10\,\mathrm{m\,s^{-1}}$ over the past two years. The power of algorithms is that they can process large sets of information and the results should, in principle, be objective as they can strictly follow the given relations or rules without suffering from human errors, therefore lacking subjective bias. Algorithms can easily process massive amounts of data with complicated relations, which would be an impossible task for a

human to analyse manually. Objectivity and capability to efficiently handle massive amounts of data with complicated connections are desirable features, for example, when the aim is to identify a certain meteorological condition by using multiple years of meteorological data.

At wind farms, the real-time wind measurements from the wind turbine nacelles are used to determine the estimated power production and to detect faulty conditions, e.g. due to atmospheric icing, by using simple algorithms. Other meteorological phenomena can be automatically identified based on the real-time observations with a set of rules by using more complicated algorithms, such as identification of a low-level jet by using wind profile observations or estimation of conditions causing wind turbine icing by using a combined information from different observational data sources and/or forecast data.

In contrast to real-time monitoring, algorithms can also be used to analyse historical data. When investigating over several years, the automated identification of a particular phenomenon or process is usually necessary. With algorithms applied to historical data (observations or model), it is possible to investigate the climatological behaviour of the feature of interest. This is desirable, for example, when estimating the impacts of certain phenomena on a renewable energy project – it is beneficial to understand the occurrence of hazardous phenomena when estimating the possible stresses that will be expected by the structures, for example wind turbines. In these cases, it is again required that large amounts of data can be objectively analysed.

Model evaluation

NWP models may not always represent the atmospheric conditions and different phenomena accurately. Hence, if only relying on model data, any inaccuracy in estimating turbulence would likely impact the estimated wind resource or the expected life-time of the wind turbines. As numerical models are needed for estimating renewable energy resources and other weather-related impacts, and for forecasting the amount of expected power production one day-ahead at any location, it is vital to know how accurate the NWP model is.

Different meteorological observations are used for model evaluation at the location of available measurement data. Especially long time series of observational data, with possible algorithms applied to investigate certain phenomena, are used for investigating the model's performance. To determine the accuracy of the model, the model must be systematically compared against observations by using large amount of data. Comparing model output with observations is not always a simple task, as the nature of model and observational data differ. NWP output is usually a representation of a condition in a grid-space, thus the forecast values represent averaged or instantaneous conditions over a certain area or volume. On the other hand,

observations may be a point measurement (for example traditional solar radiation observations by a pyranometer) or a measurement over a certain area (such as satellite-derived solar radiation data).

The accuracy of NWP models can be analysed by using a wide range of error metrics and skill scores (Casati et al., 2008). These represent the differences between the observations and forecast data, thus describing how well the forecast model is representing the real (observed) conditions. The model's skill in forecasting a certain condition may vary diurnally, seasonally or based on location. For example, it is known that a typical model's resolution may not be high enough to produce some local effects, such as coastal or mountainous effects, and that small-scale phenomena are harder to predict compared to large-scale effects. Some conditions have diurnal and seasonal variability and if the models have deficiencies in representing these conditions accurately, this may result in diurnal and/or seasonal variations in model's skill to predict a certain phenomenon.

2.3. Low-level jets, clouds and solar radiation

In this thesis, the focus has been on low-level jets that potentially affect wind energy, and on forecasts of low- and mid-level clouds that strongly affect solar radiation forecasts. Different meteorological data sets, from point measurements to profile observations to gridded reanalysis and NWP model data, are used. Additionally, methods and algorithms have been created which enable research at scales varying from an individual measurement site to networks with hundreds of sites operating certain instruments, and to global scales.

Low-level jets

A low-level jet (LLJ) is a localized maximum in the vertical profile of horizontal wind. LLJs typically occur in the lowest few hundred meters of the atmosphere, therefore being potentially important for wind energy (Banta et al., 2013). The increased wind speed related to the LLJ maximum can enhance wind power production but on the other hand the increased wind shear and turbulence can be harmful for wind turbines. In addition, LLJs have other implications, such as their impact on the development of severe weather, transport of moisture and gases (Higgins et al., 1997; Mao and Talbot, 2004; Hu et al., 2013), therefore affecting air quality, as well as impacts on marine and aviation safety due to increased wind shear. There are different LLJ forcing mechanisms, such as inertial oscillation in time (Blackadar, 1957) and space (Högström and Smedman-Högström, 1984; Smedman et al., 1993), barrier and katabatic winds (Parish, 1982; Renfrew and S. Anderson, 2006), large scale baroclinicity, and shallow baroclinicity induced by the coastlines or sea-ice edges

(Doyle and Warner, 1993; Savijärvi et al., 2005). Different forcing mechanisms have different impacts on the occurrence and characteristics of LLJs.

Low-level jets have been studied widely over flat land areas, especially over the Great Plains in the United States where a nocturnal LLJ is a common phenomenon, especially in the summer season (Banta et al., 2002; Storm et al., 2009; Vanderwende et al., 2015). These LLJs are usually forced by an inertial oscillation in time when the boundary layer transforms from daytime unstable stratification to nighttime stable stratification, and the upper part of the boundary layer decouples from the surface resulting in decayed friction and accelerated horizontal wind speed in the boundary layer. However, LLJs can also occur in cold regions, although the forcing mechanisms may be different. LLJs have been studied in the Arctic (Moore and Renfrew, 2005) and in the Antarctic (Andreas et al., 2000; Renfrew and S. Anderson, 2006), but overall, there are fewer studies focusing on wintertime LLJs. This acknowledged imbalance is partly covered in this thesis by deriving the wintertime climatology of LLJs based on the reanalysis data.

Different types of meteorological data sets discussed in the previous section have been used in LLJ research. LLJs have been investigated with long time series of gridded model data, such as reanalysis data sets (Rife et al., 2010; Ranjha et al., 2013). Reanalysis data enable the research of the phenomena over large areas and over long time periods. NWP models may not represent the LLJs correctly, possibly due to their inaccurate representation of the stable boundary layer showing too much turbulent mixing (Storm et al., 2009; Floors et al., 2013), or too coarse vertical and horizontal resolution. Therefore, in order to understand the phenomena, to estimate the effects of the phenomena on wind power production, and to evaluate the model performance, it is important to investigate the phenomena by using different data. In this thesis, the climatology of LLJs is investigated by using regional renanalysis data and at two different sites based on long time series of Doppler lidar observations with high temporal and vertical resolution.

In recent years, the growing interest in wind energy has also raised interest in LLJs in coastal areas (Tucker et al., 2010; Pichugina et al., 2012; Dörenkämper et al., 2015; Peña et al., 2016). In wind energy applications, the focus area is the lowest few hundred metres above the ground and long data sets of wind profile observations are needed to investigate the climatology of LLJs. There are no previous climatological studies of LLJs in Finnish coastal regions. Accurate representation of LLJs can be obtained from high temporal and vertical resolution wind profile observations, and furthermore used to evaluate the ability of a numerical model to capture them. LLJs should be investigated at more sites to understand the forcing mechanisms and to extend the model verification. These aspects are partly addressed in this thesis by the algorithm development, and by using Doppler lidar observations for investigating LLJs in the

Finnish Archipelago and in Germany, as well as comparing results from the reanalysis data and LES model to the observed LLJs.

Clouds and cloud properties

A cloud consists of liquid droplets, ice particles, or both, suspended in the air. There are different types of clouds in the atmosphere. Traditionally clouds are divided into ten main groups that can be separated into low-, mid- and high-level clouds. Clouds are highly variable; cloud heights typically vary from ground level up to approximately 15 km in altitude, and, as can be visually observed, have different sizes, shapes and structures, and vary in transparency. The cloud forcing mechanisms and atmospheric conditions determine the cloud properties.

As clouds consist of liquid and/or solid particles, the cloud optical properties highly depend on the constituents of a cloud. High clouds typically consist of ice particles only, being optically thinner than mixed-phase clouds or liquid clouds, that contain liquid droplets. Mixed-phase clouds contain a mixture of ice and supercooled droplets at temperatures below freezing, down to $-40°$C. For the same amount of water content ice clouds, mixed-phase clouds and pure liquid clouds show different optical properties, as ice particles are usually larger than liquid cloud droplets (Korolev et al., 2017).

NWP models forecast the cloud liquid/ice water contents at every model level for each grid point, from which the cloud fraction information at each grid point can be obtained. The single-level values of cloud cover for each layer (low, mid, high) as well as total cloud cover are derived from the forecast cloud liquid/ice water contents over the each layer and each model column. NWP models derive the cloud optical properties from the cloud liquid water and cloud ice water contents in each grid point. From these variables the cloud liquid water path and cloud ice water paths can be estimated, describing the total amount of cloud liquid and cloud ice water contents in one column. Extensive cloud profiling measurement stations are sparsely located, and therefore the comprehensive evaluation of a model's skill in predicting clouds is only done at a few ground-based sites (Illingworth et al., 2007; Hogan et al., 2009) or from profiling satellites which have a very narrow swath (Delanoë et al., 2011). Therefore, there is a shortage of research evaluating model's skill in predicting clouds against high temporal resolution observations. In this thesis, this need is partly covered by using ceilometer observations, which are densely distributed globally.

Forecasting solar radiation and clouds

In the solar energy field, the interest is in the actual and forecast amount of solar radiation on the ground. The solar radiation received at the Earth's surface depends on the solar zenith angle and the absorption and scattering of the radiation in

the atmosphere, clouds being the major contributor. Both the amount of clouds (cloudiness) and cloud type affect the amount of solar radiation reaching the surface: optically thick liquid clouds scatter solar radiation more effectively than deeper but optically thinner ice clouds, resulting in less solar radiation on the ground when liquid or mixed-phase clouds are present. Operational NWP models can be used to predict the incoming solar radiation and to estimate the potential solar energy produced by the solar farm, for example, one day-ahead. The model's capability to predict the incoming solar radiation is dependent on the model's capability to predict clouds. Numerical models have been shown to have deficiencies in predicting clouds containing supercooled liquid (Forbes and Ahlgrimm, 2014) resulting in a bias in the predicted shortwave solar radiation (Ahlgrimm and Forbes, 2012).

There are earlier studies estimating the accuracy of the solar radiation forecasts (e.g. Schroedter-Homscheidt et al., 2017) and accuracy of the solar radiation data obtained from the reanalysis (e.g. Frank et al., 2018; Urraca et al., 2018) at different locations based on solar radiation measurements, satellite-derived radiation products and numerical model data. These studies focus on solar radiation forecast error, and do not investigate the possible source of the error. Investigating the impact of the representation of clouds in NWP models on solar radiation forecasts mainly rely on extensive cloud profiling instrumentation (Ahlgrimm and Forbes, 2012), that are installed at sparsely distributed research facilities, such as Cloudnet stations (Illingworth et al., 2007) and Atmospheric Radiation Measurement facilities (Mather and Voyles, 2013). In this thesis, the emphasis has been to step beyond solely documenting accuracy of the solar radiation forecast and investigating the impact of low- and mid-level clouds by using simpler instrumentation, therefore being applicable to hundreds of sites globally.

3. Data and methods

In this thesis, a wide range of different meteorological data were used to identify and model LLJs, and to observe and forecast clouds and solar radiation. Vertical profiles of horizontal wind speed obtained from reanalysis data, Doppler wind lidar observations and an LES model were used to investigate LLJs. In addition, wind speed measurements from cup and sonic anemometers, and radiosoundings were used as an additional source of wind speed information. Clouds and solar radiation were observed using ceilometer and pyranometer instruments, respectively, and forecast by the operational NWP model. Automated algorithms were developed to objectively identify LLJs and the presence of clouds. The specific observational data sets, numerical model data and algorithms used in this thesis are described in the following sections in more detail.

3.1. Observational data

Doppler lidar observations

Doppler lidar observations are used in papers II and III to obtain vertical profiles of horizontal wind speed and direction and to investigate LLJs. A Halo Photonics Streamline Doppler lidar is used in both studies (Pearson et al., 2009). This instrument emits a light pulse at a wavelength of $1.5\ \mu\mathrm{m}$ and measures the Doppler shift of the backscattered signal, which is further post-processed to get the line-of-sight velocity of the air (aerosols). Furthermore, the wind speed and direction profiles are calculated from the combination of the line-of-sight velocities in several beam directions, assuming the horizontal homogeneity of the wind field. The line-of-sight resolution is 30 m, and therefore changing the scanning pattern of the instrument (and the elevation angle of the beam) changes both the vertical resolution of the final wind profile and also the measurement volume over which horizontal homogeneity must be assumed. In addition, the temporal resolution of the wind measurements depends on the choice of the scanning pattern.

In paper II, the temporal resolution of the wind profiles is 10 minutes, and the wind profile is concatenated by using two different scanning types, a 24-beam VAD scan at 4°elevation and a 3-beam DBS scan at 70°elevation, and additional sonic anemometer observations. The resulting vertical resolution is 2 m below 130 m, where the VAD scan is used and 28 m above 130 m, where the DBS scan is used. Sonic anemometer measurements were inserted at the corresponding height level (20 m above ground). The vertically pointing operation between the two different scans was used to derive the vertical velocity.

In paper III, the scan type used was a VAD at 75°elevation angle, resulting in

vertical a resolution of 29 m. The temporal resolution of the data was 15 minutes. Over two years of continuous Doppler lidar observations were used in paper II, and in paper III the data period was over four years.

Ceilometer observations

Four years of continuous Vaisala CL51 ceilometer atteanuated backscatter profiles were used in paper IV to detect clouds. The ceilometer emits a laser pulse close to 910 nm into the atmosphere and receives the backscattered signal from the aerosols, cloud droplets and precipitation. The backscatter coefficient is reported with 10 m range resolution up to 15 km, with a vertical profile every 15 seconds. The knowledge of the shape of the attenuated backscatter profiles and the magnitude of the attenuated backscatter coefficient in cases of clear sky, liquid cloud layer, ice cloud, precipitation, and fog can be used to identify these meteorological conditions automatically from the ceilometer data. The laser signal attenuates in thick cloud layers or in heavy precipitation, and no information is available from above. However, the ceilometer time series data can be used to estimate the amount of clouds in the sky (cloudiness).

Other observations

In addition to ground-based remote sensing instrumentation used in papers II, III, and IV, more traditional meteorological observations were used. Additional wind observations in papers II and III were obtained by using sonic anemometer, cup anemometer and wind vanes. These observations were used to supplement the Doppler lidar wind speed measurements and to quality check the Doppler lidar data. Data from radiosoundings are used in paper III to compare the results of a case study. Eddy-Covariance technique, used in paper III to investigate the effect of LLJs on the fluxes of latent and sensible heat and the net ecosystem CO_2 exchange, requires a sonic anemometer in addition to an open path gas-analyser (Mauder et al., 2013). Pyranometers were used in paper IV to observe the GHI, and 1-minute averaged, quality-controlled GHI values (Long and Shi, 2008; Rontu and Lindfors, 2018) over four years were used.

3.2. Model data

Arctic System Reanalysis

The first version of the Arctic System Reanalysis (ASR) data set (ASR-Interim, Bromwich et al., 2010) was used in paper I to investigate the climatology of LLJs. ASR covers Northern hemisphere mid-latitude and polar regions north of

45°N. ASR is optimised for polar regions as it was produced by using the polar optimised Weather Research and Forecast (Polar-WRF) model with three-dimensional variational (3D-Var) data assimilation scheme. The horizontal resolution is 30 km, and the model has 71 model levels. The output data were available at 34 pressure levels resulting in a vertical resolution of 25 hPa between 1000 hPa and 500 hPa. Temporal resolution of the reanalysis output was three hours. The downloaded variables contained horizontal wind components (u, v) and geopotential height at each model pressure level, in addition to single-level parameters such as terrain height and wind components at 10 m height. The data set used covered winter season (October to March) over an 11-year period (2000 to 2010).

Integrated Forecast System

Integrated Forecast System (IFS) is a global forecast model run operationally by the European Centre for Medium-Range Weather Forecasts (ECMWF). IFS model output was used in paper IV to investigate the cloud and solar radiation forecasts. The high-resolution deterministic forecasts are run every 12 hours and forecasts up to 10-day-ahead are produced. The horizontal resolution of the latest model cycle is approximately 9 km and there are 137 vertical levels. The vertical grid spacing is denser closer to the ground. In this thesis only data below 15 km is considered (as we are interested in clouds) and therefore the vertical resolution varies between 20 and 300 m. The temporal resolution of the model output is one hour. For the model evaluation, only the closest grid point to the measurement site is considered and day-ahead forecasts (initialisation at 12 UTC, forecast hours T+12 to T+35) were used to represent each day from 00 UTC to 23 UTC. The day-ahead cloud and solar radiation forecasts were evaluated over a four year time period (2014–2017) by using the single-level cloud cover and solar radiation fields (low cloud cover, medium cloud cover, downward surface solar radiation). In addition, other single-level and model-level fields were downloaded and used in paper IV for more detailed analysis, for example, the temperature and specific cloud liquid water content fields for investigating the solar radiation forecast error in case of supercooled liquid clouds vs. warm liquid clouds. A full documentation of the IFS can be found from ECMWF documentation (ECMWF, 2019, https://www.ecmwf.int/en/forecasts/documentation-and-support/changes-ecmwf-model/ifs-documentation (last access: 1 April 2019)).

ICON Large Eddy Model

The global ICOsahedral Non-hydrostatic atmospheric model (ICON, Zängl et al., 2015) is developed further to perform as a large eddy simulation model (ICOM-LEM,

Dipankar et al., 2015) and evaluated by Heinze et al. (2017). In paper III, LES simulation of one day, produced by using ICON-LEM, is used in a case study to investigate the spatial representation of the wind field around Jülich Observatory for Cloud Evolution measurement site, in Jülich, Germany. The model setup, similar to that used by Heinze et al. (2017), includes four nests starting with the outermost nest with a radius of 110 km and a horizontal resolution of 624 m to the innermost nest with a radius of 10 km and a horizontal resolution of 78 m, centered at the measurement site. There are 33 vertical levels in the lowest 2 km, resulting in minimal layer thickness of 20 m. The model output is stored every 10 minutes over the whole domain, and profile data every 9 seconds at the measurement site are available.

3.3. Algorithm development

Different algorithms have been developed in this thesis to automatically investigate the phenomena of interest. A LLJ identification algorithm suitable for a gridded data set was created in paper I to investigate the LLJs grid point by grid point. In paper II, a LLJ identification algorithm suitable for high temporal and vertical resolution wind profile data from Doppler wind lidar was created and applied to over two and over four years of wind profile data in papers II and III, respectively. Cloud detection was produced by the combination of three algorithms: detection of liquid layer, precipitation and fog, which were developed in paper IV.

Low-level jet identification

A low-level jet is a local maximum in the vertical profile of the wind speed. In paper I, the following approach is used to identify LLJs from the reanalysis data: First, the heights and wind speeds of all local maxima and minima below 1500 m are identified (Figure 1). It is further required that the local maximum must fulfill the criteria of being at least 2 m s^{-1} and 25 % stronger than the local minima above and below the maximum, following the criteria by Baas et al. (2009), to be identified as a LLJ feature. Multiple LLJs are allowed and identified with the algorithm, if present. In paper I, this approach is applied to all time steps (every 3 hours) and for each grid point to identify LLJs automatically from the ASR data.

In paper II, in addition to the identification described above, additional steps are required for LLJ identification in high temporal and vertical resolution Doppler lidar data. It is required that the identified LLJ is a coherent feature and therefore each wind profile is compared to the previous profile requiring that there are no sudden jumps in the wind speed values, for example due to data quality issues. Additionally, it is required that the feature is present for at least one hour, discarding individual profiles to be identified as LLJ case. This approach is then applied to all wind profile

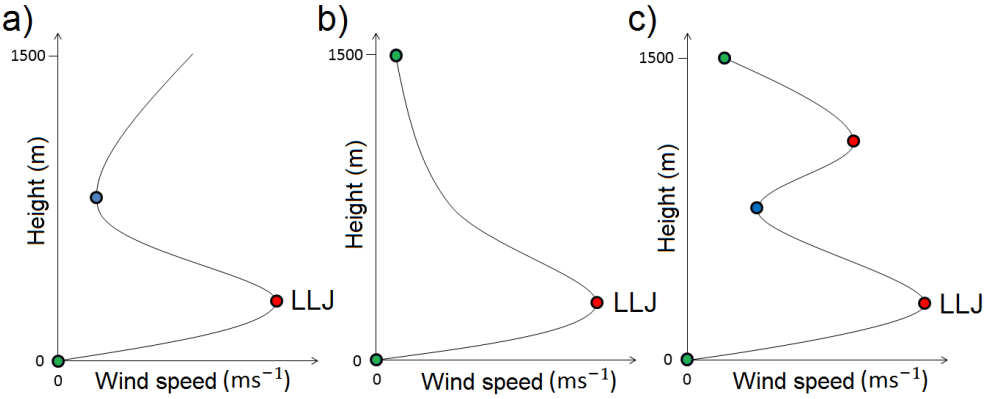

Figure 1: Schematic figure of identification of a LLJ from a wind profile. Red dots show local maxima, blue dots show local minima and green dots show points where minima are declared due to their location either at the surface or immediately below 1500 m. (a) The case of one local maximum and one local minimum below 1500 m, (b) the case of one local maximum but no local minimum below 1500 m and (c) the case of two local maxima and one local minimum below 1500 m. Figure from paper I, © 2015 The Atmospheric Science Letters

measurements from the Doppler lidar data automatically. The algorithm can be also applied to real-time Doppler lidar measurements to operationally identify LLJs.

Fog, liquid cloud layer and precipitation identification

Attenuated backscatter profile from the ceilometer reveals information on the meteorological conditions, such as whether it is precipitating or not. It also gives information on clouds, whether there is fog, liquid cloud layers or high ice clouds. These conditions can be automatically identified based on the shape of the attenuated backscatter profile and the magnitude of the signal.

A fog layer just above the ground shows a strong attenuated backscatter signal in the first range gates with rapid decrease above, as the lidar signal is attenuated in the fog layer (Figure 2a). Liquid cloud layers above the surface show a similar feature, however the full peak shape is visible (Figure 2b). The shape of the attenuated backscatter signal is different in the case of precipitation, as the the lidar signal is not attenuating as fast as in liquid clouds and the lidar can ”see” further into the layer resulting in wider and weaker peak (Figure 2c). These principles of the physical behavior of the transmitted laser pulse and the received backscattered signal can be used to automatically detect these meteorological conditions.

These algorithms can be used for both research and operational purposes. In

addition to derive the cloudiness, the accurate real-time detection of liquid cloud layers can be crucial for wind turbine operation as in-cloud icing due to clouds containing supercooled liquid is a notable issue in cold climates.

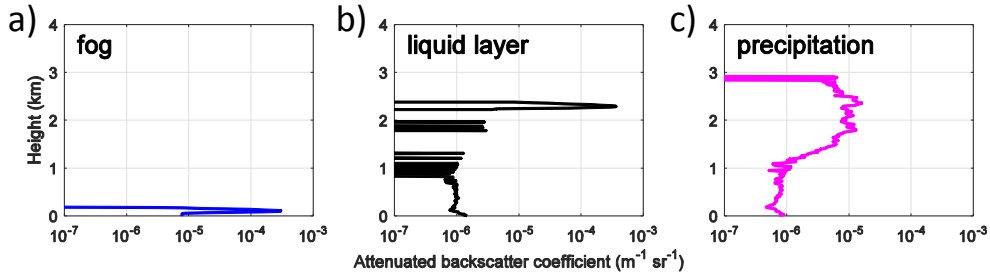

Figure 2: Schematic figure of identification of a) fog, b) liquid layer and c) precipitation from ceilometer attenuated backscatter profile data. Figure from paper IV, © 2019 Atmospheric Chemistry and Physics

4. Overview of main results

4.1. Climatology of wintertime low-level jets based on Arctic System Reanalysis

An 11-year climatology of low-level jets occurring in winter-time (October to March) in the Northern hemisphere mid-latitudes and polar regions was developed based on the Arctic System Reanalysis data set in paper I. A LLJ identification algorithm was created and applied to wind profiles obtained from the reanalysis at every time step and grid point. The LLJ frequency of occurrence and characteristics, the mean LLJ wind speed and height, were determined. These LLJ properties depend upon a range of geographical influences, including topography and contrasts in surface roughness and temperature across land/ocean and sea ice/open ocean boundaries.

The highest LLJ frequency of occurrence (up to 80–90%) was found to be associated with strong gradients in topography: on the coasts of Greenland and in the south-eastern parts of Russia where, based on the analysis of LLJ characteristics, LLJs are most probably due to katabatic forcing. High LLJ occurrences were also found elsewhere in the mountainous areas in Siberia and Alaska. In general, a higher LLJ frequency of occurrence was found over land compared to open sea. However, over sea ice the LLJ frequency of occurrence is higher compared to open sea. High LLJ frequency of occurrence values were found to be located on the sea-ice edge area where the strongest baroclinic zone between the open sea and sea ice is present.

The sea-ice effect was investigated further and Figure 3 shows that the higher LLJ occurrence values follow the sea ice edge (red line). During March (Figure 3a), when the sea ice cover over the Arctic is at its maximum, the LLJ occurrence is high especially over sea ice near the ice edge. In October (Figure 3b), when the sea ice cover is at its minimum, the LLJ occurrence is lower over those areas where the sea ice edge enhanced the LLJ occurrence in March but from where the sea ice has retreated towards north in October. The LLJ occurrence over steep topographical gradients, such as over Greenland, remains high in both cases and a LLJ feature is present over 80% of the time, therefore strengthening the hypothesis of topography-related forcing mechanisms playing an important role.

The strongest and highest LLJs, in terms of wind speed maximum and its altitude, occurred over the open sea, however this is where the LLJ occurrence is relatively low. The spatial variation of the mean height of LLJ reveals that in some areas LLJs always occur very close to the ground, such as in the coastal regions of Greenland and in the mountainous areas in Siberia and Alaska – from where no previous LLJ studies are available. In these areas the mean height of LLJs was below 200 m. These low, but frequently occurring LLJs show LLJ mean wind speeds of up to 14 $\mathrm{m\,s^{-1}}$.

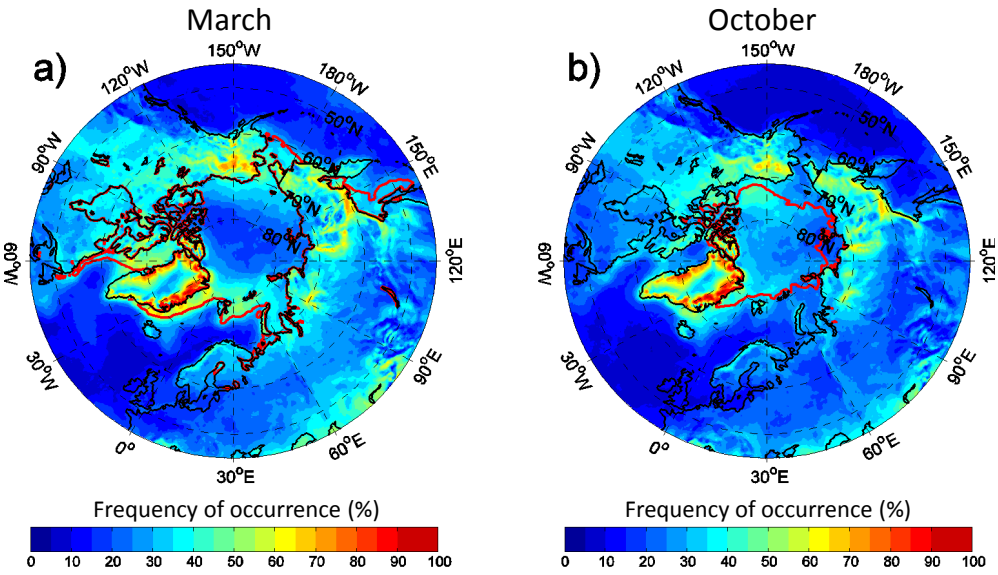

Figure 3: The low-level jet frequency of occurrence in (a) March when the sea ice has its maximum extent and (b) October when the sea ice has its minimum extent. The sea-ice edge, defined as the 11-year mean sea-ice concentration greater than 0.5 is shown by the red contour. Figure from paper I, © 2015 The Atmospheric Science Letters.

The use of a reanalysis dataset enabled the investigation of LLJs over a long time window and over a large area, revealing previously unknown areas of high LLJ occurrence. On the other hand, there are deficiencies in temporal and spatial resolution of the reanalysis data increasing the uncertainty of the results. In this study, only wind profiles below 1500 m were investigated. The vertical resolution of the reanalysis output results in 8 to 9 vertical levels below 1500 m, thus resulting in coarse representation of the boundary layer. The coarse vertical resolution in addition to 3-hourly temporal resolution of the output affects the results and the finest structures and rapid changes of the stable boundary layer and the LLJs may not be well captured. Therefore, the importance of high temporal and vertical resolution data are well acknowledged as an additional source of data to verify the reanalysis results.

4.2. Climatology of low-level jets based on Doppler wind lidar observations

Low-level jet climatologies, obtained based on Doppler lidar wind profile observations, were derived at Utö, Finland in paper II and at Jülich, Germany in paper III. A LLJ identification algorithm suitable for high temporal and vertical resolution Doppler

lidar data was created in paper II and applied to several years of wind profile observations from Utö and Jülich. With long time series of high temporal and vertical resolution wind profile observations, the LLJ frequency of occurrence and LLJ characteristics were derived with greater detail for specific sites than what was possible to achieve based on the reanalysis data in paper I.

Figure 4 shows two examples of the Doppler lidar wind data measured at Utö, Finland, with the LLJ identification algorithm applied to the measured wind profiles (black stars denoting a detected LLJ case). The data availability issues of the Doppler lidar data due to clean air (lack of aerosols to track, especially an issue at Utö), the presence of low clouds (fully attenuated lidar signal) and turbulent motions (invalid horizontal homogeneity assumption) may affect the results, as at times the wind data must be discarded as unreliable (Figure 4b). However, the Doppler lidar is a powerful instrument to obtain wind profiles in the lowest few hundred meters of the atmosphere, at height levels specifically important to wind energy. The low-level jet identification algorithm created in this study is also suitable for operational use, and the algorithm has already been applied to other Doppler lidars, both for research and operational use.

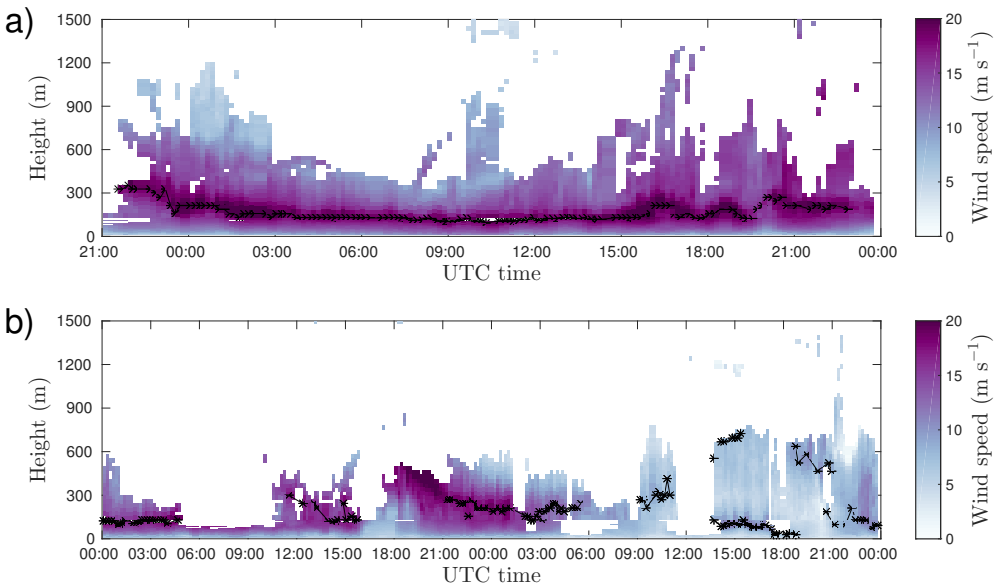

Figure 4: Time–height plots of horizontal wind speed derived from Doppler lidar data at Utö (a) between 2100 UTC 20 May 2013 and 0000 UTC 22 May 2013 and (b) between 17 and 18 May 2013. Horizontal wind speed is given by the color shades; white regions denote missing wind speed data due to lack of signal. Black stars denote LLJ profiles, with black lines linking appropriate LLJ profiles into an LLJ case. Figure from paper III, © 2017 American Meteorological Society

Utö is a small island in Finnish archipelago, and the area could be a potential source of wind energy production in the future. LLJs are a common feature at the site, the mean LLJ frequency of occurrence over all seasons being 12%. A clear seasonal cycle is observed at Utö with LLJ frequency of occurrence less than 5% in winter, and up to 30% during summer. However, there is only a slight increase in LLJ occurrence at nighttime in summer, and apart from that no clear diurnal cycle was observed. In turn, some jets were found to persist continuously over several days. The mean LLJ wind speed is 11.6 $\mathrm{m\ s^{-1}}$ and the strongest LLJs are observed during spring and winter. The majority of the LLJs were observed below 150 m in all seasons, thus can have a major impact of wind turbine operations. Additionally important for wind energy, the wind shear induced by the LLJs due to the strong change in wind speed with height was found to be greater below the jet compared to above the jet.

By using the same LLJ identification algorithm as in paper II, a climatology of LLJs was derived at Jülich, Germany, and similar statistics of LLJ characteristics were derived. LLJ occurrence shows a much clearer diurnal cycle at this location, compared to results from Utö, strongly favoring nighttime occurrence. The locations of these two sites highly affect the results; Utö is located in the archipelago representing marine conditions, whereas Jülich represents a continental site and is located further south. Therefore, the forcing mechanisms and characteristics of the LLJs in these two locations would be expected to differ. In paper III the shear and turbulence characteristics of LLJs and their influence on the surface fluxes were investigated based on the additional surface measurements. Similarly, as found in paper II, the wind shear is highest below the jet, and it was shown in paper III that the turbulence connected to the jet is high close to the ground. This is highly important for wind energy, as the highest shear and turbulence values related to the LLJs are occurring at low altitudes, within the height range of modern wind turbines.

A case study utilizing an LES model in paper III showed that the LES model captures the LLJ feature, however, the modeled LLJ has slightly stronger and sharper LLJ maximum in the wind speed profiles compared to the Doppler lidar observations, potentially due to too weak turbulent mixing in the model. The LES model was used to further understand the effect of topography to the wind field. The analysis revealed that the small hill close to the measurement site can affect the spatial wind field.

4.3. Evaluating cloud and solar radiation forecasts

Operational one day-ahead cloud and solar radiation forecasts by the ECMWF IFS model were evaluated at Helsinki, Finland, by comparing ceilometer and solar radiation observations to cloud cover and solar radiation forecasts in paper IV. Algorithms to detect liquid cloud layers, fog, and precipitation from ceilometer attenuated backscatter profiles were developed to obtain reliable cloud cover

information (Figure 5). In addition, methods to enable a fair comparison between model forecasts and point observations were developed and tested at one site in this study.

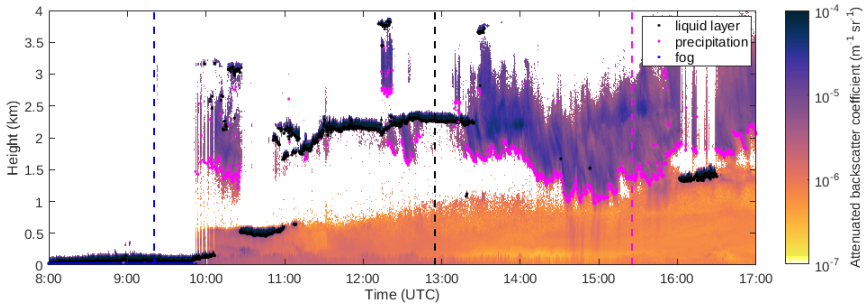

Figure 5: Time–height cross section of attenuated backscatter profiles from a Vaisala CL51 ceilometer on 30 March 2016 at Helsinki, Finland. Overplotted are the results from our identification algorithms: fog (blue dots), liquid cloud base (black dots), and precipitation base (magenta dots). The dashed lines represent the time steps of the sample attenuated backscatter profiles shown in Figure 2. Figure from paper IV, © 2019 Atmospheric Chemistry and Physics.

The skill in forecasting clouds was found to be lower in spring and summer when there are more broken cloud cases compared to winter when overcast situations are more common and easier to predict. However, in summer the amount of incoming solar radiation is highest due to the seasonal cycle of solar radiation, originating from the seasonal cycles of the solar zenith angle and cloudiness.

At Helsinki, Finland, the solar radiation forecasts show overall positive bias. In principle, the bias is negative in cases where the model overestimates the cloud cover (cases above the diagonal in Figure 6) and positive when the model underestimates the cloud cover (cases below the diagonal in Figure 6). A negative bias was found in clear cases where the cloud cover was correctly forecast (lower left corners in Figure 6) and a positive bias was found in overcast cases where the cloud cover was correctly forecast (upper right corners in Figure 6).

Averaging the data from hourly to 3-, 6-, 12-hourly, and daily values, the skill in cloud cover forecasts increased and solar radiation forecast errors decreased with increasing averaging window. This is an important finding as it shows that the model performs better when estimating the cloudiness and the amount of solar radiation over a longer time window, as it is difficult for the model to get the exact timing of the clouds correct with hourly temporal resolution at one specific location. This result suggests that the model performs better in getting the cloudiness and the amount of solar radiation correct on average, rather than predicting each individual cloud accurately.

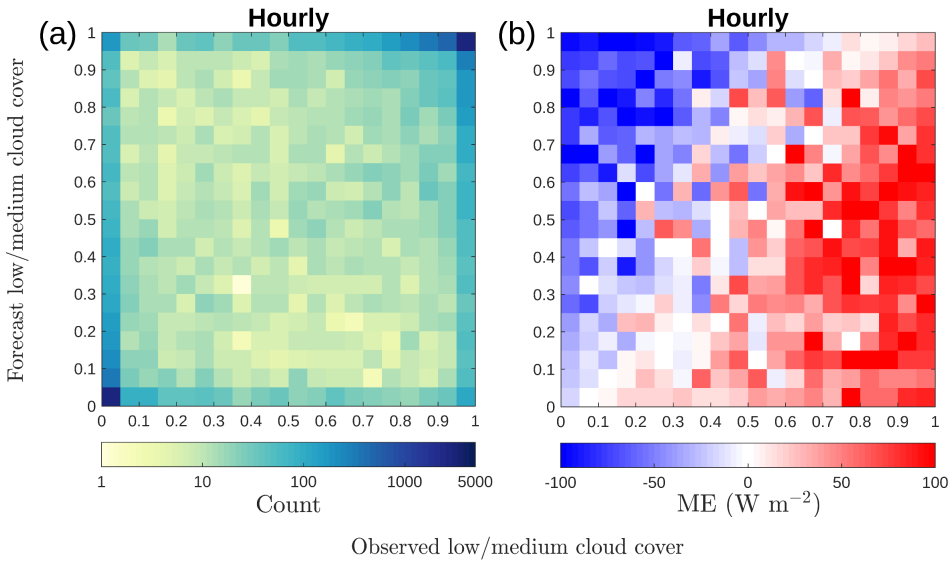

Figure 6: 2D-histogram of (a) observed and forecast cloud cover, with colors representing counts on a logarithmic scale, and (b) Mean error (ME) in solar radiation forecast for each cloud cover pair in (a). Figure from paper IV, © 2019 Atmospheric Chemistry and Physics.

The positive bias during correctly forecast overcast cases was investigated further and found to be related to cases where the forecast cloud Liquid Water Path (LWP) is low. These results suggest that the model is either not producing enough cloud liquid water or that there are deficiencies in forecasting the optical properties of clouds having low LWP. This aspect should be investigated further with LWP observations that were not available for this study at this site.

The algorithms and methods developed in this study can be further applied to hundreds of sites globally to investigate the skill in cloud and solar radiation forecasts based on relatively simple data sets. The liquid layer identification algorithm can be also used in the wind energy sector to estimate the conditions of in-cloud icing, as supercooled liquid clouds play an important role in case of meteorological icing of wind turbine structures.

5. Review of papers and author's contribution

Paper I: The focus of this study was to determine the climatology of LLJs in the mid-latitudes and polar regions of the Northern Hemisphere based on reanalysis. The focus was on the cold season (October to March) and the aim was to investigate where LLJs frequently occur and what are their mean characteristics.

Paper II: The first aim of this study was to develop an objective LLJ identification algorithm suitable for Doppler wind lidar and the second aim was to apply the algorithm over two years of wind profile measurements from Utö, Finland, and to investigate the LLJ occurrence and characteristics, and their seasonal and diurnal variability.

Paper III: The objective of this study was to investigate LLJ occurrence and characteristics, and their seasonal and diurnal variability at Jülich, Germany based on Doppler lidar observations. A more detailed analysis on the LLJ turbulence characteristics and the influence on LLJs on the surface fluxes was conducted in addition to a case study focusing on the interaction of a LLJ with the local topography.

Paper IV: The objective of this study was to investigate how well clouds and solar radiation are forecast at Helsinki, Finland, based on ceilometer and pyranometer observations and operational NWP model output. The aim was to develop fast and robust methods for investigating the relation between cloud and solar radiation forecasts, which can then be applied to hundreds of sites globally by using relatively simple instrumentation.

The author was responsible for most of the work in **papers I**, **II** and **IV**. For **paper I**, the author developed the low-level jet identification algorithm, applied it to the gridded reanalysis data, post-processed and analysed the results, and wrote the paper with the help of co-authors. For **paper II** the author developed an automated low-level jet identification algorithm, applied the algorithm to Doppler wind lidar observations, analysed the results, and wrote the manuscript with the help of co-authors. The low-level jet identification algorithm suitable for Doppler lidar data was further implemented to another site with a Doppler lidar, and the results are shown in **paper III**. The author helped with implementing the algorithm, analysing the results and writing the manuscript. The algorithm development, analysis of the results and writing of **paper IV** was mostly done by the author.

6. Conclusions and future perspectives

How can low-level jets and clouds, and their potential impact on renewable energy, be investigated based on a range of meteorological observations, reanalysis and numerical weather prediction model output?

An 11-year wintertime climatology of LLJs was investigated in **paper I** based on the reanalysis data set covering the Northern Hemisphere mid-latitude and polar regions. The occurrence of LLJs and their mean characteristics were investigated and new information on frequently occurring LLJs was gained in regions where no earlier LLJ studies have been conducted. Reanalysis data can be used to increase our understanding of certain phenomena over a wider temporal and spatial scale to understand the ”bigger picture”. This information is helpful for example when prospecting potential areas for renewable energy production before any detailed analysis.

More detailed climatologies and characteristics of LLJs at individual sites are derived in **papers II** and **III** based on long-term Doppler wind lidar observations. Site specific information on the shear and turbulence characteristics related to LLJs can be investigated with high temporal and vertical resolution Doppler lidar data. This information can be further utilized in understanding how LLJs would affect structures, such as causing stress on the wind turbines.

A climatology of cloudiness and solar radiation at Helsinki, Finland was derived in **paper IV** based on ceilometer and pyranometer observations. The skill in operational short term (day-ahead) cloud forecast and its impacts on solar radiation forecast were evaluated by using fast and simple methods developed in this paper. These methods are applicable for any site with relatively simple instumentation: ceilometer and pyranometer observations. Therefore, this study can be repeated at hundreds of sites globally, a major advantage compared to the previous studies, conducted mainly at a few measurement sites having extensive research instrumentation.

The algorithms created in this thesis enable the real-time identification of LLJs and clouds, separating liquid cloud layers, precipitation (and ice clouds) and fog. These algorithms are available for operational and research purposes, and they are applicable to Doppler lidar wind profiles and ceilometer attenuated backscatter observations. The LLJ identification algorithm has been applied to different studies and is in operational use at the Mace Head station operated by the National University of Ireland Galway. The liquid cloud layer identification will be applied to the European-wide cloud profiling network, Cloudnet, and the European-wide ceilometer network, E-Profile, enabling the detection of liquid clouds more accurately than previously achieved. The improved cloud detection algorithms are already used operationally at the Finnish Meteorological Institute. The algorithms for ceilometer data can be also used to

identify potential icing conditions that are important for aviation and wind energy.

How well do different numerical models represent low-level jets, clouds and solar radiation?

Results of LLJs derived based on reanalysis data in **paper I** were compared to results from one specific site in **paper II** by investigating the closest grid point to the measurement site. The LLJs identified based on reanalysis were higher and weaker than those observed with the Doppler lidar, but the predominant LLJ direction was similar in both data sets. Thus, there are deficiencies in the ability of reanalysis to represent this phenomenon accurately, probably due to the coarse spatial and temporal resolution. For example, at Utö, the LLJ can occur in the lowest 50 meters, and therefore it is challenging for the model to represent such rapid changes in the vertical if the model vertical resolution is quite coarse.

In **paper III**, an LES model was used to investigate the effect of topography on a LLJ case. In this study, it was seen that this individual case was quite well represented in the model. However, the LES model may not help with operational use, because of the high computational requirements for achieving the necessary resolution. Running the LES model is computationally expensive and therefore not suited for operational use. However, the detailed analysis of LLJ forcing mechanisms with LES models increases our understanding of the phenomenon, and these methods should be extended in the future to other sites.

In **paper IV**, the conclusions of the evaluation of an operational NWP model's skill in forecasting clouds and solar radiation revealed that the model predicts clouds and solar radiation quite well on average. However, there are difficulties in forecasting the timing of clouds, resulting in large errors, especially for hourly values. The model shows a positive bias in overcast situations, which is attributed to a problem in representing cloud properties, resulting in an inaccurate solar radiation forecast even though the amount of cloud is correctly forecast. Additionally, it was found that the model shows a negative bias in cloud-free situations, potentially due to deficiencies in representing the aerosols. The results in this study should be repeated at several sites to gain more understanding of these errors.

How observational systems can help numerical weather prediction model development?

This thesis includes algorithm development that can help both NWP model and furthermore reanalysis development. The LLJ identification algorithm developed in **paper II** can be applied to any site having Doppler lidar. To understand the model capability in representing LLJs, long data sets of observational data can be investigated

by applying the objective LLJ identification algorithm and consistently comparing the results with the model output. The characteristics of LLJs can be compared between the model and observations to understand which aspects the model can represent, and which ones it fails to capture in different conditions. Similarly, reanalysis data can be evaluated in more detail to gain information on when the reanalysis accurately captures observed features.

The methods in **paper III** using LES model to reproduce the LLJ feature can help model development as more information can be gained on the effects of changing model parameters or parametrizations, and model resolution. This enables more information on the model's capability to produce the phenomenon and can help us to understand what features are the most critical when interested in LLJs.

The methods in **paper IV** can guide model physical process development as potential root causes for errors in solar radiation forecasts were identified. More analysis should be made in order to get reliable results, for example, including observations of LWP. Additionally, more sites should be included in the analysis to understand if similar features can be seen elsewhere giving more confidence on the causes of errors.

In the future, more analysis on the model's performance regarding LLJs, clouds and solar radiation can be achieved with the algorithms and methods developed in this thesis. Attention has to be paid to get comparable data sets between the observations and model output due to the fundamental differences in point observations and gridded model data, as described in more detail in **paper IV**.

References

Ahlgrimm, M., and R. Forbes, 2012: The impact of low clouds on surface shortwave radiation in the ECMWF model. *Monthly Weather Review*, **140**(11), 3783–3794.

Andreas, E. L., K. J. Claffy, and A. P. Makshtas, 2000: Low-level atmospheric jets and inversions over the western Weddell Sea. *Boundary-Layer Meteorology*, **97**(3), 459–486.

Baas, P., F. C. Bosveld, H. Klein Baltink, and A. A. M. Holtslag, 2009: A climatology of nocturnal low-level jets at Cabauw. *Journal of Applied Meteorology and Climatology*, **48**(8), 1627–1642.

Banta, R., R. K. Newsom, J. K. Lundquist, Y. L. Pichugina, R. L. Coulter, and L. Mahrt, 2002: Nocturnal low-level jet characteristics over Kansas during CASES-99. *Boundary Layer Meteorology*, **105**(2), 221–252.

Banta, R. M., Y. L. Pichugina, N. D. Kelley, R. M. Hardesty, and W. A. Brewer, 2013: Wind energy meteorology: Insight into wind properties in the turbine-rotor layer of the atmosphere from high-resolution Doppler lidar. *Bulletin of the American Meteorological Society*, **94**(6), 883–902.

Bauer, P., A. Thorpe, and G. Brunet, 2015: The quiet revolution of numerical weather prediction. *Nature*, **525**, 47–55.

Blackadar, A. K., 1957: Boundary layer wind maxima and their significance for the growth of nocturnal inversions. *Bulletin of American Meteorological Society*, **38**, 283–290.

Bromwich, D., Y.-H. Kuo, M. Serreze, J. Walsh, L.-S. Bai, M. Barlage, K. Hines, and A. Slater, 2010: Arctic System Reanalysis: Call for community involvement. *Eos, Transactions American Geophysical Union*, **91**(2), 13–14.

Bromwich, D. H., A. B. Wilson, L. Bai, Z. Liu, M. Barlage, C.-F. Shih, S. Maldonado, K. M. Hines, S.-H. Wang, J. Woollen, B. Kuo, H.-C. Lin, T.-K. Wee, M. C. Serreze, and J. E. Walsh, 2018: The Arctic System Reanalysis, version 2. *Bulletin of the American Meteorological Society*, **99**(4), 805–828.

Casati, B., L. J. Wilson, D. B. Stephenson, P. Nurmi, A. Ghelli, M. Pocernich, U. Damrath, E. E. Ebert, B. G. Brown, and S. Mason, 2008: Forecast verification: current status and future directions. *Meteorological Applications*, **15**(1), 3–18.

Delanoë, J., R. J. Hogan, R. M. Forbes, A. Bodas-Salcedo, and T. H. M. Stein, 2011: Evaluation of ice cloud representation in the ECMWF and UK Met Office models using CloudSat and CALIPSO data. *Quarterly Journal of the Royal Meteorological Society*, **137**(661), 2064–2078.

Dipankar, A., B. Stevens, R. Heinze, C. Moseley, G. Zängl, M. Giorgetta, and S. Brdar, 2015: Large eddy simulation using the general circulation model ICON. *Journal of Advances in Modeling Earth Systems*, **7**(3), 963–986.

Dörenkämper, M., M. Optis, A. Monahan, and G. Steinfeld, 2015: On the offshore advection of boundary-layer structures and the influence on offshore wind conditions. *Boundary-layer Meteorology*, **155**(3), 459–482.

Doyle, J. D., and T. T. Warner, 1993: A three-dimensional numerical investigation of a Carolina coastal low-level jet during GALE IOP 2. *Monthly Weather Review*, **121**, 1030–1047.

ECMWF, 2019: ECMWF IFS full documentation, `https://www.ecmwf.int/en/forecasts/documentation-and-support/changes-ecmwf-model/ifs-documentation` (last access: 1 April 2019).

ERA5, 2019: Copernicus Climate Change Service (C3S) (2017): ERA5: Fifth generation of ECMWF atmospheric reanalyses of the global climate. Copernicus Climate Change Service Climate Data Store (CDS), `https://cds.climate.copernicus.eu/cdsapp#!/home` (last access 1 April 2019).

Floors, R., C. L. Vincent, S. E. Gryning, A. Peña, and E. Batchvarova, 2013: The wind profile in the coastal boundary layer: Wind lidar measurements and numerical modelling. *Boundary Layer Meteorology*, **147**(3), 469–491.

Forbes, R. M., and M. Ahlgrimm, 2014: On the representation of high-latitude boundary layer mixed-phase cloud in the ECMWF global model. *Monthly Weather Review*, **142**(9), 3425–3445.

Frank, C. W., S. Wahl, J. D. Keller, B. Pospichal, A. Hense, and S. Crewell, 2018: Bias correction of a novel European reanalysis data set for solar energy applications. *Solar Energy*, **164**, 12–24.

Hasager, C., D. Stein, M. Courtney, A. Peña, T. Mikkelsen, M. Stickland, and A. Oldroyd, 2013: Hub height ocean winds over the North Sea observed by the NORSEWInD lidar array: Measuring techniques, quality control and data management. *Remote Sensing*, **5**(9), 4280–4303.

Heinze, R., et al., 2017: Large-eddy simulations over Germany using ICON: a comprehensive evaluation. *Quarterly Journal of the Royal Meteorological Society*, **143**(702), 69–100.

Higgins, R. W., Y. Yao, E. S. Yarosh, J. E. Janowiak, and K. C. Mo, 1997: Influence of the Great Plains low-level jet on summertime precipitation and moisture transport over the central United States. *Journal of Climate*, **10**(3), 481–507.

Hogan, R. J., E. J. O'Connor, and A. J. Illingworth, 2009: Verification of cloud-fraction forecasts. *Quarterly Journal of the Royal Meteorological Society*, **135**(643), 1494–1511.

Högström, U., and A.-S. Smedman-Högström, 1984: The wind regime in coastal areas with special reference to results obtained from the Swedish wind energy program. *Boundary Layer Meteorology*, **30**, 351–373.

Hu, X.-M., P. M. Klein, M. Xue, F. Zhang, D. C. Doughty, R. Forkel, E. Joseph, and J. D. Fuentes, 2013: Impact of the vertical mixing induced by low-level jets on boundary layer ozone concentration. *Atmospheric Environment*, **70**, 123 –130.

Illingworth, A. J., et al., 2007: CLOUDNET - continuous evaluation of cloud profiles in seven operational models using ground-based observations. *Bulletin of the American Meteorological Society*, **88**, 883–898.

Illingworth, A. J., D. Cimini, A. Haefele, M. Haeffelin, M. Hervo, S. Kotthaus, U. Löhnert, P. Martinet, I. Mattis, E. J. O'Connor, and R. Potthast, 2019: How can existing ground-based profiling instruments improve european weather forecasts? *Bulletin of the American Meteorological Society*, **100**(4), 605–619.

IPCC, 2018: Summary for Policymakers. In: Global warming of 1.5°C. An IPCC Special Report on the impacts of global warming of 1.5°C above pre-industrial levels and related global greenhouse gas emission pathways, in the context of strengthening the global response to the threat of climate change, sustainable development, and efforts to eradicate poverty [V. Masson-Delmotte, P. Zhai, H. O. Pörtner, D. Roberts, J. Skea, P.R. Shukla, A. Pirani, W. Moufouma-Okia, C. Péan, R. Pidcock, S. Connors, J. B. R. Matthews, Y. Chen, X. Zhou, M. I. Gomis, E. Lonnoy, T. Maycock, M. Tignor, T. Waterfield (eds.)]. World Meteorological Organization, Geneva, Switzerland, 32 pp.

IRENA, 2019: Renewable capacity statistics 2019. International Renewable Energy Agency (IRENA), Abu Dhabi.

Korolev, A., G. McFarquhar, P. R. Field, C. Franklin, P. Lawson, Z. Wang, E. Williams, S. J. Abel, D. Axisa, S. Borrmann, J. Crosier, J. Fugal, M. Krämer, U. Lohmann, O. Schlenczek, M. Schnaiter, and M. Wendisch, 2017: Mixed-phase clouds: Progress and challenges. *Meteorological Monographs*, **58**, 5.1–5.50.

Long, C. N., and Y. Shi, 2008: An automated quality assessment and control algorithm for surface radiation measurements. *The Open Atmospheric Science Journal*, **2**, 23–37.

Mao, H., and R. Talbot, 2004: Role of meteorological processes in two New England ozone episodes during summer 2001. *Journal of Geophysical Research: Atmospheres*, **109**(D20).

Mather, J. H., and J. W. Voyles, 2013: The ARM climate research facility: A review of structure and capabilities. *Bulletin of the American Meteorological Society*, **94**(3), 377–392.

Mauder, M., M. Cuntz, C. Drüe, A. Graf, C. Rebmann, H. P. Schmid, M. Schmidt, and R. Steinbrecher, 2013: A strategy for quality and uncertainty assessment of long-term eddy-covariance measurements. *Agricultural and Forest Meteorology*, **169**, 122–135.

Moore, G. W. K., and I. A. Renfrew, 2005: Tip jets and barrier winds: A QuikSCAT climatology of high wind speed events around Greenland. *Journal of Climate*, **18**(18), 3713–3725.

Parish, T. R., 1982: Barrier winds along the Sierra Nevada mountains. *Journal of Applied Meteorology*, **21**(7), 925–930.

Pearson, G., F. Davies, and C. Collier, 2009: An analysis of the performance of the UFAM pulsed Doppler lidar for observing the boundary layer. *Journal of Atmospheric and Oceanic Technology*, **26**(2), 240–250.

Peña, A., R. Floors, A. Sathe, S.-E. Gryning, R. Wagner, M. S. Courtney, X. G. Larsén, A. N. Hahmann, and C. B. Hasager, 2016: Ten years of boundary-layer and wind-power meteorology at Høvsøre, Denmark. *Boundary-Layer Meteorology*, **158**(1), 1–26.

Pichugina, Y. L., R. M. Banta, W. A. Brewer, S. P. Sandberg, and R. M. Hardesty, 2012: Doppler lidar–based wind-profile measurement system for offshore wind-energy and other marine boundary layer applications. *Journal of Applied Meteorology and Climatology*, **51**(2), 327–349.

Ranjha, R., G. Svensson, M. Tjernström, and A. Semedo, 2013: Global distribution and seasonal variability of coastal low-level jets derived from ERA-Interim reanalysis. *Tellus A: Dynamic Meteorology and Oceanography*, **65**(1), 20412.

Renfrew, I., and P. S. Anderson, 2006: Profiles of katabatic flow in summer and winter over Coats Land, Antarctica. *Quarterly Journal of the Royal Meteorological Society*, **132**, 779–802.

Rife, D. L., J. O. Pinto, A. J. Monaghan, C. A. Davis, and J. R. Hannan, 2010: Global distribution and characteristics of diurnally varying low-level jets. *Journal of Climate*, **23**(19), 5041–5064.

Rontu, L., and A. V. Lindfors, 2018: Comparison of radiation parametrizations within the HARMONIE–AROME NWP model. *Advances in Science and Research*, **15**, 81–90.

Savijärvi, H., S. Niemelä, and P. Tisler, 2005: Coastal winds and low-level jets: Simulations for sea gulfs. *Quarterly Journal of the Royal Meteorological Society*, **131**(606), 625–637.

Schroedter-Homscheidt, M., A. Benedetti, and N. Killius, 2017: Verification of ECMWF and ECMWF/MACC's global and direct irradiance forecasts with respect to solar electricity production forecasts. *Meteorologische Zeitschrift*, **26**(1), 1–19.

Smedman, A., M. Tjernström, and U. Högström, 1993: Analysis of the turbulence structure of a marine low-level jet. *Boundary Layer Meteorology*, **66**, 105–126.

Storm, B., J. Dudhia, S. Basu, A. Swift, and I. Giammanco, 2009: Evaluation of the Weather Research and Forecasting model on forecasting low-level jets: implications for wind energy. *Wind Energy*, **12**(1), 81–90.

Tucker, S. C., R. M. Banta, A. O. Langford, C. J. Senff, W. A. Brewer, E. J. Williams, B. M. Lerner, H. D. Osthoff, and R. M. Hardesty, 2010: Relationships of coastal nocturnal boundary layer winds and turbulence to Houston ozone concentrations during TexAQS 2006. *Journal of Geophysical Research: Atmospheres*, **115**(D10).

Urraca, R., T. Huld, A. Gracia-Amillo, F. J. M. de Pison, F. Kaspar, and A. Sanz-Garcia, 2018: Evaluation of global horizontal irradiance estimates from ERA5 and COSMO-REA6 reanalyses using ground and satellite-based data. *Solar Energy*, **164**, 339–354.

Vanderwende, B. J., J. K. Lundquist, M. E. Rhodes, E. S. Takle, and S. L. Irvin, 2015: Observing and simulating the summertime low-level jet in central Iowa. *Monthly Weather Review*, **143**(6), 2319–2336.

Werner, C., 2005: Doppler wind lidar. *Lidar*. Springer, 325–354.

Wiegner, M., F. Madonna, I. Binietoglou, R. Forkel, J. Gasteiger, A. Geiß, G. Pappalardo, K. Schäfer, and W. Thomas, 2014: What is the benefit of ceilometers for aerosol remote sensing? An answer from EARLINET. *Atmospheric Measurement Techniques*, **7**(7), 1979–1997.

Zängl, G., D. Reinert, P. Rípodas, and M. Baldauf, 2015: The ICON (ICOsahedral Non-hydrostatic) modelling framework of DWD and MPI-M: Description of the non-hydrostatic dynamical core. *Quarterly Journal of the Royal Meteorological Society*, **141**(687), 563–579.

I

Reprinted, with permission, from
The Atmospheric Science Letters, 16, 492–499,
doi:10.1002/asl.587

ATMOSPHERIC SCIENCE LETTERS
Atmos. Sci. Let. (2015)
Published online in Wiley Online Library
(wileyonlinelibrary.com) **DOI:** 10.1002/asl.587

RMetS
Royal Meteorological Society

A climatology of low-level jets in the mid-latitudes and polar regions of the Northern Hemisphere

M. Tuononen,[1]* V. A. Sinclair[1] and T. Vihma[2]
[1]*Department of Physics, University of Helsinki, Helsinki, Finland*
[2]*Arctic Research, Finnish Meteorological Institute, Helsinki, Finland*

**Correspondence to:*
M. Tuononen, Atmospheric Composition Research, Finnish Meteorological Institute, P.O. Box 503 (Erik Palménin aukio 1), FI-00101 Helsinki, Finland.
E-mail: minttu.tuononen@fmi.fi

Received: 27 January 2015
Revised: 8 May 2015
Accepted: 11 May 2015

Abstract

A wintertime climatology of the occurrence and characteristics of low-level jets (LLJs) in the Northern Hemisphere mid-latitudes and polar regions was developed. A LLJ detection algorithm was applied to 11 years of Arctic system reanalysis data. The highest occurrence of LLJs was associated with strong gradients in topography and with the sea-ice edge. Sea areas fully covered with sea ice also favoured the occurrence of LLJs, however, these areas, including the central Arctic, had fewer LLJs than along the sea-ice edge. LLJs also occurred frequently in the seldom studied Sea of Okhotsk area.

Keywords: **low-level jets; Arctic system reanalysis; sea ice; topography**

1. Introduction

A low-level jet (LLJ) is a localized maximum in the vertical profile of wind speed that typically occurs at a height between 100 and 1000 m. Often organized as narrow zones of high-speed flow that extend for hundreds of kilometres (Stensrud, 1996), LLJs are an important part of the lower-tropospheric circulation. Such LLJs can lead to horizontal transport of moisture which in turn modifies precipitation patterns and effects the hydrological cycle (Higgins *et al.*, 1997). Furthermore, LLJs lead to strong vertical wind shear which impacts turbulent mixing within the boundary layer, the exchange of heat, moisture, and trace gases between the surface and the atmosphere, aviation safety and wind energy production.

LLJs have previously been studied extensively and many such studies have attempted to identify the forcing mechanisms for LLJs. Consequently, it is known that LLJs develop due to inertial oscillations driven by temporal (Blackadar, 1957) and spatial variations (Högström and Smedman-Högström, 1984) in turbulent mixing. Baroclinicity, due to different sources, has also been demonstrated to be an important LLJ forcing mechanism. For example, shallow baroclinicity induced by coastlines and the sea-ice edge can lead to the development of LLJs (Doyle and Warner, 1993; Savijärvi *et al.*, 2005) as can synoptic-scale baroclinicity and baroclinicity due to sloping terrain. LLJs in regions of steep topography have also undergone considerable analysis. Blocking by topography can accelerate the low-level winds leading to barrier jets, which have been studied primarily along the coasts of California (e.g. Parish, 1982) and Greenland (e.g. Petersen *et al.*, 2009). Katabatic flows, which are very common over continental ice sheets, can also lead to the formation of LLJs (Renfrew and Anderson, 2006).

Although LLJs have been extensively studied, the majority of studies have considered mid-latitude LLJs, and especially the summertime Southern Great Plains LLJ (e.g. Mitchell *et al.*, 1995; Higgins *et al.*, 1997). Furthermore, many previous studies have been based on observations and thus are geographically limited and do not cover remote, data sparse regions. Recently, Rife *et al.* (2010) created a global climatology of nocturnal LLJs and identified many previously unknown regions where nocturnal LLJs are common. Ranjha *et al.* (2013) developed a global climatology of coastal LLJs based on ERA-Interim reanalysis data and found that coastal LLJs occur mainly along the western coasts of all continents. The analysis conducted by Ranjha *et al.* (2013) suggests that in Greenland katabatic LLJs are present approximately 25–30% of the time and are more common in winter than in summer. However, Ranjha *et al.* (2013) did not focus on these katabatic LLJs.

Hence, there may remain many unknown regions in the mid-latitudes and polar regions where LLJs are common, especially in the cold season when observational campaigns in the polar regions are very limited. Therefore, the first objective of this study is to determine where in the mid-latitudes and polar regions of the Northern Hemisphere LLJs frequently occur in the cold season (October–March). We focus on the cold season as we hypothesize that the majority of LLJs will be due to katabatic flows and to inertial oscillations within the stable boundary layer and thus will be more common in the cold season than in the warm season. The second objective of this study is to identify the typical

characteristics of the LLJs and postulate their forcing mechanisms.

2. Methodology

2.1. Arctic system reanalysis – interim data set

The first version of the Arctic system reanalysis [ASR-Interim, Bromwich *et al.* (2010)], which is a regional reanalysis covering all areas north of 45°N, is used in this study. The Arctic system reanalysis was developed with the aim of improving the representation of the Northern Hemisphere polar regions in a reanalysis compared to global reanalysis data sets. ASR-Interim was produced by using the Polar optimized version of the Weather Research and Forecast model (Polar-WRF) and a three-dimensional variational data assimilation scheme (3D-Var). Surface and upper air model-level data from the global reanalysis ERA-Interim are used as initial and lateral boundary conditions on the outer domain for the Polar-WRF model. Geopotential height, temperature and wind components are nudged towards ERA-Interim on all model levels in the outer domain and on model levels above 100 hPa in the inner domain of the model (Bromwich *et al.*, 2015). The temporal resolution of ASR-Interim is 3 h, the horizontal resolution is 30 km, and there are 71 model levels. The output data are available on 34 pressure levels, which have a vertical spacing of 25 hPa between 1000 and 500 hPa.

In this study we utilize the horizontal wind components (u, v) in three dimensions to calculate the wind speed at all grid points and on all pressure levels. To determine the height of the pressure levels we also obtain the geopotential height in three dimensions and the terrain height from ASR-Interim. The height above ground is calculated by subtracting the terrain height from the geopotential height which ensures that we do not consider any data on pressure levels that are below the surface. To enhance the vertical resolution of the wind profiles near the surface we use the 10-m horizontal wind components and we also set the wind speed to be zero at the surface. After adding the extra 10-m level, we find that on average there are eight or nine levels located below 1500 m. We analyse the 11-year period from 2000 to 2010 but we only consider winter months (October–March).

Bromwich *et al.* (2015) compared the near-surface and upper-level analyses from ASR-Interim and ERA-Interim with surface station data and soundings made in the Arctic region. They found that the correlation between the observed and analysed 10-m wind speed was higher in ASR-Interim than in ERA-Interim during every month (during winter months the correlation for ASR-Interim was 0.72 and for ERA-Interim 0.67) and that ASR-Interim showed slightly negative bias whereas ERA-Interim showed positive bias. Annual mean correlations between the observed and analysed horizontal winds were higher in ASR-Interim compared to ERA-Interim below 150 hPa. Winds at 1000 hPa had significantly smaller biases in ERA-Interim than in ASR-Interim but otherwise the wind fields below 150 hPa and at 10-m had smaller negative bias in ASR-Interim compared to ERA-Interim.

2.2. LLJ identification algorithm

There are many previous studies which have developed different criteria to identify LLJs. The first such study, by Bonner (1968), defined three classes of LLJs in which threshold values for the absolute wind speed (12, 16 and 20 $m\,s^{-1}$) and drop-off (decrease) of wind speed (6, 8 and 10 $m\,s^{-1}$) above the jet were defined. Bonner (1968) required the localized maximum in the wind speed associated with the LLJ (referred to hereinafter as the LLJ maximum) and the minimum in wind speed above the LLJ maximum both to be below 3 km. In contrast, Baas *et al.* (2009) required the LLJ maximum and minimum above both to be below 500 m and the wind speed of the LLJ maximum was only required to exceed 2 $m\,s^{-1}$. Baas *et al.* (2009) also applied a relative as well as an absolute criteria for the drop-off of wind speed above the maximum.

In this study, LLJs are identified using a relative and an absolute criteria, similar to Baas *et al.* (2009). The absolute criteria requires that the LLJ maximum must be at least 2 $m\,s^{-1}$ stronger than the minimums below and above the maximum. In weak wind conditions, the absolute criteria prevent small variations in wind speed with height being incorrectly identified as LLJs. In strong wind conditions, the relative criteria prevents random, turbulent variations in the wind speed with height, which exceed the absolute criteria, accidentally being identified as LLJs.

The absolute criteria requires that the LLJ maximum must be at least 2 $m\,s^{-1}$ stronger than the minimums below and above the maximum. The relative criteria requires that the LLJ maximum must be at least 25% stronger than the minimums below and above the maximum. The definition of the absolute criteria means that the maximum must be at least 2 $m\,s^{-1}$.

The heights and wind speeds of all local maximums and minimums below 1500 m are first identified. The wind speed at the surface is set to be 0 $m\,s^{-1}$ and it is assumed to be a minimum. The local maximums are then tested using the above defined absolute and relative criteria to determine if they are LLJs. In the case of one local maximum and one local minimum above (Figure 1(a)), if the relative and absolute criteria are met the maximum is declared to be a LLJ. In the case of one local maximum, but no local minimum above, the wind speed at the highest level below 1500 m is defined as a minimum (Figure 1(b)). The local maximum is only declared as a LLJ if the absolute and relative criteria are met. In the case where there are multiple local maximums below 1500 m (Figure 1(c)), the lowest maximum which meets the absolute and relative criteria is identified as the LLJ in the profile.

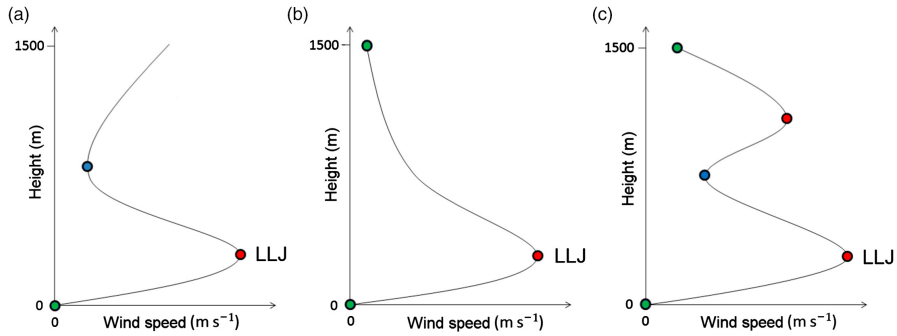

Figure 1. Schematic diagram showing the detection algorithm of low-level jets. Red dots show local maximums, blue dots show local minimums and green dots show points where minimums are declared due to their location either at the surface or immediately below 1500 m. (a) The case of one local maximum and one local minimum below 1500 m, (b) the case of one local maximum but no local minimum below 1500 m and (c) the case of two local maximums and one local minimum below 1500 m.

3. Results

3.1. Eleven-year climatology of LLJs

The 11-year climatology of the frequency of LLJ occurrence shows that LLJs are more frequent over land than over sea (Figure 2(a)). Over land points, LLJs occur during 31% of analysis times whereas over sea points the corresponding value is only 18%. LLJs occur most frequently (80–90%) in the coastal regions over Greenland and southeastern Russia, where strong horizontal gradients in topography exist (Figure 2(d)). Relatively high frequencies (60–80%) are also found over other mountainous areas in Siberia and Alaska. The lowest frequencies (5–15%) are found over the North Atlantic and the North Pacific. Regional variations in the frequency of LLJ occurrence are larger over land than over sea, which is largely due to the spatial inhomogeneities caused by topography over land. The frequency of LLJ occurrence is more spatially homogeneous over open sea than over sea ice.

Over open sea, the dominant forcing mechanism is most likely synoptic-scale baroclinicity, although LLJs can also be generated due to coastal orography, shallow baroclinicity related to sea surface temperature (SST) fronts, coastlines and sea-ice margins, and due to inertial oscillations induced by spatial variations in turbulent mixing downwind of SST fronts (Högström and Smedman-Högström, 1984). Over sea ice, all the above mentioned LLJ generation factors are active (the surface temperature fronts are mostly related to leads and polynyas). In addition, however, inertial oscillations induced by temporal variations in turbulent mixing occur more frequently than over the open sea, where the boundary-layer structure varies less. Hence, there is more variation in the type of forcing mechanisms acting over sea ice than over open sea, which leads to larger spatial variations in the frequency of LLJ occurrence. In the central Arctic, the frequency of LLJ occurrence is, based on ASR-Interim, relatively low (20–25%), much lower than analysed near the sea-ice edge, which is due to the absence of shallow persistent baroclinic zones and limited synoptically forced baroclinic zones.

The LLJs with the strongest wind speeds (up to 17 m s^{-1}) occur along the southeast coast of Greenland, in the coastal area of the Sea of Okhotsk, along the northeastern coast of Siberia and in the western North Atlantic (Figure 2b). Strong LLJs (14–15 m s^{-1}) also occur over the North Atlantic and North Pacific storm track regions as well as in the central part of southern Greenland. The weakest LLJs (4–5 m s^{-1}) are found over Siberia (between 120–150°E and 60–70°N). As expected, LLJs have stronger wind speeds over open sea than over land which is most likely due to a combination of reduced surface friction over open sea and the dominance of synoptic-scale baroclinicity as a forcing mechanism. LLJs over sea ice have weaker wind speeds than over open sea which, we hypothesize, is due to the different type of forcing mechanisms; LLJs due to synoptic-scale baroclinicity, which tend to have stronger wind speeds, are less likely to develop in polar regions than in the mid-latitude storm tracks.

LLJs occur at higher altitudes over sea than over land (Figure 2c). The lowest LLJs (50–200 m above ground) are found in regions with large horizontal gradients in topography such as Greenland, the Canadian Arctic Archipelago, parts of Siberia and in the mountainous regions on the Siberia/Mongolia/Kazakhstan border between 80–100°E and 45–55°N. These LLJs are assumed to occur due to katabatic flows because of the high frequency of occurrence and the low height of the wind speed maximum. The highest LLJs (450–550 m above ground) occur over oceans, western Eurasia, and eastern parts of North America.

3.2. Sea-ice effects

We analyse the frequency of LLJ occurrence when the sea-ice extent is at a maximum (March, Figure 3(a)) and in October (Figure 3(b)), when the sea-ice cover is still close to its September minimum but the ice surface has already cooled generating shallow baroclinic zones near the ice margins. The spatial pattern of the

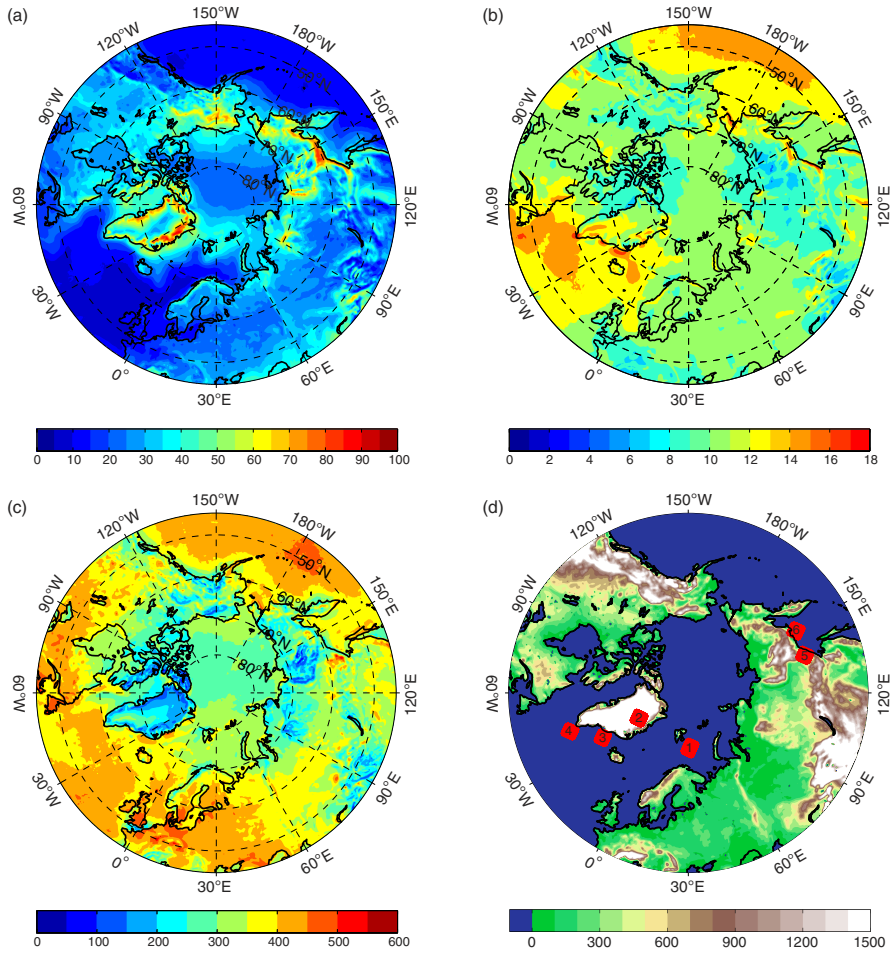

Figure 2. The 11-year mean (a) frequency of low-level jet (LLJ) occurrence (percentage of times when LLJs were observed), (b) the speed of detected LLJs ($m\,s^{-1}$) and (c) the height of detected LLJs (m). Data from October to March for the years 2000–2010 are included. (d) Topography (m). The numbered red squares show the groups of grid points which are analysed in more detail in Figures 4 and 5.

frequency of LLJ occurrence differs between October and March; in October the higher frequencies retreat closer to the North Pole as does the sea ice. In many regions in March (Figure 3(a)), the frequency of LLJ occurrence is high near the sea-ice edge but is enhanced on the sea-ice side compared to on the open water side. These LLJs arise as there are strong shallow baroclinic zones near the sea-ice edge which induce baroclinically forced LLJs and thus locally enhance the frequency of LLJ occurrence in the vicinity of the sea-ice edge. In addition, inertial oscillations during warm-air advection over the cold ice surface may generate LLJs over the sea ice but near the sea-ice edge (Tisler *et al.*, 2008).

There are several areas where sea ice is present in March but not in October and the frequency of LLJ occurrence is notably higher in March (Figure 3(a)) than in October (Figure 3(b)). Such areas are Hudson Bay, Baffin Bay, Barents Sea, Kara Sea, Sea of Okhotsk, Bering Sea and Chukchi Sea. The sea-ice margin is located within or near these sea areas, except in the case of Hudson Bay. Hudson Bay is completely covered with sea ice in March (Figure 3(a)) and thus the boundary layer will be mainly stably stratified. This, combined with the location of Hudson Bay far from either shallow baroclinic zones induced by the sea-ice edge or baroclinic zones related to the common occurrence of synoptic-scale weather systems, suggests that the LLJs which occur in Hudson Bay in March are mostly due to inertial oscillations (orographic effects may be important near the coasts).

The remaining areas mentioned above have sea ice present in March but not in October and are also located much closer to the sea-ice edge in March than in October. Thus, it is likely that LLJs over these areas are mainly forced by shallow, persistent baroclinic zones induced by the sea-ice edge. In contrast, in the Beaufort

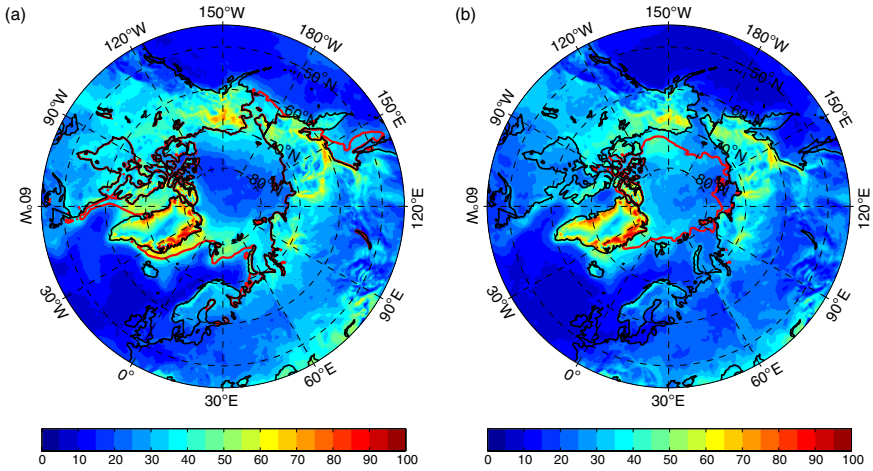

Figure 3. The frequency of low-level jet occurrence (colours) in (a) March and (b) October. The sea-ice edge, defined as the 11-year mean sea-ice concentration greater than 0.5 is shown by the red contour.

Sea the frequency of LLJ occurrence is clearly higher in October than in March. However, in October the sea-ice edge, and hence a shallow persistent baroclinic zone, is located in the Beaufort Sea whereas in March the area is completely covered by sea ice. In the central Arctic, sea ice is present in both March and October, however the frequency of LLJ occurrence is lower in March (15–20%) than in October (20–30%). The explanation may be that in March the shallow baroclinic zone due to the sea-ice edge and baroclinicity associated with the common occurrence of synoptic-scale cyclones is further away than in October (Serreze and Barry, 2005, Chapter 4). Therefore, there are fewer forcing mechanisms for LLJs in the central Arctic in March than in October.

The characteristics of LLJs occurring in one localized region along the edge of the sea ice are investigated in more detail to better understand the forcing mechanism. The area under investigation is southeast of Svalbard, shown as the red area marked 1 in Figure 2(d). This area, and the other red areas marked in Figure 2(d) (discussed in subsequent sections), contain approximately 50 grid points and therefore covers an area of approximately 200 km^2. We focus on March, when the sea-ice edge is located in this area, and on October when the sea-ice edge is further north. In March, most of the LLJs are parallel to the sea-ice edge (Figure 4(a)). Accordingly, the colder air mass is located to the right of the wind vector demonstrating that the LLJs are baroclinically forced as in this reverse shear situation thermal wind balance states that wind speed must decrease with height. LLJs from the northeast occur at lower heights than those from the southeast which suggests that the latter LLJs have a different forcing mechanism. In October (Figure 4(b)), the direction of LLJs is much more variable as the sea-ice edge is no longer present and thus there is not a dominant forcing mechanism acting. In October, the most common direction of LLJs is from the east (Figure 4(b)). This may be due to the position on the northern side of the end of the storm track where low-level prevailing winds in October are from the northeast (not shown). It should also be noted that the frequency of LLJ occurrence southeast of Svalbard is higher in March (28%) than in October (20%, Figures 3 and 4).

3.3. Orographic effects

On the northeast coast of Greenland (red area marked 2 in Figure 2(d)), LLJs are remarkably low, primarily from the west and occur frequently (Figure 5(a)), and thus are likely due to katabatic flows. The spread in the LLJ direction is primarily because of variations in the direction and steepness of the topography slope but also due to variations in the boundary-layer stratification and geostrophic wind vector (Ball, 1960). No LLJs with an easterly wind direction (i.e. upslope) occur in this region. On the southeast coast of Greenland (red area marked 3 in Figure 2(d)), all LLJs are from the northeast (Figure 5(b)) and thus are parallel to the coastline, sea-ice margin and SST front. Overland (1984) showed theoretically that barrier winds may occur within a horizontal distance of the coastline, given by the Rossby radius of deformation, and Moore and Renfrew (2005) estimated for the southeast coast of Greenland a Rossby radius of deformation of ∼400 km. Therefore, the LLJs we identify close to the southeast coast of Greenland are barrier jets. However, the LLJs further away from the coast may be generated by the combined effects of barrier winds (important close to the coast) and baroclinicity (important close to the sea-ice edge and SST front, Vihma *et al.*, 1998). At the southern tip of Greenland (red area marked 4 in Figure 2(d)), there are two dominant directions for LLJs: from the northeast and northwest (Figure 5(c)). These LLJs are tip jets and reverse tip jets (Moore and Renfrew, 2005), respectively.

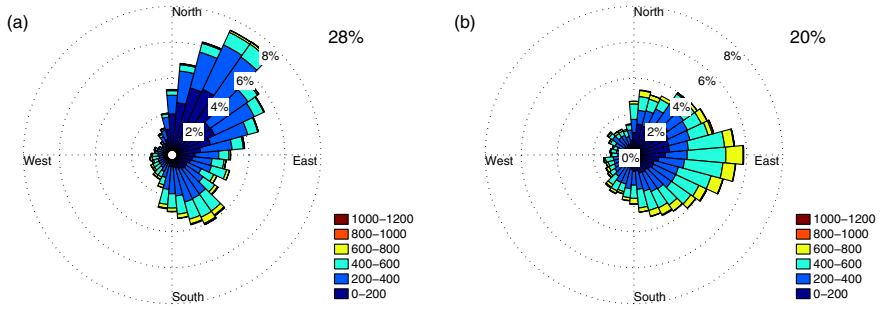

Figure 4. Wind roses for the occurrence of LLJs at the grid points near Svalbard (the red area marked 1 in Figure 2(d)) for (a) March and (b) October. The colours show the height (m) of the LLJs and the percentages in the top right corner of each panel indicate the percentage of time when a LLJ was identified.

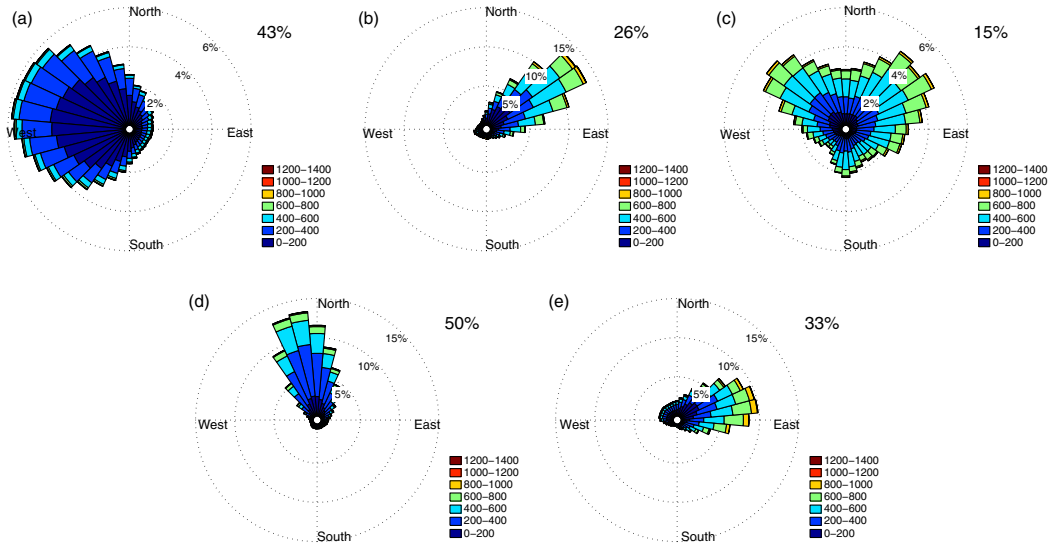

Figure 5. Wind roses for the occurrence of LLJs at the grid points (a) in the eastern part of Greenland (red area marked 2 in Figure 2(d)), (b) in the southeast coast of Greenland (marked 3 in Figure 2(d)), (c) near the southern tip of Greenland (marked 4 in Figure 2(d)), (d) over land along the southeast Russian coast (marked 5 in Figure 2(d)) and (e) over the northern part of the Sea of Okhotsk (marked 6 in Figure 2(d)). The colours show the height (m) of the LLJs and the percentages in the top right corner of each panel indicate the percentage of time when a LLJ was identified.

Over land, on the southeast Russian coast (red area marked 5 in Figure 2(d)), all LLJs are from the north-northwest (Figure 5(d)) and therefore are perpendicular to the coast and more importantly are parallel to the slope of the topography. The LLJs in this region are in general higher than the LLJs which occur in the northeastern part of Greenland (Figure 5(a)). However, the majority of LLJs near the southeast Russian coast occur below 400 m and therefore are most probably katabatic jets. Over the northern part of the Sea of Okhotsk (red area marked 6 in Figure 2(d)), all LLJs are from the east-northeast (Figure 5(e)) and thus are parallel to the coastline. The height distribution between Figure 5(b) and (e) are nearly identical, LLJs are from a narrow range of angles in both areas, and the topography of these two areas is similar (steep topography onshore). Thus it is likely that the LLJs over the Sea of Okhotsk, but close to the coast, are barrier jets, while further away from the coastline, barrier winds and baroclinicity both contribute to the formation of LLJs.

3.4. Comparison to previous studies

Overall, our results are in good qualitative agreement with previous studies. However, quantitative comparisons with previous similar studies are challenging due to differences between the time of interest, spatial coverage and LLJ identification criteria. Ranjha *et al.* (2013) investigated coastal LLJs based on ERA-Interim reanalysis. Their study covers the years 1980–2011 and their results for LLJ frequency of occurrence in the Arctic area during the cold season (December–February) has a similar spatial pattern

to that shown in Figure 2(a). Their LLJ frequency values on the sea-ice edges and over the central Arctic are approximately 5–15% lower than the frequencies calculated in this study in the same areas, however, both studies show lower frequencies in the central Arctic compared to near the sea-ice edge. Ranjha *et al.* (2013) found the highest LLJ frequencies over the eastern coast of Greenland similarly to this study, but their values are again lower than revealed from ASR. Differences between the frequency values may be due to different LLJ identification criteria used in these studies.

The directional analysis conducted for areas 3 and 4 (Figure 2(d)) agrees well with the results of Moore and Renfrew (2005). Our results show similar characteristics of the barrier flow along the southeast coast of Greenland and are also able to capture the tip jets and the reverse tip jets around the southern tip of Greenland. Moore and Renfrew (2005) found extremely strong LLJs (up to $50\,\mathrm{m\,s^{-1}}$) along the southeast coast and around the southern tip of Greenland which are the same areas that the strongest LLJs in this study were found. The highest frequencies and the lowest LLJs in this study were found on the coastal areas of Greenland and these results compare well with the study by Cassano *et al.* (2001). They investigate the persistent katabatic flows over the coasts Greenland and found the strongest wind speeds over eastern, northern and western coasts of Greenland at the lowest model level, which agrees well with our results in Figure 2(a) and (c) that show almost persistent, shallow katabatic LLJs over the same areas.

Rife *et al.* (2010) studied nocturnal LLJs globally and found larger values of their LLJ index around and over southern parts of Greenland during January compared to July. Their results suggest that increased LLJ occurrence in the North Atlantic and southern parts of Greenland is due to enhanced synoptic activity during the winter months. The results of this study are difficult to compare to those of Rife *et al.* (2010) as the LLJ identification criteria used by Rife *et al.* (2010) rejects most of the LLJs in the polar area (e.g. persistent katabatic jets). This study also reveals some new locations where strong LLJs are frequent, almost persistent, and from where earlier studies are not available. Such areas are northeastern coast of Russia and northern Alaska.

4. Conclusions

An 11-year climatology of LLJs in the Northern Hemisphere mid-latitudes and polar regions during the cold season was created based on the Interim Arctic system reanalysis. Our analysis has shown that LLJs are more common over land than over open sea areas and that the vast majority of LLJs are associated with either sea ice or topography.

The frequency of LLJ occurrence is large near the sea-ice edge in many regions especially near Svalbard, in the Sea of Okhotsk and in the Bering Sea due to the presence of shallow, persistent baroclinic zones. However, the LLJ frequency of occurrence is enhanced on the sea-ice side compared to on the open water side. This asymmetry in the frequency of LLJ occurrence suggests that inertial oscillations in space may be important for the formation of LLJs near the sea-ice edge. In contrast, in Hudson Bay, which is covered by sea ice in March, the frequency of LLJs is high everywhere. Thus, LLJs which develop here are most likely due to inertial oscillations in stable boundary layers. In the central Arctic LLJs have a relatively low (20–25%, according to ASR-Interim) frequency of occurrence when all winter months are considered because of the lack of strong forcing mechanisms.

Our climatology demonstrates that topography leads to the formation of barrier winds, katabatic flows and tip jets which meet our LLJ criteria in many regions. Our results show that LLJs due to katabatic flows are common over the northeast coast of Greenland, that LLJs due to barrier winds are prevalent immediately adjacent to the southeast coast of Greenland and that LLJs due to tip jets and reverse tip jets occur at the southern tip of Greenland. These results are in good qualitative agreement with previous studies (e.g. Moore and Renfrew, 2005) demonstrating the reliability of the method used in this study. The results obtained in this study also highlight the presence of frequent LLJs in the Sea of Okhotsk region, which have undergone significantly less study than the LLJs in Greenland. LLJs due to katabatic flows were identified over land and barrier winds were identified over the sea. The barrier winds identified in the Sea of Okhotsk had similar characteristics to those observed along the southeastern coast of Greenland.

Finally it should be noted that quantitative differences in the characteristics of LLJs and their frequency of occurrence may exist between the results presented here and observations. Such differences are likely as all reanalysis data sets have some inadequacies in the vertical resolution or in the model's stable boundary-layer parametrization. However, this study, based solely on reanalysis data, is the first attempt to create a climatology of all types of LLJs over a large geographic area and has identified many regions for closer investigation using a combination of observations and high resolution modelling systems.

Acknowledgements

The work of MT and VAS was supported by the Academy of Finland (contract 272041) and the work of TV was supported by the Academy of Finland (contract 259537). We thank Chi-Fan Shih from UCAR for help with downloading the ASR-Interim data.

References

Baas P, Bosveld FC, Klein Baltink H, Holtslag AAM. 2009. A climatology of nocturnal low-level jets at Cabauw. *Journal of Applied Meteorology and Climatology* **48**: 1627–1642.

Ball FK. 1960. Winds on the ice slopes of Antarctica. *Antarctic Meteorology: Proceedings of the Symposium Held in Melbourne February*

1959, Australian Academy of Science, Dwyer LJ (eds). Pergamon Press: London; 9–16.

Blackadar AK. 1957. Boundary layer wind maxima and their significance for the growth of nocturnal inversions. *Bulletin of the American Meteorological Society* **38**: 283–290.

Bonner WD. 1968. Climatology of the low level jet. *Monthly Weather Review* **96**: 833–850.

Bromwich D, Kuo YH, Serreze M, Walsh J, Bai LS, Barlage M, Hines K, Slater A. 2010. Arctic system reanalysis: call for community involvement. *Eos Transactions* **91**: 13–14.

Bromwich DH, Wilson AB, Bai LS, Moore GWK, Bauer P. 2015. A comparison of the regional arctic system reanalysis and the global ERA-interim reanalysis for the Arctic. *Quarterly Journal of the Royal Meteorological Society*, doi: 10.1002/qj.2527.

Cassano JJ, Box JE, Bromwich DH, Li L, Steffen K. 2001. Evaluation of polar MM5 simulations of Greenland's atmospheric circulation. *Journal of Geophysical Research* **106**: 33867–33889.

Doyle JD, Warner TT. 1993. A three-dimensional numerical investigation of a Carolina coastal low-level jet during GALE IOP 2. *Monthly Weather Review* **121**: 1030–1047.

Higgins RW, Yao Y, Yarosh ES, Janowiak JE, Mo KC. 1997. Influence of the Great Plains low-level jet on summertime precipitation and moisture transport over the central United States. *Journal of Climate* **10**: 481–507.

Högström U, Smedman-Högström AS. 1984. The wind regime in coastal areas with special reference to results obtained from the Swedish wind energy program. *Bound-Layer Meteorology* **30**: 351–373.

Mitchell MJ, Arritt RW, Labas K. 1995. A climatology of the warm season Great Plains low-level jet using wind profiler observations. *Weather Forecasting* **10**: 576–591.

Moore GWK, Renfrew IA. 2005. Tip jets and barrier winds: a QuikSCAT climatology of high wind speed events around Greenland. *Journal of Climate* **18**: 3713–3725.

Overland JE. 1984. Scale analysis of marine winds in straits and along mountainous coasts. *Monthly Weather Review* **112**: 2530–2534.

Parish TR. 1982. Barrier winds along the Sierra Nevada mountains. *Journal of Applied Meteorology* **21**: 925–930.

Petersen GN, Renfrew IA, Moore GWK. 2009. An overview of barrier winds off southeastern Greenland during the Greenland Flow Distortion experiment. *Quarterly Journal of the Royal Meteorological Society* **135**: 1950–1967.

Ranjha R, Svensson G, Tjernström M, Semedo A. 2013. Global distribution and seasonal variability of coastal low-level jets derived from ERA-Interim reanalysis. *Tellus A* **65**, 20412, doi: 10.3402/tellusa.v65i0.20412.

Renfrew IA, Anderson PS. 2006. Profiles of katabatic flow in summer and winter over Coats Land, Antarctica. *Quarterly Journal of the Royal Meteorological Society* **132**: 779–802.

Rife DL, Pinto JO, Monaghan AJ, Davis CA, Hannan JR. 2010. Global distribution and characteristics of diurnally varying low-level jets. *Journal of Climate* **23**: 5041–5064.

Savijärvi H, Niemelä S, Tisler P. 2005. Coastal winds and low-level jets: simulations for sea gulfs. *Quarterly Journal of the Royal Meteorological Society* **131**: 625–637.

Serreze MC, Barry RG. 2005. *The Arctic Climate System*. Cambridge University Press, New York, NY.

Stensrud DJ. 1996. Importance of low-level jets to climate: a review. *Journal of Climate* **9**: 1698–1711.

Tisler P, Vihma T, Müller G, Brümmer B. 2008. Modelling of warm-air advection over Arctic sea ice. *Tellus* **60A**: 775–788.

Vihma T, Uotila J, Launiainen J. 1998. Air-sea interaction over a thermal marine front in the Denmark Strait. *Journal of Geophysical Research* **103**: 27665–27678, doi: 10.1029/98JC02415.

II

Reprinted, with permission, from
Journal of Applied Meteorology and Climatology, 56, 2577–2594,
doi:10.1175/JAMC-D-16-0411.1

Low-Level Jets over Utö, Finland, Based on Doppler Lidar Observations

MINTTU TUONONEN

Finnish Meteorological Institute, Helsinki, Vaisala Oyj, Vantaa, and Department of Physics, University of Helsinki, Helsinki, Finland

EWAN J. O'CONNOR

Finnish Meteorological Institute, Helsinki, Finland, and Meteorology Department, University of Reading, Reading, United Kingdom

VICTORIA A. SINCLAIR

Department of Physics, University of Helsinki, Helsinki, Finland

VILLE VAKKARI

Finnish Meteorological Institute, Helsinki, Finland

(Manuscript received 16 December 2016, in final form 16 June 2017)

ABSTRACT

Over two years of meteorological observations from Utö, a small island in the Finnish outer archipelago in the Baltic Sea, were used to investigate the occurrence and characteristics of low-level jets (LLJs) and the diurnal and seasonal variations in these properties. An objective LLJ identification algorithm that is suitable for high-temporal-and-vertical-resolution Doppler lidar data was created and applied to wind profiles obtained from a combination of Doppler lidar data and two-dimensional sonic anemometer observations. This algorithm was designed to identify coherent LLJ structures and requires that they persist for at least 1 h. The long-term mean LLJ frequency of occurrence at Utö was 12%, the mean LLJ wind speed was 11.6 m s^{-1}, and the vast majority of identified LLJs occurred below 150 m above ground level. The LLJ frequency of occurrence was much higher during summer (21%) and spring (18%) than in autumn (8%) and winter (3%). During winter and spring, the LLJ frequency of occurrence is evenly distributed throughout the day. In contrast, the LLJ frequency of occurrence peaks at night (1900–0100 UTC) during summer and during the evening hours (1700–1900 UTC) in autumn. The highest and strongest LLJs come from the southwest, which is also the predominant LLJ direction in all seasons. LLJs below 100 m are common in spring and summer, are weaker, and do not show a strong directional dependence.

1. Introduction

Here we define a low-level jet (LLJ) to be a localized maximum in the vertical profile of the horizontal wind that is usually observed in the lowest few hundred meters of the atmosphere. LLJs can be produced by a range of different mechanisms, and the characteristics of LLJs can vary considerably. In this study, a ''climatology'' of LLJs at Utö, a small island in the Finnish archipelago (Fig. 1), is created that incorporates both the frequency of occurrence and the characteristics of all LLJs, regardless of their forcing mechanism.

LLJs have been shown to transport moisture considerable horizontal distances and consequently to influence precipitation patterns and the hydrological cycle (e.g., Higgins et al. 1997). Likewise, pollutants can also be transported horizontally by LLJs, affecting air quality (Mao and Talbot 2004; Hu et al. 2013) and Su et al. (2016) showed that shear-driven turbulence associated with LLJs can transport aerosol and water vapor vertically, influencing cloud formation. Strong shear-driven turbulence below the jet can also have an effect on the surface fluxes of heat and moisture (Banta et al. 2002).

Corresponding author: Minttu Tuononen, minttu.tuononen@fmi.fi

DOI: 10.1175/JAMC-D-16-0411.1

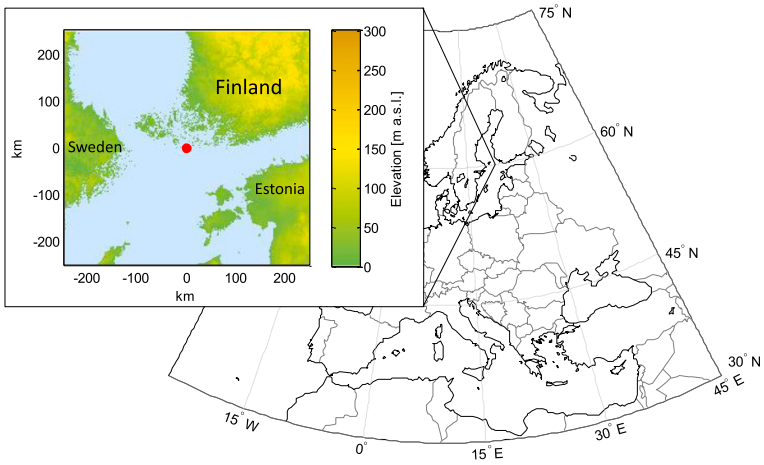

FIG. 1. Location of the Utö measurement site in the Finnish archipelago area. In the 500 km × 500 km topographic map insert for Utö (USGS 2010), the location of the measurement site is indicated by a red dot.

The recent increase in the number of installed wind turbines has also raised interest in LLJs: for example, in the Great Plains and Midwest of the United States (Banta et al. 2006, 2013; Storm et al. 2009; Storm and Basu 2010; Vanderwende et al. 2015), at onshore coastal sites in Denmark (Floors et al. 2013; Peña et al. 2016), and in offshore regions in the Gulf of Maine (Pichugina et al. 2012) and the Baltic Sea (Dörenkämper et al. 2015). Increased shear and associated turbulence related to LLJs are harmful for wind turbines and lower turbine lifetimes (Kelley et al. 2006), but the enhanced low-level wind speeds in the rotor sweep area are potentially beneficial for wind-power production. Therefore, accurate information about how frequently LLJs occur at a specific location, together with the characteristics of the LLJs, would be valuable when planning new wind farms (Kelley et al. 2006).

The occurrence, forcing mechanisms, and impacts of LLJs have been extensively studied over the past 50 years. It is now known that LLJs can develop via inertial oscillations in time (e.g., Blackadar 1957; Mitchell et al. 1995; Baas et al. 2009), large-scale baroclinicity (e.g., Kotroni and Lagouvardos 1993; Whiteman et al. 1997), coastal effects (e.g., Parish 2000; Ranjha et al. 2013; Orr et al. 2005), katabatic winds (e.g., Renfrew and Anderson 2006), and barrier winds (e.g., Parish 1982). Only a brief review of previous LLJ studies and LLJ forcing mechanisms is given here [see Stensrud (1996) and references within for a more complete overview].

The majority of the early observational LLJ studies took place in the United States. For example, Bonner (1968) analyzed observations from 47 rawinsonde stations and determined that LLJs most frequently occurred in the Great Plains. Numerous further studies (e.g., Mitchell et al. 1995; Whiteman et al. 1997) then analyzed the structure and forcing mechanisms for the LLJs that develop in the Great Plains; Mitchell et al. (1995) concluded that the strongest LLJs occurred near local midnight and that a diurnal oscillation in the wind speed and direction was present, indicating that inertial oscillations in time play an important role in the dynamics of these LLJs. These observations supported the theory of inertial oscillations in time proposed by Blackadar (1957). The acceleration of the horizontal wind speed occurs after sunset when the boundary layer undergoes a transition from a well-mixed state to a stably stratified state. The rapid decrease in convectively driven turbulent mixing and, as a consequence, the decay of friction disrupts the force balance among the pressure gradient force, the Coriolis force, and friction, which results in acceleration of the horizontal wind speed in the decoupled boundary layer. Extensive field campaigns have more recently taken place in the Great Plains region and have resulted in extensive knowledge of these nocturnal LLJs (e.g., Banta et al. 2006). Nocturnal LLJs forced by inertial oscillations in time have also been studied in Australia (May 1995) and in the Netherlands (e.g., Baas et al. 2009, 2012).

In comparison with in the United States, fewer LLJ studies, whether focusing on their climatological characteristics or on their forcing mechanisms, have taken place in northern Europe where our study is focused; as a consequence, less is known about LLJs in this region. In addition, many of the studies that have

examined LLJs in the Baltic Sea area have concluded that, unlike in the Great Plains area, LLJs are not predominantly forced by inertial oscillations in time. Högström and Smedman-Högström (1984), Smedman et al. (1993), and Smedman et al. (1995) investigated LLJs, their turbulent characteristics, and forcing mechanisms over the Baltic Sea during spring and summer. They concluded that LLJs occur frequently over the Baltic Sea in the warm season and that they are the result of an ''inertial oscillation in space,'' which is triggered by frictional decoupling at a coastline when relatively warm air passing over a nearby landmass flows out over much colder water. Such LLJs have also been identified elsewhere and are discussed in theoretical studies. Owinoh et al. (2005) and Orr et al. (2005) refer to these LLJs as thermal boundary layer jets and noted the similarity between these and the more classical nocturnal jet forced by temporal, rather than spatial, variations in atmospheric stability. When LLJs are generated by an upwind coastline, however, the acceleration of the wind speed depends on the horizontal distance from the step change in boundary layer stratification, and thus these LLJs usually have no diurnal cycle and cannot be identified from hodographs created from point observations of wind speed and direction. A step change in surface friction can also trigger the development of LLJs—for example, at a coastline when the wind flows from over rough land to smooth sea; such jets are referred to as frictional–Coriolis–buoyancy jets by Orr et al. (2005). More recent studies of LLJs in the Baltic Sea include Dörenkämper et al. (2015), who developed an LLJ climatology by using data from a 100-m mast in the central western Baltic Sea; they concluded that LLJs are most common in spring and least common in winter. In a modeling study, Svensson et al. (2016) showed that LLJs are common over the Baltic Sea and occur at lower heights (210–250 m) in spring than in winter (typically around 450 m).

Many early studies on LLJs analyzed rawinsonde observations (Bonner 1968; Whiteman et al. 1997). The advantages of such observations are their continuous nature (no data gaps) and their vertical extent. Disadvantages are primarily low temporal resolution—for example, Bonner (1968) based his study on twice-daily observations—and the limited number of observing stations. Studies have also analyzed LLJs using meteorological towers or masts (e.g., Dörenkämper et al. 2015), which tend to have good temporal and vertical resolution but are limited to the lowest 100–300 m of the atmosphere.

Remote sensing instruments have much better temporal resolution in comparison with radiosonde observations and provide vertical profiles that extend much farther into the troposphere in comparison with meteorological masts. As a consequence, active remote sensing instruments have been used considerably in more recent LLJ studies. For example, multiple years of wind profiler data were utilized by May (1995) and Song et al. (2005), and Baas et al. (2009) combined 7 years of meteorological mast and wind profiler observations at Cabauw in the Netherlands. Sodar data have also been used to determine the occurrence and characteristics of LLJs—for example, in Florida (Karipot et al. 2009) and in Moscow (Kallistratova and Kouznetsov 2012). High-resolution Doppler lidar has proven to be an ideal instrument to measure vertical wind profiles (Banta et al. 2002, 2013), and Doppler lidar systems have even been deployed on ships (Tucker et al. 2010; Pichugina et al. 2012), enabling the investigation of LLJs in marine locations.

Many of these remote sensing studies have been conducted using research instruments. Although such research instruments clearly provide high-quality observations, it appears to be common to deploy them on short-term field campaigns rather than to operate them at the same location for multiple years at a time. In our study, we use a Doppler lidar that is part of the Finnish Meteorological Institute (FMI) operational ground-based remote sensing network (Hirsikko et al. 2014), the main purpose of which is to monitor winds, air pollution, and boundary layer properties in near–real time. Hence, this Doppler lidar provides a long time series of observations but has a scan strategy that is not optimized for identifying LLJs.

The first aim of this study is to create an objective LLJ identification algorithm. Many previous LLJ studies have developed automated algorithms to identify LLJs from a range of datasets, and we build on these earlier studies (Bonner 1968; Whiteman et al. 1997; Baas et al. 2009; Tuononen et al. 2015). The algorithm developed in this study differs somewhat from earlier algorithms, because it is specifically designed to identify LLJs from high-temporal-and-vertical-resolution operational Doppler lidar data obtained in the particularly clean environment of Utö (the strength of the Doppler lidar signal depends on the scattering from aerosol particles; a clean atmosphere may have too few aerosol particles present to provide sufficient signal). The second aim is to investigate the occurrence and diurnal and seasonal variability of LLJs as well as the LLJ characteristics at Utö, which may be a potential area for future production of wind power.

The paper is structured as follows: A description of the measurement site and lidar observations is given in section 2. The LLJ identification algorithm is discussed

in detail in section 3. Section 4 includes the results of the LLJ occurrence and characteristics at Utö as well as information on the dependence of these results on thresholds applied in the LLJ detection algorithm. In section 5, a brief comparison of our results with earlier studies in the Baltic Sea is given. An optimal scanning scheme for LLJ identification is discussed in section 6, before the conclusions are presented in section 7.

2. Observations

a. Measurement station and data period

Utö is a small, flat island in the Finnish outer archipelago (59.78°N, 21.37°E), located about 80 km from the southwestern tip of the Finnish mainland (Fig. 1). The total area of the island is 0.81 km^2, with the highest point less than 20 m above mean sea level (MSL). Utö is the southernmost island of the Finnish archipelago. To the north, between Utö and the Finnish mainland, there are many islands; to the south the Baltic Sea opens out (Fig. 1). Utö is not located close to the mainland coastlines of Finland, Estonia, or Sweden.

Solar noon at Utö is UTC + 1.4 h. During summer months, the earliest sunrise is at 0413 local time and the latest sunset is at 2300 local time. In contrast, in winter, sunrise is around 0930 and the sun sets around 1530 local time. The lowest monthly mean temperature, −2.2°C, is observed in February, and the highest monthly mean temperature, +16.7°C, is observed in July (Pirinen et al. 2012).

Vertical profiles of horizontal wind obtained from a scanning Doppler lidar were the primary data used for this study, supplemented with two-dimensional (2D) sonic anemometer observations from a nearby tower. Data for this study were gathered quasi continuously from 1 January 2013 to 4 May 2015, with 118 days of data missing because of maintenance and other issues, mostly during spring/summer 2014. Sea ice was not observed near Utö during this study except for a short period in early 2013. The highest sea ice concentrations were observed between 25 February and 14 April 2013, but the Doppler lidar was not operating between 8 March and 5 April 2013.

b. Doppler lidar observations

Vertical profiles of horizontal wind speed and direction were obtained from a Halo Photonics Stream Line Doppler lidar operating routinely as part of the FMI Doppler lidar network (Hirsikko et al. 2014). This instrument operates at a wavelength of 1.5 μm and uses the heterodyne technique to detect the Doppler shift. The pulse repetition frequency was 15 kHz, pulse length was 200 ns, and line-of-sight resolution was 30 m. A total of 320 range gates gives a potential range of 9.6 km, but useful signals are typically limited to much closer ranges because of insufficient numbers of aerosol or cloud particles in the atmosphere. Liquid clouds are excellent targets, but, because they also strongly attenuate the lidar signal, those signals are limited to cloud base and do not penetrate more than a few hundred meters into the cloud. The instrument provides profiles of signal-to-noise ratio and radial Doppler velocity at a user-selected temporal resolution. Postprocessing then applies background corrections to the signal-to-noise ratio (Manninen et al. 2016), and uncertainty estimates for the radial Doppler velocities are obtained directly from the corrected signal-to-noise ratio by using an approximation to the Cramér–Rao lower-bound method (Rye and Hardesty 1993) given in O'Connor et al. (2010). Unreliable radial Doppler velocities are identified by applying the standard operational signal-to-noise ratio threshold of −21 dB; that is, each radial velocity measurement with a signal-to-noise ratio of less than −21 dB has an intrinsic measurement uncertainty of $>0.15\ m\ s^{-1}$ and is discarded.

The Doppler lidar was deployed at 3 m above ground level (AGL) (8 m MSL) and was configured with a scan schedule that included wind scans interspersed with vertical stare and other scans. The wind scans were composed of a Doppler beam swing (DBS) scan and a low-level velocity–azimuth display (VAD) scan (Fig. 2a). The three-beam DBS scan was performed every 10 min and consisted of one beam pointing toward vertical and two orthogonal beams at 70° elevation (from horizontal) (Fig. 2a). The low-level VAD scan was performed every 30 min at 4° elevation and contained 24 beams (one every 15° in azimuth) (Fig. 2a). All wind scans were obtained with a large number of accumulated pulses per beam (>75 000) to ensure high accuracy. One low-level VAD scan takes 2 min to complete, and one three-beam DBS scan takes 1 min. Together with other scans, this leaves about 45 min per hour for vertically pointing operation (Fig. 2c). It is important to note that the instrument scanning schedule that was implemented was designed for other operational requirements and has not been optimized for LLJ studies.

c. Deriving vertical profiles of the horizontal wind

The horizontal wind speed and direction are obtained from DBS (Henderson et al. 2005; Lane et al. 2013) and VAD (e.g., Päschke et al. 2015) scans by using trigonometry and assuming that no major changes occur within the scanning volume (Fig. 2b). Uncertainties in the derived horizontal wind speed and direction are then obtained through propagation of the radial Doppler

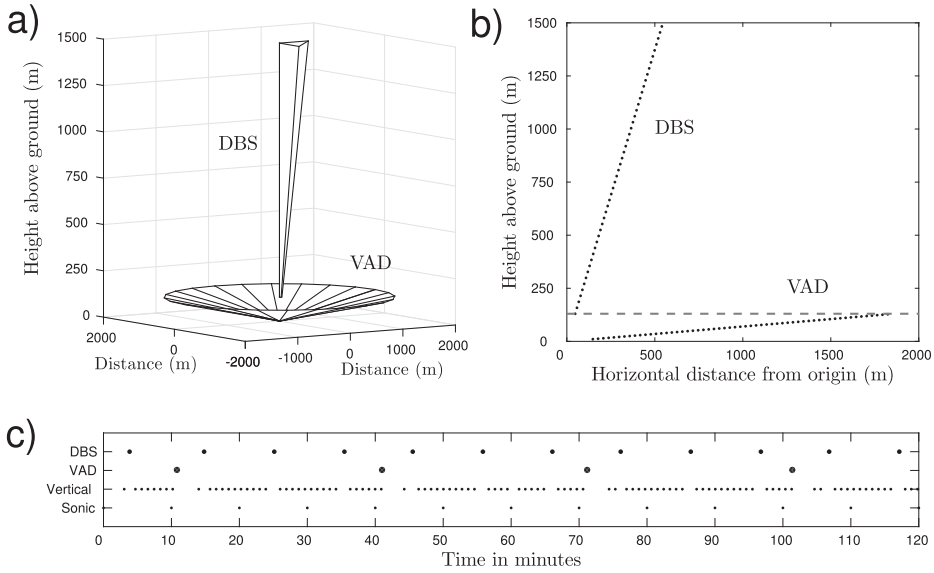

FIG. 2. A schematic drawing that describes scan sequence and scans that are concatenated to create the wind-profile dataset. (a) Illustration of the two Doppler lidar scanning patterns used in this study. Point (0, 0, 0) represents the measurement site. (b) Horizontal and vertical distance from origin for each off-zenith beam from VAD (below 130 m AGL) and DBS (above 130 m AGL) scans. The horizontal dashed line indicates the height level at which the scan pattern used changes from VAD to DBS (at 130 m AGL). (c) Measurement interval for each dataset (DBS scan, VAD scan, vertically pointing operation, and sonic anemometer) used in this study during a 2-h sample period, indicating the effective temporal resolution of each dataset.

velocity uncertainty estimates (e.g., Päschke et al. 2015). Both DBS and VAD methods for obtaining winds assume horizontal homogeneity and stationarity in the wind field, which may not be appropriate in highly turbulent situations (Koscielny et al. 1984). The VAD method proposed by Päschke et al. (2015) uses a quality metric that is based on the coefficient of determination for the sine fit, together with an estimate of the collinearity of the data, to determine reliable data. Such a metric is not available for winds derived from DBS scans, and therefore we use the standard deviation σ_w of the vertical wind to diagnose the presence of turbulence that is sufficient to bias the DBS measurements. The σ_w is calculated from the vertically pointing data from before and after the DBS scan, using a sliding window of 30 min and three range gates centered on each height in the wind profile to ensure a sufficient number of samples for a reliable estimate. The threshold value for σ_w above which wind profiles were discarded for being unreliable was empirically determined to be 0.20 m s^{-1}. Similar values for estimating turbulent situations by Doppler lidar have been used, for example, in Hogan et al. (2009) and Tucker et al. (2009).

The full vertical profile of the horizontal wind is then obtained by concatenating the wind profiles provided by both VAD and DBS Doppler lidar scans. At 2-km radius, the VAD scan at an elevation of 4° from horizontal reaches an altitude of 140 m. Since the maximum range of the VAD scan was typically less than 2 km, we create the concatenated wind profile by limiting the VAD scan to 130 m AGL and then stacking the DBS scan (from 130 m AGL) on top of the VAD scan (Figs. 2a,b). Thus, the lowest measurement height that we use from the low-level VAD scan is 10.3 m AGL, which corresponds to a radius of 148 m, and the lowest height for the DBS scan is 130 m AGL, at which height the off-zenith beams have a horizontal distance of 47 m from the instrument (Fig. 2b). Ten-minute-averaged winds from the 2D sonic anemometer at 20 m AGL were inserted into the concatenated profile at the appropriate height level, and the VAD and 2D sonic anemometer data were interpolated in time to match the DBS time series (data every 10 min).

d. Data availability and quality

The VAD scan is often limited to ranges that are much closer than 2 km because of low aerosol concentrations or intervening cloud and precipitation, and this situation means that there can be gaps in the concatenated wind profile between the highest altitude available from the VAD scan and the first measurement

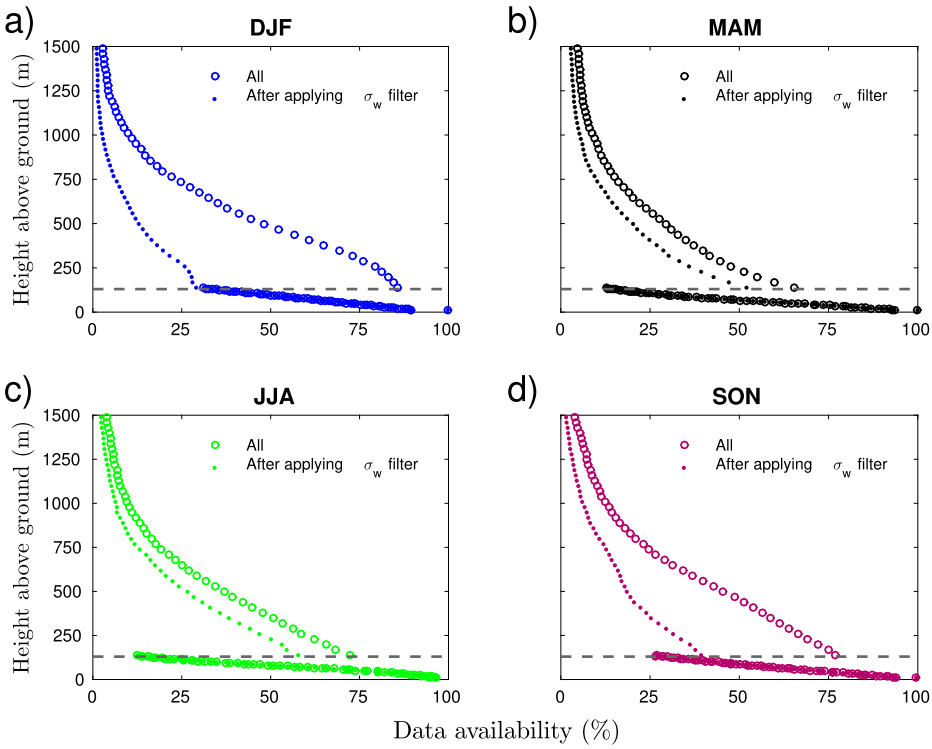

FIG. 3. Concatenated wind-profile data availability vs height above ground for each season: (a) December–February (DJF), (b) March–May (MAM), (c) June–August (JJA) and (d) September–November (SON), before and after applying the σ_w threshold to discard unreliable turbulent wind measurements. Data availability represents the percentage of valid data at each height relative to the total number of observations. Altitudes below 130 m AGL correspond to VAD (and 2D sonic anemometer) data availability; altitudes above 130 m AGL correspond to DBS data availability. The horizontal dashed line indicates the height level at which the scan pattern that is used changes from VAD to DBS (at 130 m AGL).

altitude from the DBS scan. The seasonal data availability for the combined dataset is presented in Fig. 3 and clearly shows the challenge of obtaining signal in a clean atmosphere with a shallow boundary layer. Data availability decreases with range in all seasons, as expected, for both DBS and VAD scans. Clearly visible in Fig. 3 is the considerable impact that applying the σ_w threshold has on DBS data availability, with up to 70% of DBS data with good signal being discarded in winter and 27% being discarded in summer. That turbulent conditions can reduce the number of reliable wind profiles in good signal conditions was also noted by Päschke et al. (2015). Data availability before applying the σ_w threshold was higher in winter and autumn, whereas after applying the σ_w threshold the data availability was lowest in winter. Very few turbulent issues were noted in the VAD scans—a fact that was attributed to the low elevation of the scanning angle. We do not expect LLJs to be present during strong convectively driven turbulent conditions, however, and therefore the discarding of a significant portion of the DBS data should not affect the true LLJ climatology. The potential impact of the data availability on the LLJ climatology is discussed in section 3.

It is clear that the 4°-elevation VAD scan, 70°-elevation DBS scan, and 2D sonic anemometer are not measuring the same volume, with each measurement type representing different atmospheric scales. For example, at 127 m in altitude the VAD scan radius is 1.8 km, whereas at 130 m in altitude the horizontal distance for the off-zenith DBS beams is 47 m (Fig. 2b). To check whether this method of creating a concatenated wind profile was valid, in Fig. 4a the winds obtained from the 2D sonic anemometer were compared with the VAD winds closest to the anemometer height. In addition, in Fig. 4b the wind speed from the lowest DBS height (130 m AGL) was

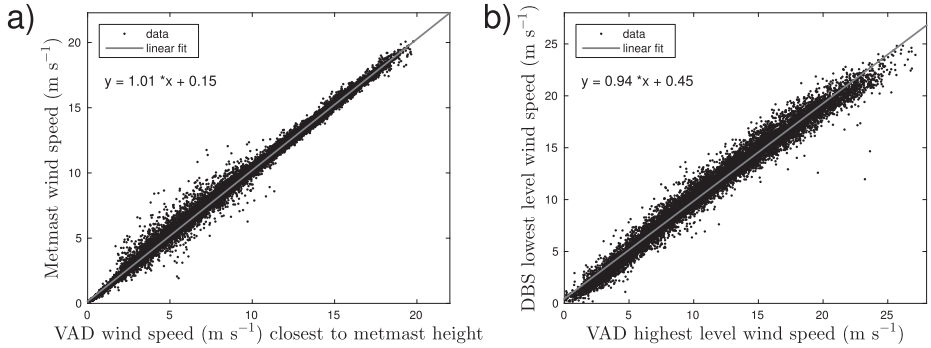

FIG. 4. (a) Comparison of 2D sonic anemometer wind speed from the meteorological mast (at 20 m AGL) and Doppler lidar VAD wind speed from the height that is closest to that 2D sonic anemometer measurement height (21 m AGL), and (b) comparison of Doppler lidar DBS wind speed at the lowest available level (130 m AGL) and Doppler lidar VAD wind speed at the highest level that was used (128 m).

compared with the wind speed from the closest VAD range gate to this height (128 m AGL). Both comparisons showed minimal bias, with a root-mean-square error for the VAD–DBS comparison of $0.87\,\mathrm{m\,s^{-1}}$ and a root-mean-square error of $0.29\,\mathrm{m\,s^{-1}}$ for the VAD–2D sonic anemometer comparison. These values give us confidence that, at this location and despite the differences in the measurement volumes, the method used to obtain a concatenated wind profile is suitable for diagnosing LLJs.

3. Low-level-jet identification algorithm

The LLJ identification algorithm consists of two parts, 1) main criteria and 2) threshold criteria, that were applied to the quality-controlled concatenated wind-profile data. The main criteria are used to find all low-level wind speed maxima in each wind profile. The threshold criteria result in coherent LLJ cases, without sudden jumps in LLJ height, wind speed, and wind direction, and ignore individual wind speed maxima that should not be identified as LLJ cases. The algorithm logic is as follows.

For each wind profile, all local wind speed maxima and minima below 1510 m are identified. After finding all local maxima and minima, the main criteria are applied to each wind profile that contains at least one local maximum: if a local maximum is both at least $2\,\mathrm{m\,s^{-1}}$ stronger and at least 25% stronger than the local minima below and above the local maximum, the local maximum will be denoted as a low-level wind speed maximum. The main criteria are checked for all local maxima in each profile. Up to three low-level wind speed maxima are permitted in each individual wind profile, allowing multiple LLJs, at different heights, to be identified within a single profile.

After finding all low-level wind speed maxima, the threshold criteria are applied. An individual profile with at least one low-level wind speed maximum that meets all of the thresholds is then designated as an LLJ profile. One LLJ case is defined to be a quasi-continuous time series of LLJ profiles, and therefore every LLJ profile belongs to an LLJ case. The threshold criteria ensure that an LLJ case consists of LLJ profiles that have similar characteristics and thus are coherent features without any large or sudden changes in height, speed, or direction. It also allows short time gaps in the data. All subjectively chosen thresholds (labeled 1–4 below) are checked simultaneously and must be fulfilled as follows:

1) The height difference (Δh in Fig. 5a) between two consecutive low-level wind speed maxima must be smaller than 135 m. This absolute threshold value corresponds to the height of four range gates in the Doppler lidar DBS data.
2) The wind speed difference (Δws in Fig. 5b) between two consecutive low-level wind speed maxima must be smaller than 30%. This relative value allows larger absolute differences when the wind speed is high and smaller absolute differences with low wind speed.
3) The wind direction difference (Δwd in Fig. 5c) between two consecutive low-level wind speed maxima must be smaller than 45°.
4) The time difference (Δt in Fig. 5d) between two consecutive low-level wind speed maxima must be smaller than 1 h. This absolute value will allow some missing wind profiles (i.e., data gaps) between two consecutive LLJ profiles in the same LLJ case.

If any one of the thresholds 1–4 described above is not fulfilled, the low-level wind speed maximum being

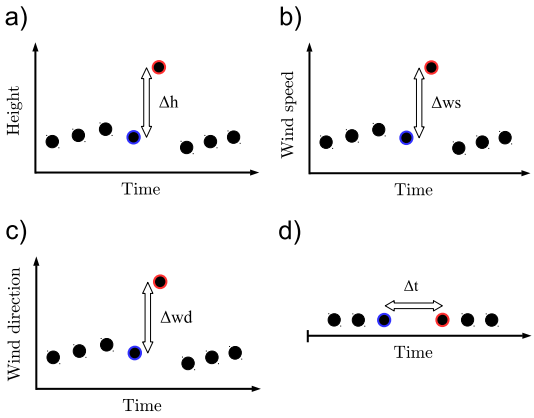

FIG. 5. A schematic drawing that describes the different threshold criteria used for identifying LLJ profiles on the basis of (a) height, (b) wind speed, (c) wind direction, and (d) time differences between two consecutive low-level wind speed maxima (Δh, Δws, Δwd, and Δt, respectively). Filled black circles represent low-level wind speed maxima fulfilling the main criteria described in section 3. Each low-level wind speed maximum (e.g., red-edged profile) is compared with the previous low-level wind speed maximum (blue-edged profile) and differences (Δh, Δws, Δwd, and Δt) between these consecutive low-level wind speed maxima are tested against the threshold values simultaneously. If any difference values (Δh, Δws, Δwd, or Δt) between two consecutive low-level wind speed maxima are larger than the given threshold value, the low-level wind speed maximum does not belong to the same LLJ case as the previous LLJ profile.

tested does not belong to the same LLJ case as the earlier low-level wind speed maxima that fulfilled the criteria. Furthermore, the low-level wind speed maximum that did not fulfill the threshold criteria is not rejected until it is verified that it is not the initial low-level wind speed maximum of a new LLJ case. Each LLJ case is labeled with a running number, and therefore it is possible to calculate the estimate of the duration of each LLJ case. In addition, it is required that each LLJ case must last at least 1 h; this ensures that only coherent LLJ structures are detected and prevents isolated individual profiles that happen to meet the rest of the criteria from being identified as an LLJ case.

The principles behind the main criteria are very similar to those presented in previous studies. The LLJ criteria used by Bonner (1968) and Whiteman et al. (1997) used stricter thresholds for the LLJ maximum and falloff above the maximum; however, these studies did not test for a minimum below the maximum. In contrast, the algorithm by Banta et al. (2002) consisted of looser absolute thresholds for LLJ maximum and falloffs for the minima, both below and above the maximum. Andreas et al. (2000) used an absolute criterion that was similar to that used in this study, but they did not use a relative falloff criterion for the minima. The main criteria are also similar to those applied by Baas et al. (2009) and Tuononen et al. (2015), consisting of both absolute and relative criteria with similar magnitudes. High temporal resolution permits testing the persistence of the LLJ, with a requirement that is similar to that imposed by Baas et al. (2009). The additional threshold criteria employed here have been designed specifically for high-resolution Doppler lidar data to enable the identification of coherent LLJ cases rather than individual LLJ profiles.

On applying the main and threshold criteria to strict quality-controlled Doppler lidar wind-profile data, it can be seen that the algorithm is capable of objectively identifying LLJ cases (Fig. 6). In some situations in which the air is very clean or clouds are present, the Doppler lidar signal is too weak and therefore wind measurements, especially at higher altitudes in the atmosphere, are missing. Missing data are shown in white in Fig. 6, and there is often a small gap in the concatenated profile after combining the VAD and DBS scans, as seen around the heights below 200 m in Fig. 6. This occurs because there is not enough signal in the VAD scan at far ranges, as shown in the data-availability plot (Fig. 3). Data gaps may also exist as a result of the instrument conducting other scan types as part of its operational routine. The algorithm detects an LLJ case when all criteria are fulfilled but may discard some viable cases as a result of data gaps even though the LLJ likely continues during the data gap. Such cases are potentially visible in Fig. 6b. An LLJ is detected at 0000 UTC 17 May 2013 and continues until 0500 UTC 17 May 2013, but, between 0500 and 1100 UTC 17 May 2013, there are no data available above 100 m AGL and, therefore, no LLJ is identified by the algorithm, even though it is likely that the LLJ persisted through this period. A similar situation also occurs in the evening between 1630 and 2100 UTC 17 May. Because of data limitations, such as operational data gaps and inability to observe the entire wind profile in all weather situations with the Doppler lidar (such as in the presence of low clouds), the LLJ duration calculation is only suggestive and should be taken as a lower limit. How data limitations and data availability can affect the LLJ statistics presented here is also discussed in section 4.

4. LLJ characteristics over Utö, Finland

a. LLJ frequency of occurrence

On the basis of more than 2 years of Doppler lidar data, the LLJ frequency of occurrence at Utö is 12%, calculated by dividing all identified LLJ profiles by the number of observed wind profiles. At Utö, LLJs are more common

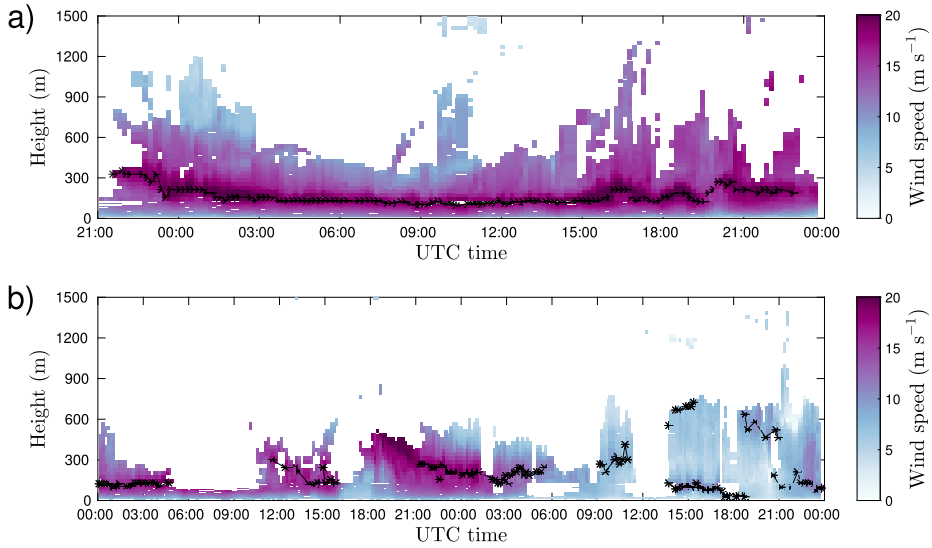

FIG. 6. Time–height plots of horizontal wind speed derived from Doppler lidar data at Utö (a) between 2100 UTC 20 May 2013 and 0000 UTC 22 May 2013 and (b) between 17 and 18 May 2013. Horizontal wind speed is given by the color shades; white regions denote missing wind speed data due to lack of signal. Black stars denote LLJ profiles, with black lines linking appropriate LLJ profiles into an LLJ case.

during spring and summer than in winter and autumn (Fig. 7a); the LLJ frequency of occurrence is highest between March and August and is lowest between November and February, with a maximum in July (28%) and a minimum in December (2%). The values of LLJ frequency of occurrence corresponding to each month, season, or hour are normalized by the number of wind profiles measured during each month, season, or hour. Therefore, the values of LLJ frequency of occurrence account for the variation in the number of observed wind profiles. Multiple LLJs (i.e., more than one low-level wind speed maximum belonging to separate LLJ cases in one wind profile) were found in 0.1% of all wind profiles, corresponding to 1% of all LLJ profiles.

There is little diurnal variation in LLJ frequency of occurrence during winter and spring (Fig. 7b), but the mean LLJ frequency of occurrence is 15% higher in spring than in winter. Some diurnal variation is present during summer, with LLJ frequency of occurrence enhanced at night, by up to 15%, and in autumn, when LLJs are up to 8% more common in the early evening. Note that all values of LLJ frequency of occurrence should be considered as a lower bound because of the data limitations, as discussed in section 3.

b. *LLJ characteristics*

The LLJ height (Table 1) is usually lowest in summer (median LLJ height 104 m) and highest in winter (median LLJ height 243 m). Figure 8a shows the distribution of LLJ heights observed in each season. The vast majority of LLJs identified are below 200 m, with a peak occurrence observed between 130 and 200 m. The observed LLJ height distribution in spring is very similar to that of summer, with low (below 100 m) LLJs being common. During autumn, there are more LLJs at higher levels and, similar to what is observed in winter, far fewer LLJs identified below 100 m. Figure 8a shows that many LLJs occur between 130 and 200 m, corresponding to the three lowest DBS levels, but, in reality, the true wind maximum may occur slightly below 130 m. This is a consequence of the low VAD data availability at far ranges (Fig. 3) relative to the DBS data availability at near ranges; the LLJ maximum is likely to be observed at the first available DBS range gates (from 130 m AGL above) in which there is much more signal. There is a larger jump in data availability between the farthest VAD range and the first DBS range in spring and summer (Figs. 3b,c), which may explain the strong peak in LLJ occurrence at the lowest DBS levels in spring and summer. Thus, interpreting the distribution of LLJ height should be made in reference to the data availability at each height.

The mean LLJ wind speed is 11.6 m s^{-1} (standard deviation of 4.3 m s^{-1}) with a median value of 10.8 m s^{-1}, a result of a slightly positively skewed LLJ wind speed distribution (Table 1). The median wind speeds in autumn

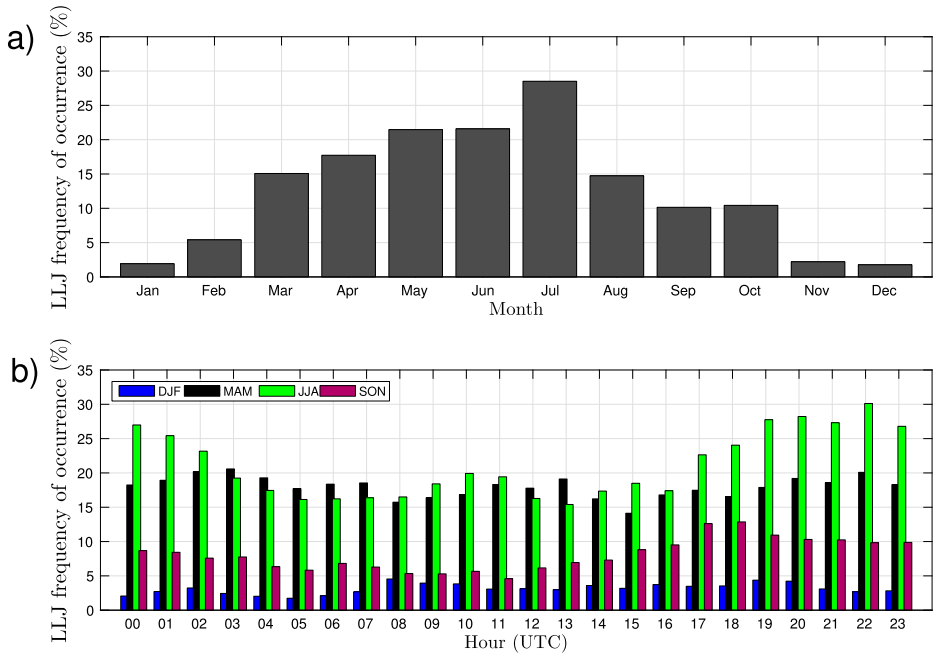

FIG. 7. Histograms that show (a) monthly variation of LLJ frequency of occurrence and (b) hourly variation of LLJ frequency of occurrence, separated by season. Each bar is normalized by the number of wind profiles of the corresponding month or hour.

(10.0 m s^{-1}) and in summer (10.6 m s^{-1}) are weaker than in winter (11.8 m s^{-1}) and in spring (11.4 m s^{-1}). The LLJ wind speed distribution also varies from season to season (Fig. 8b), with a narrow distribution in summer and broader distributions with longer tails toward stronger wind speeds during other seasons. The wintertime distribution is particularly broad.

Three wind directions dominate LLJ occurrence over Utö: 1) east–east-southeast, 2) south-southwest–west, and 3) north–northwest (Fig. 8c). All three directions are well represented during spring and summer months, whereas during winter months the dominant LLJ direction is from the south-southwest. In autumn, the most common direction for LLJ occurrence is from the southwesterly sector, together with a slight increase in LLJ occurrence from the southeast.

The LLJ bulk speed shears below and above the LLJ are respectively defined as

$$\alpha_{\text{below}} = \frac{U_{\text{LLJ}} - U_{\text{min,below}}}{h_{\text{LLJ}} - h_{\text{min,below}}} \quad \text{and} \tag{1}$$

$$\alpha_{\text{above}} = \frac{U_{\text{min,above}} - U_{\text{LLJ}}}{h_{\text{min,above}} - h_{\text{LLJ}}}, \tag{2}$$

where U_{LLJ} is the LLJ wind speed, $U_{\text{min,below}}$ and $U_{\text{min,above}}$ are respectively the wind speeds of the minima below and above the LLJ, h_{LLJ} is the LLJ height, and $h_{\text{min,below}}$ and $h_{\text{min,above}}$ are respectively the heights of the minima below and above the jet. Median values of bulk speed shear above and below the jet are −0.019 and 0.048 m s^{-1} m^{-1} (Table 1), respectively, and the distributions of LLJ bulk speed shear values below the jet are much broader than the distributions of shear values above the jet. These observations demonstrate that the speed shear is, in most cases, stronger below the LLJ than above it. This usually is because most LLJs are very low in altitude (below 150 m) and, therefore, the height difference $h_{\text{LLJ}} - h_{\text{min,below}}$ in Eq. (1) is usually smaller than the height difference $h_{\text{min,above}} - h_{\text{LLJ}}$ in Eq. (2).

The mean and median bulk speed shear above and below the LLJ are strongest in spring (median values are −0.022 m s^{-1} m^{-1} above and 0.057 m s^{-1} m^{-1} below) and weakest in winter (median values are −0.013 m s^{-1} m^{-1} above and 0.028 m s^{-1} m^{-1} below). Above the jet, the distribution of speed shear values is similar for all seasons, peaking between −0.01 and −0.02 m s^{-1} m^{-1}. In contrast, below the jet, in winter and autumn the distributions are more positively skewed than in spring and summer, denoting larger shear values during spring and

TABLE 1. LLJ statistics showing mean, 25th, 50th (median), and 75th percentiles of LLJ height, LLJ wind speed, and bulk speed shears above and below the LLJ on each season.

	Season	Mean	25th percentile	Median	75th percentile
LLJ height (m)	All	161	81	121	158
	Winter	254	130	243	327
	Spring	141	75	113	158
	Summer	140	73	104	130
	Autumn	206	109	130	271
LLJ wind speed ($m\,s^{-1}$)	All	11.6	8.7	10.8	13.7
	Winter	12.5	9.3	11.8	15.6
	Spring	12.2	8.9	11.4	14.8
	Summer	10.9	8.7	10.6	12.7
	Autumn	11.5	8.0	10.0	13.0
Speed shear above the LLJ ($s^{-1}\,m^{-1}$)	All	−0.024	−0.030	−0.019	−0.011
	Winter	−0.016	−0.019	−0.013	−0.009
	Spring	−0.028	−0.034	−0.022	−0.013
	Summer	−0.024	−0.030	−0.020	−0.012
	Autumn	−0.020	−0.024	−0.015	−0.008
Speed shear below the LLJ ($s^{-1}\,m^{-1}$)	All	0.054	0.031	0.048	0.071
	Winter	0.030	0.017	0.028	0.040
	Spring	0.063	0.040	0.057	0.082
	Summer	0.058	0.036	0.052	0.077
	Autumn	0.035	0.022	0.031	0.046

summer below the jet. Eight percent of bulk speed shear values are larger than $0.1\,m\,s^{-1}\,m^{-1}$, and 1% are smaller than $-0.1\,m\,s^{-1}\,m^{-1}$.

Figures 9a–d show how the LLJ height varies with speed and direction during each season. The highest and strongest LLJs typically arrive from southwesterly directions, which is also the prevailing wind direction at this site. These LLJs occur in all seasons. Other strong and high LLJs arrive from the east and from the north-northwest; these are present in spring and summer, with the easterly LLJs being slightly stronger and higher. LLJs at heights below 100 m have low wind speeds (typically $<15\,m\,s^{-1}$) and appear to be evenly distributed in all directions, except in winter.

c. *Threshold sensitivity in the LLJ identification algorithm*

In comparison with previous automated LLJ identification algorithms that were predominantly applied to observations with coarser temporal resolution by, for example, Bonner (1968), Whiteman et al. (1997), and Baas et al. (2009) and to gridded reanalysis data by, for example, Rife et al. (2010), Ranjha et al. (2013), and Tuononen et al. (2015), our newly developed algorithm includes some extra subjectively chosen thresholds and criteria. To ensure that the results presented here are not strongly threshold dependent, in this section we analyze the impact of all thresholds that were applied.

The sensitivity of the LLJ characteristics—that is, LLJ frequency of occurrence (Fig. 10a), LLJ mean height (Fig. 10b), LLJ mean speed (Fig. 10c), number of LLJ cases (Fig. 10d), and LLJ duration (Fig. 10e)—to the threshold values used in the LLJ identification algorithm was analyzed by changing one threshold value at a time while keeping the others constant (the default values are those described in section 3). Threshold values for the change in the height, speed, and direction between two consecutive low-level wind speed maxima (e.g., as described in Figs. 5a–c) were varied by ±10%, ±30%, ±50%, and ±70% relative to the default thresholds. Furthermore, the accepted time difference between two consecutive low-level wind speed maxima (as described in Fig. 5d) was also varied by ±10%, ±30%, ±50%, and ±70% relative to the default threshold. Last, the sensitivity to the duration criterion—that is, how long an LLJ case needs to be—was investigated by varying the default value by ±10%, ±30%, ±50%, and ±70%. Note that, except in the case of the duration threshold, when the threshold values are decreased the algorithm becomes stricter and when they are increased the algorithm becomes less stringent.

The LLJ frequency of occurrence is the most sensitive to the time-difference threshold between two consecutive low-level wind speed maxima (Fig. 10a). When the time-difference threshold is changed by −70% (equivalent to setting it to be less than 18 min), the LLJ frequency of occurrence decreases to 7%. Changes in the other thresholds do not affect the LLJ frequency of occurrence as much, especially when the algorithm is relaxed. By changing any threshold by ±30%, the LLJ

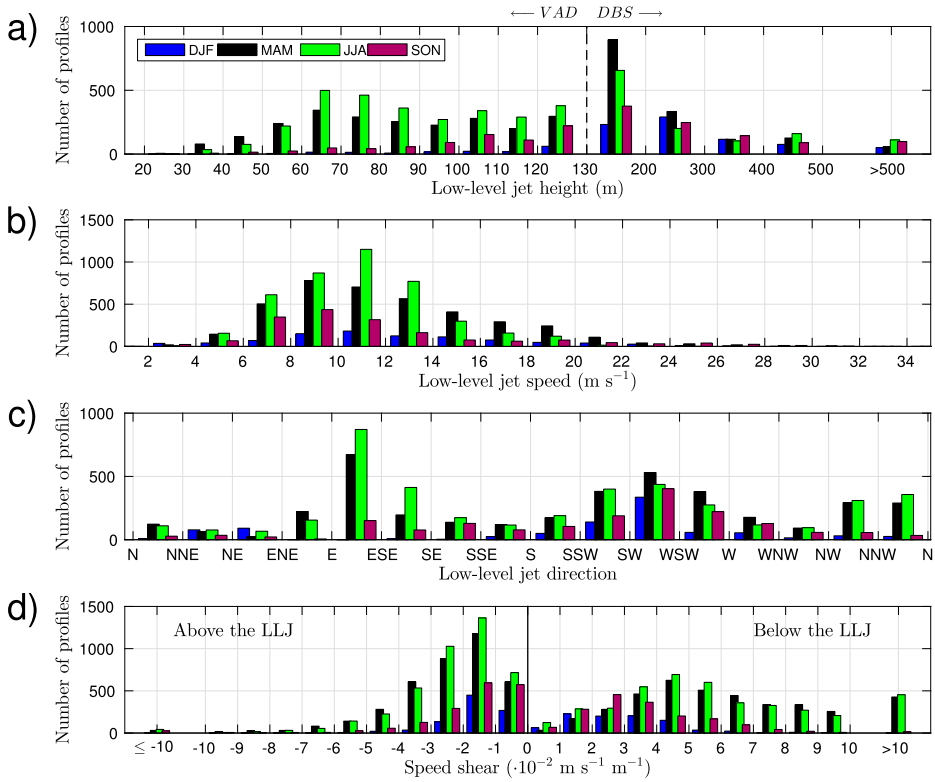

FIG. 8. Histograms that show (a) LLJ height (note the unequal bin edges on the x axis, corresponding to 4–5 gates in the VAD range and 3–4 gates in the DBS range, except the last bin), (b) LLJ speed, (c) LLJ direction, and (d) LLJ bulk speed shear (by definition: <0 above the LLJ and >0 below the LLJ). Each bar represents the number of profiles between the tick values. Results are separated by different seasons.

frequency of occurrence changes by less than ±1% relative to the LLJ frequency of occurrence as calculated with the default thresholds.

The LLJ mean height is affected most when the height-difference threshold or time-difference threshold between two consecutive low-level wind speed maxima is changed (Fig. 10b). The duration threshold also affects the mean LLJ height but in the opposite direction. This result is consistent with expectations, because the longer cases usually occur at lower heights. For any threshold change of ±30% or less, however, the LLJ mean height varies by less than 20 m, which is smaller than the vertical resolution of the data obtained from the DBS scans.

The impact on LLJ mean speed is marginal for any threshold variation up to ±70% (Fig. 10c), especially for any increase in threshold value. Even when the thresholds are decreased by 70%, the resulting LLJ mean speed varies by less than 0.6 m s^{-1}, and the extreme values are within ±1% relative to the reference mean LLJ speed.

The number of LLJ cases is mostly affected by changing the time threshold and the duration threshold (Fig. 10d), as expected. If the time gap between two low-level wind speed maxima is less than 18 min (70% decrease relative to the reference time-difference threshold), the number of LLJ cases clearly decreases. In contrast, by requiring the LLJ duration to be only 18 min, the number of LLJ cases clearly increases. Because the percentage change in the number of cases is much larger than for any other LLJ statistic, we conclude that, of all of the LLJ statistics that we consider, the number of LLJ cases is most susceptible to the subjective threshold choice and is the least reliable.

The LLJ duration is affected mostly when the duration threshold or the time threshold is changed. If the time threshold is reduced (allowing a shorter time gap between two consecutive low-level wind speed maxima), the algorithm splits LLJ cases more often into shorter cases. In contrast, allowing a longer time gap allows LLJ cases to continue across missing data.

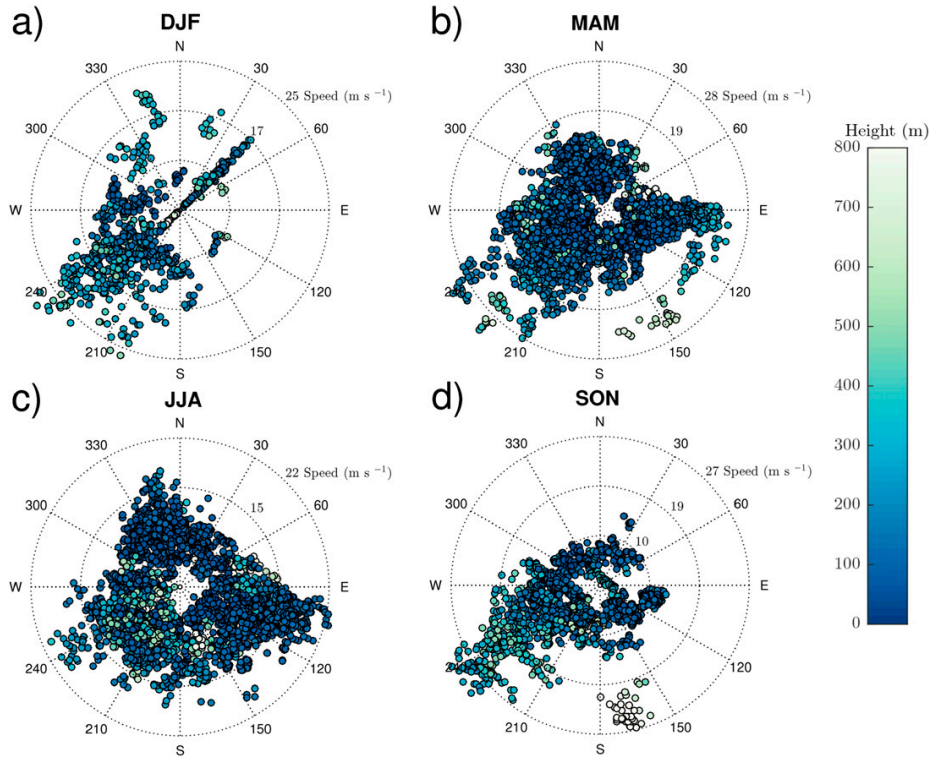

FIG. 9. Scatterplots that show how LLJ height varies with LLJ speed and direction for each season: (a) DJF, (b) MAM, (c) JJA, and (d) SON. LLJ speed and direction are presented in polar coordinates, and the color of the circle shows the LLJ height. Values for each individual LLJ profile within all observed LLJ cases are plotted. Note that each plot has a different scaling for the LLJ wind speed. LLJ direction is defined as the direction from which the wind is coming.

However, increasing the allowed time gap also permits the algorithm to combine cases that do not have the same characteristics and therefore should not be identified as the same case (not shown). Other thresholds have a minimal effect on the mean LLJ duration.

Overall, changing the duration threshold has the largest effect on the results, especially in the mean height, number of cases, and LLJ duration itself. If the LLJ duration threshold is increased, the mean LLJ height is lower, the number of LLJs is decreased, and the duration is longer relative to the reference. On the contrary, if shorter LLJs are allowed, the mean height is higher, the number of LLJs is larger, and the duration is shorter relative to the reference. The length of the allowed time gap between two consecutive low-level wind speed maxima also affects the results. Both of these thresholds are essential for the algorithm to operate because of the characteristics of the Doppler lidar data that are available at this location (described in section 3), and the reference values for these thresholds were selected on the basis of the time resolution and limitations of the data. Otherwise, the observed LLJ characteristics are not sensitive to the choice of threshold if it is within ±30% of the reference thresholds employed in this study.

5. Comparison with earlier studies in the Baltic Sea

We now compare the results presented here with previous studies that were conducted close to Utö. Quantitative comparison is often difficult because of the differences in the measurement period, LLJ identification criteria, instrument capabilities, and data resolution.

Dörenkämper et al. (2015) investigated the seasonal variation of LLJ occurrence and LLJ characteristics in the western Baltic Sea (55.00°N, 13.15°E) on the basis of 6 years of mast measurements up to 102 m MSL. They define an LLJ event such that the wind speed at any altitude below 102 m must exceed the wind speed measured at 102 m by a certain percentage value

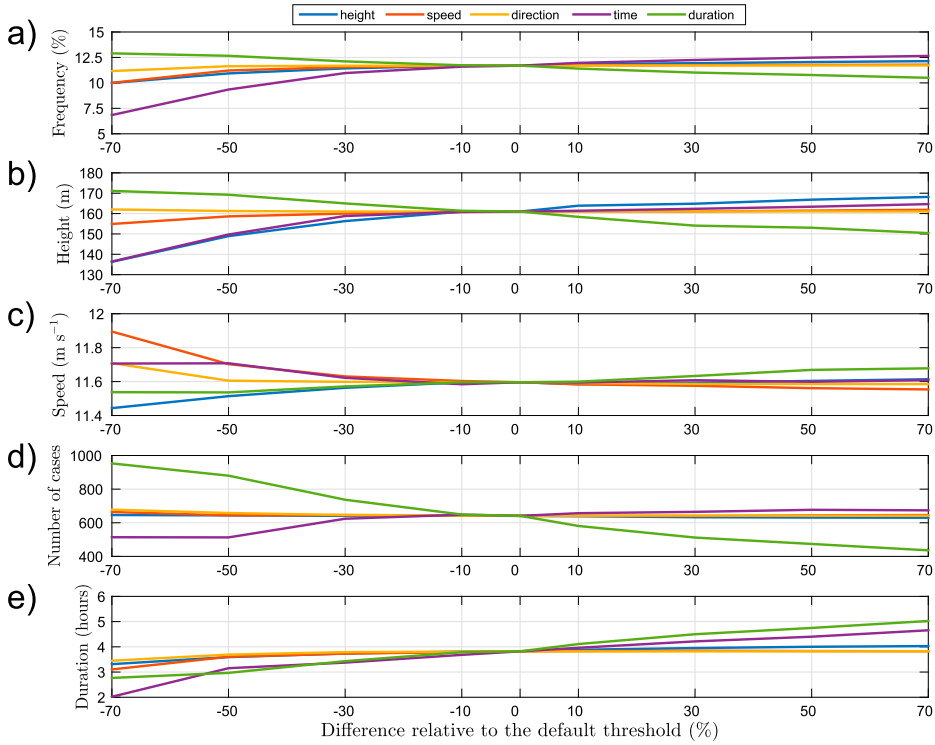

FIG. 10. Sensitivity of (a) LLJ frequency of occurrence, (b) mean LLJ height, (c) mean LLJ speed, (d) number of LLJ cases, and (e) mean LLJ duration to the different thresholds that are used in the LLJ identification algorithm described in section 3 and shown in Fig. 5. The corresponding lines and thresholds are given by blue for the height threshold, orange for the speed threshold, yellow for the direction threshold, purple for the time threshold, and green for the duration threshold.

(10%, 20%, 30%, or 40%). Dörenkämper et al. (2015) found the highest LLJ occurrence in spring (7% with the least-strict criteria) and the lowest occurrence in winter (<1% with the least-strict criteria). They found no strong diurnal cycle for springtime LLJs but slightly enhanced LLJ occurrence in summer evenings. Our results show enhanced LLJ occurrence throughout the night in summer, whereas in autumn increased LLJ frequency of occurrence is found in the evening. Our results show higher LLJ frequency of occurrences, and, in contrast to the study by Dörenkämper et al. (2015), the highest LLJ frequency of occurrence is found in summer (21%) and the second highest is found in spring (18%). Differences between the results may be due to the different vertical extent of the two different measurement systems (meteorological mast vs Doppler lidar) and consequently the different definitions of an LLJ. Although both sites were located in the Baltic Sea, the different site characteristics may also play a role.

To enable a fairer comparison with the results of Dörenkämper et al. (2015), our statistics were recalculated by limiting the results to LLJ maxima identified below 102 m MSL. The observed diurnal cycle of LLJ occurrence in these recalculated statistics is similar to that found by Dörenkämper et al. (2015) both in spring and summer (not shown). In addition, the LLJ frequency of occurrence at Utö decreases to 10% in summer and 7% in spring and similarly is low in winter (0.2%) and autumn (1.2%). These recalculated statistics compare better to the study by Dörenkämper et al. (2015); note, however, that, although we consider only LLJs below 102 m, the minimum above the jet is usually found above 102 m.

Högström and Smedman-Högström (1984), and Smedman et al. (1993, 1995) investigated LLJs in the Baltic coast of Sweden and the Stockholm archipelago on the basis of double-theodolite pilot-balloon measurements, radiosoundings, aircraft measurements, and modeling. They found spring- and summertime LLJs

that were forced by an inertial oscillation in space in situations in which the flow is directed from a warmer coast (Swedish or Latvian coast) over the colder Baltic Sea. According to Smedman et al. (1995), summertime LLJs—observed by the radiosonde observations and modeled by the numerical simulations in the Stockholm archipelago, and forced by an inertial oscillation in space—occur at low altitudes (30–100 m) and reach speeds of 12 m s^{-1}. In addition, on the basis of idealized 2D-modeling experiments, Savijärvi (2011) found summertime LLJs along the southern coast of Finland that were due to inertial oscillations in space when the flow was directed from the Estonian coast over the colder sea. Furthermore, the model results by Savijärvi (2011) revealed easterly LLJs with height and speed characteristics that were similar to those reported here in Doppler lidar data from Utö.

It is also interesting to compare our observations with results that were obtained from a reanalysis dataset. Wintertime (October–March) LLJs were diagnosed from the "Arctic system reanalysis" (ASR) for the period of 2000–10 by Tuononen et al. (2015). They found that the wintertime LLJ frequency of occurrence at the grid point nearest to Utö was 18%, with an LLJ mean height of 340 m and an LLJ mean wind speed of 11 m s^{-1}. These LLJs were higher and weaker than those observed with the Doppler lidar, probably as a result of both the coarser vertical resolution close to the ground in ASR and the reduction in data availability at higher altitudes in the observations. This would also explain why there are more LLJs diagnosed in ASR than in the observations. The predominant LLJ direction in ASR was from the west, with the majority occurring within the west-to-south sectors; our observations show southwest as the predominant LLJ direction. Although progress has been made in representing LLJs in high-resolution numerical models (e.g., Hu et al. 2013; Vanderwende et al. 2015), this comparison suggests that deficiencies are still evident in coarser-vertical-resolution reanalysis datasets, especially when attempting to diagnose LLJs below 100 m.

6. Optimizing scanning for LLJs

It is clear that the scanning scheme employed at this location is not optimal for diagnosing LLJs, especially because it necessitates combining two scan types with very different data availabilities at the height at which they are stacked (130 m). Although LLJs are not expected in strong convectively driven turbulent conditions, such conditions do affect the wind retrievals, with DBS scans suffering strongly from violation of the homogeneity assumption necessary for the retrieval. VAD scans mitigate this impact, but VADs are also susceptible to turbulence causing the homogeneity assumption to be violated, especially at higher scan elevations (Päschke et al. 2015). Therefore, an ideal scan strategy would involve the use of one VAD scan at an elevation that gives full coverage through the extent of the boundary layer (i.e., up to at least 1.5 km in altitude) while still providing sufficient vertical resolution near the surface to enable the calculation of both the LLJ maximum and the minimum below for LLJs below 100 m. A suitable elevation angle for the scan will depend on the range resolution of the instrument that is performing the scans. An instrument with a radial range resolution of 100 m must scan lower than an instrument with a radial range resolution of 30 m to obtain the same vertical resolution; an elevation angle of 9° for a range resolution of 100 m and 30° for a range resolution of 30 m will permit a vertical resolution of 15 m.

Our results indicate that the temporal resolution of the scans (10 min for DBS; 30 min for VAD) was sufficient for capturing LLJs so that when selecting an integration time the focus should be on obtaining high-quality data rather than rapid scans (i.e., taking 4 min to complete one high-quality VAD scan may be preferable to a sequence of 10 scans taking 24 s each). The integration time will depend on location since it depends on the amount of aerosol that is present in the atmosphere.

7. Conclusions

An LLJ identification algorithm was developed specifically for objective identification of LLJs in Doppler lidar data with high temporal and vertical resolution. The algorithm was applied to more than 2 years of Doppler lidar data from Utö, an island in the Finnish outer archipelago, to determine the LLJ frequency of occurrence, the statistics of LLJ characteristics, and their seasonal and diurnal variability. In the future, this algorithm can easily be applied to data from different locations and even in an operational context. In this study, the wind profiles, used as input to the LLJ identification algorithm, are obtained by combining observations from two different Doppler lidar scanning patterns (DBS and VAD) with additional anemometer wind data. In addition, a data-quality step was applied, removing measurements for which the homogeneity assumption was unlikely to be satisfied because of the presence of convectively driven turbulence.

LLJs were identified in 12% of all observed wind profiles at Utö. The vast majority of LLJs were identified below 150 m AGL, and the mean LLJ wind speed was 11.6 m s^{-1}. The LLJ frequency of occurrence should be considered as a lower limit because of data limitations.

For example, some LLJs may be missed because of data gaps that can occur during cloudy conditions or when the air is very clean—a more common problem in Utö than in most European locations—because the lidar signal is too weak. Low data availability at higher altitudes as a result of the lack of signal limits any detection of potential LLJs at these altitudes, directly affecting our results. The data availability below 400 m AGL, however, was sufficient to capture LLJs that can have an impact on wind energy, which was one motivation of this study.

The LLJ frequency of occurrence was higher during spring and summer (up to 30% during summer nights) than in autumn and was lowest in winter (<5% throughout the day). During summer, LLJs occur at lower heights and are slightly weaker than they are in other seasons. The highest and strongest LLJs come from the southwest, which is also the predominant LLJ direction in all seasons. Other common directions in spring and summer are east and north-northwest, which exhibit lower and slightly weaker LLJs. LLJs below 100 m are the weakest, show little directional dependence, and are most common in spring and summer.

We have shown that LLJ is a common phenomenon and occurs at relatively low altitudes at Utö, especially during the spring and summer seasons. Since LLJs can have a positive impact on the production of wind power and a potential negative impact on the lifetime and efficiency of wind turbines (Kelley et al. 2006), the ability to provide long-term climatological descriptions of LLJ characteristics is crucial when considering future increases in offshore wind-turbine installations in the Finnish archipelago. Numerical models are used to provide wind-resource assessments for wind-energy purposes, and these observations will be used to evaluate whether such models are capable of producing LLJs accurately in this region. In addition, the characteristics of the shear-driven turbulence associated with LLJs, which were not included in this study, should be examined in detail to understand their impact on wind-turbine stress and wind-power production. The objective algorithm created for this study can be used to identify LLJs operationally, verify numerical model output, and guide decision-making regarding wind-power installations in the future.

Acknowledgments. Author MT was supported by the Maj and Tor Nessling Foundation (Grants 201500300 and 201600003). Author VAS was funded by the Academy of Finland (Project 3073314). We also acknowledge the support from EU COST Action ES1303 TOPROF.

REFERENCES

Andreas, E. L, K. J. Claffy, and A. P. Makshtas, 2000: Low-level atmospheric jets and inversions over the western Weddell Sea. *Bound.-Layer Meteor.*, **97**, 459–486, doi:10.1023/A:1002793831076.

Baas, P., F. C. Bosveld, H. K. Baltink, and A. A. M. Holtslag, 2009: A climatology of nocturnal low-level jets at Cabauw. *J. Appl. Meteor. Climatol.*, **48**, 1627–1642, doi:10.1175/2009JAMC1965.1.

——, B. J. H. van de Wiel, L. van den Brink, and A. Holtslag, 2012: Composite hodographs and inertial oscillations in the nocturnal boundary layer. *Quart. J. Roy. Meteor. Soc.*, **138**, 528–535, doi:10.1002/qj.941.

Banta, R. M., R. K. Newsom, J. K. Lundquist, Y. L. Pichugina, R. L. Coulter, and L. Mahrt, 2002: Nocturnal low-level jet characteristics over Kansas during CASES-99. *Bound.-Layer Meteor.*, **105**, 221–252, doi:10.1023/A:1019992330866.

——, Y. L. Pichugina, and W. A. Brewer, 2006: Turbulent velocity-variance profiles in the stable boundary layer generated by a nocturnal low-level jet. *J. Atmos. Sci.*, **63**, 2700–2719, doi:10.1175/JAS3776.1.

——, ——, N. D. Kelley, R. M. Hardesty, and W. A. Brewer, 2013: Wind energy meteorology: Insight into wind properties in the turbine-rotor layer of the atmosphere from high-resolution Doppler lidar. *Bull. Amer. Meteor. Soc.*, **94**, 883–902, doi:10.1175/BAMS-D-11-00057.1.

Blackadar, A. K., 1957: Boundary layer wind maxima and their significance for the growth of nocturnal inversions. *Bull. Amer. Meteor. Soc.*, **38**, 283–290.

Bonner, W. D., 1968: Climatology of the low level jet. *Mon. Wea. Rev.*, **96**, 833–850, doi:10.1175/1520-0493(1968)096<0833:COTLLJ>2.0.CO;2.

Dörenkämper, M., M. Optis, A. Monahan, and G. Steinfeld, 2015: On the offshore advection of boundary-layer structures and the influence on offshore wind conditions. *Bound.-Layer Meteor.*, **155**, 459–482, doi:10.1007/s10546-015-0008-x.

Floors, R., C. L. Vincent, S. E. Gryning, A. Peña, and E. Batchvarova, 2013: The wind profile in the coastal boundary layer: Wind lidar measurements and numerical modelling. *Bound.-Layer Meteor.*, **147**, 469–491, doi:10.1007/s10546-012-9791-9.

Henderson, S. W., P. Gatt, D. Rees, and R. M. Huffaker, 2005: Wind lidar. *Laser Remote Sensing*, T. Fujii and T. Fukuchi, Eds., CRC Press, 469–722.

Higgins, R. W., Y. Yao, E. S. Yarosh, J. E. Janowiak, and K. C. Mo, 1997: Influence of the Great Plains low-level jet on summertime precipitation and moisture transport over the central United States. *J. Climate*, **10**, 481–507, doi:10.1175/1520-0442(1997)010<0481:IOTGPL>2.0.CO;2.

Hirsikko, A., and Coauthors, 2014: Observing wind, aerosol particles, cloud and precipitation: Finland's new ground-based remote-sensing network. *Atmos. Meas. Tech.*, **7**, 1351–1375, doi:10.5194/amt-7-1351-2014.

Hogan, R. J., A. L. M. Grant, A. J. Illingworth, G. N. Pearson, and E. J. O'Connor, 2009: Vertical velocity variance and skewness in clear and cloud-topped boundary layers as revealed by Doppler lidar. *Quart. J. Roy. Meteor. Soc.*, **135**, 635–643, doi:10.1002/qj.413.

Högström, U., and A.-S. Smedman-Högström, 1984: The wind regime in coastal areas with special reference to results obtained from the Swedish wind energy program. *Bound.-Layer Meteor.*, **30**, 351–373, doi:10.1007/BF00121961.

Hu, X.-M., P. M. Klein, M. Xue, F. Zhang, D. C. Doughty, R. Forkel, E. Joseph, and J. D. Fuentes, 2013: Impact of the vertical mixing induced by low-level jets on boundary layer ozone concentration. *Atmos. Environ.*, **70**, 123–130, doi:10.1016/j.atmosenv.2012.12.046.

Kallistratova, M. A., and R. D. Kouznetsov, 2012: Low-level jets in the Moscow region in summer and winter observed with a sodar network. *Bound.-Layer Meteor.*, **143**, 159–175, doi:10.1007/s10546-011-9639-8.

Karipot, A., M. Y. Leclerc, and G. Zhang, 2009: Characteristics of nocturnal low-level jets observed in the north Florida area. *Mon. Wea. Rev.*, **137**, 2605–2621, doi:10.1175/2009MWR2705.1.

Kelley, N. D., B. J. Jonkman, and G. N. Scott, 2006: The Great Plains turbulence environment: Its origins, impact and simulation. National Renewable Energy Laboratory Conf. Paper NREL/CP-500-40176, 21 pp, https://www.nrel.gov/docs/fy07osti/40176.pdf.

Koscielny, A. J., R. J. Doviak, and D. S. Zrnic, 1984: An evaluation of the accuracy of some radar wind profiling techniques. *J. Atmos. Oceanic Technol.*, **1**, 309–320, doi:10.1175/1520-0426(1984)001<0309:AEOTAO>2.0.CO;2.

Kotroni, V., and K. Lagouvardos, 1993: Low-level jet streams associated with atmospheric cold fronts: Seven case studies from the Fronts 87 Experiment. *Geophys. Res. Lett.*, **20**, 1371–1374, doi:10.1029/93GL01701.

Lane, S. E., J. F. Barlow, and C. R. Wood, 2013: An assessment of a three-beam Doppler lidar wind profiling method for use in urban areas. *J. Wind Eng. Ind. Aerodyn.*, **119**, 53–59, doi:10.1016/j.jweia.2013.05.010.

Manninen, A. J., E. J. O'Connor, V. Vakkari, and T. Petäjä, 2016: A generalised background correction algorithm for a Halo Doppler lidar and its application to data from Finland. *Atmos. Meas. Tech.*, **9**, 817–827, doi:10.5194/amt-9-817-2016.

Mao, H., and R. Talbot, 2004: Role of meteorological processes in two New England ozone episodes during summer 2001. *J. Geophys. Res.*, **109**, D20305, doi:10.1029/2004JD004850.

May, P. T., 1995: The Australian nocturnal jet and diurnal variations of boundary-layer winds over Mt. Isa in north-eastern Australia. *Quart. J. Roy. Meteor. Soc.*, **121**, 987–1003, doi:10.1002/qj.49712152503.

Mitchell, M. J., R. W. Arritt, and K. Labas, 1995: A climatology of the warm season Great Plains low-level jet using wind profiler observations. *Wea. Forecasting*, **10**, 576–591, doi:10.1175/1520-0434(1995)010<0576:ACOTWS>2.0.CO;2.

O'Connor, E. J., A. J. Illingworth, I. M. Brooks, C. D. Westbrook, R. J. Hogan, F. Davies, and B. J. Brooks, 2010: A method for estimating the turbulent kinetic energy dissipation rate from a vertically pointing Doppler lidar, and independent evaluation from balloon-borne in-situ measurements. *J. Atmos. Oceanic Technol.*, **27**, 1652–1664, doi:10.1175/2010JTECHA1455.1.

Orr, A., J. Hunt, R. Capon, J. Sommeria, D. Cresswell, and A. Owinoh, 2005: Coriolis effects on wind jets and cloudiness along coasts. *Weather*, **60**, 291–299, doi:10.1256/wea.219.04.

Owinoh, A. Z., J. C. R. Hunt, A. Orr, P. Clark, R. Klein, H. J. S. Fernando, and F. T. N. Nieuwstadt, 2005: Effects of changing surface heat fluxes on the atmospheric boundary layer flow over flat terrain. *Bound.-Layer Meteor.*, **116**, 331–361, doi:10.1007/s10546-004-2819-z.

Parish, T. R., 1982: Barrier winds along the Sierra Nevada Mountains. *J. Appl. Meteor.*, **21**, 925–930, doi:10.1175/1520-0450(1982)021<0925:BWATSN>2.0.CO;2.

——, 2000: Forcing of the summertime low-level jet along the California coast. *J. Appl. Meteor.*, **39**, 2421–2433, doi:10.1175/1520-0450(2000)039<2421:FOTSLL>2.0.CO;2.

Päschke, E., R. Leinweber, and V. Lehmann, 2015: An assessment of the performance of a 1.5 μm Doppler lidar for operational vertical wind profiling based on a 1-year trial. *Atmos. Meas. Tech.*, **8**, 2251–2266, doi:10.5194/amt-8-2251-2015.

Peña, A., and Coauthors, 2016: Ten years of boundary-layer and wind-power meteorology at Høvsøre, Denmark. *Bound.-Layer Meteor.*, **158**, 1–26, doi:10.1007/s10546-015-0079-8.

Pichugina, Y. L., R. M. Banta, W. A. Brewer, S. P. Sandberg, and R. M. Hardesty, 2012: Doppler lidar–based wind-profile measurement system for offshore wind-energy and other marine boundary layer applications. *J. Appl. Meteor. Climatol.*, **51**, 327–349, doi:10.1175/JAMC-D-11-040.1.

Pirinen, P., H. Simola, J. Aalto, J.-P. Kaukoranta, P. Karllson, and R. Ruuhela, 2012: Climatological statistics of Finland 1981–2010. Finnish Meteorological Institute Rep. 2012:1, 92 pp.

Ranjha, R., G. Svensson, M. Tjernström, and A. Semedo, 2013: Global distribution and seasonal variability of coastal low-level jets derived from ERA-Interim reanalysis. *Tellus*, **65A**, doi:10.3402/tellusa.v65i0.20412.

Renfrew, I. A., and P. S. Anderson, 2006: Profiles of katabatic flow in summer and winter over Coats Land, Antarctica. *Quart. J. Roy. Meteor. Soc.*, **132**, 779–802, doi:10.1256/qj.05.148.

Rife, D. L., J. O. Pinto, A. J. Monaghan, C. A. Davis, and J. R. Hannan, 2010: Global distribution and characteristics of diurnally varying low-level jets. *J. Climate*, **23**, 5041–5064, doi:10.1175/2010JCLI3514.1.

Rye, B. J., and R. M. Hardesty, 1993: Discrete spectral peak estimation in incoherent backscatter heterodyne lidar. I: Spectral accumulation and the Cramer–Rao lower bound. *IEEE Trans. Geosci. Remote Sens.*, **31**, 16–27, doi:10.1109/36.210440.

Savijärvi, H. I., 2011: Anti-heat island circulations and low-level jets on a sea gulf. *Tellus*, **63A**, 1007–1013, doi:10.1111/j.1600-0870.2011.00531.x.

Smedman, A.-S., M. Tjernström, and U. Högström, 1993: Analysis of the turbulence structure of a marine low-level jet. *Bound.-Layer Meteor.*, **66**, 105–126, doi:10.1007/BF00705462.

——, H. Bergström, and U. Högström, 1995: Spectra, variances and length scales in a marine stable boundary layer dominated by a low level jet. *Bound.-Layer Meteor.*, **76**, 211–232, doi:10.1007/BF00709352.

Song, J., K. Liao, R. L. Coulter, and B. M. Lesht, 2005: Climatology of the low-level jet at the southern Great Plains Atmospheric Boundary Layer Experiments site. *J. Appl. Meteor.*, **44**, 1593–1606, doi:10.1175/JAM2294.1.

Stensrud, D. J., 1996: Importance of low-level jets to climate: A review. *J. Climate*, **9**, 1698–1711, doi:10.1175/1520-0442(1996)009<1698:IOLLJT>2.0.CO;2.

Storm, B., and S. Basu, 2010: The WRF Model forecast-derived low-level wind shear climatology over the United States Great Plains. *Energies*, **3**, 258–276, doi:10.3390/en3020258.

——, J. Dudhia, S. Basu, A. Swift, and I. Giammanco, 2009: Evaluation of the Weather Research and Forecasting Model on forecasting low-level jets: Implications for wind energy. *Wind Energy*, **12**, 81–90, doi:10.1002/we.288.

Su, J., M. Felton, L. Lei, M. P. McCormick, R. Delgado, and A. St. Pé, 2016: Lidar remote sensing of cloud formation caused by low-level jets. *J. Geophys. Res. Atmos.*, **121**, 5904–5911, doi:10.1002/2015JD024590.

Svensson, N., H. Bergström, E. Sahlée, and A. Rutgersson, 2016: Stable atmospheric conditions over the Baltic Sea: Model evaluation and climatology. *Boreal Environ. Res.*, **21**, 387–404.

Tucker, S. C., C. J. Senff, A. M. Weickmann, W. A. Brewer, R. M. Banta, S. P. Sandberg, D. C. Law, and R. M. Hardesty, 2009: Doppler lidar estimation of mixing height using turbulence, shear, and aerosol profiles. *J. Atmos. Oceanic Technol.*, **26**, 673–688, doi:10.1175/2008JTECHA1157.1.

——, and Coauthors, 2010: Relationships of coastal nocturnal boundary layer winds and turbulence to Houston ozone concentrations during TexAQS 2006. *J. Geophys. Res.*, **115**, D10304, doi:10.1029/2009JD013169.

Tuononen, M., V. A. Sinclair, and T. Vihma, 2015: A climatology of low-level jets in the mid-latitudes and polar regions of the Northern Hemisphere. *Atmos. Sci. Lett.*, **16**, 492–499, doi:10.1002/asl.587.

USGS, 2010: Global multi-resolution terrain elevation data. U.S. Geological Survey, accessed 4 March 2015, http://earthexplorer.usgs.gov/.

Vanderwende, B. J., J. K. Lundquist, M. E. Rhodes, E. S. Takle, and S. L. Irvin, 2015: Observing and simulating the summertime low-level jet in central Iowa. *Mon. Wea. Rev.*, **143**, 2319–2336, doi:10.1175/MWR-D-14-00325.1.

Whiteman, C. D., X. Bian, and S. Zhong, 1997: Low-level jet climatology from enhanced rawinsonde observations at a site in the Southern Great Plains. *J. Appl. Meteor.*, **36**, 1363–1376, doi:10.1175/1520-0450(1997)036<1363:LLJCFE>2.0.CO;2.

III

Reprinted, with permission, from
Journal of Applied Meteorology and Climatology, 57, 1155–1170,
doi:10.1175/JAMC-D-17-0341.1

Long-Term Observations and High-Resolution Modeling of Midlatitude Nocturnal Boundary Layer Processes Connected to Low-Level Jets

TOBIAS MARKE, SUSANNE CREWELL, VERA SCHEMANN, AND JAN H. SCHWEEN

Institute for Geophysics and Meteorology, University of Cologne, Cologne, Germany

MINTTU TUONONEN

Finnish Meteorological Institute, Helsinki, and Vaisala Oyj, Vantaa, and Department of Physics, University of Helsinki, Helsinki, Finland

(Manuscript received 6 December 2017, in final form 9 March 2018)

ABSTRACT

Low-level-jet (LLJ) periods are investigated by exploiting a long-term record of ground-based remote sensing Doppler wind lidar measurements supported by tower observations and surface flux measurements at the Jülich Observatory for Cloud Evolution (JOYCE), a midlatitude site in western Germany. LLJs were found 13% of the time during continuous observations over more than 4 yr. The climatological behavior of the LLJs shows a prevailing nighttime appearance of the jets, with a median height of 375 m and a median wind speed of 8.8 m s^{-1} at the jet nose. Significant turbulence below the jet nose only occurs for high bulk wind shear, which is an important parameter for describing the turbulent characteristics of the jets. The numerous LLJs (16% of all jets) in the range of wind-turbine rotor heights below 200 m demonstrate the importance of LLJs and the associated intermittent turbulence for wind-energy applications. Also, a decrease in surface fluxes and an accumulation of carbon dioxide are observed if LLJs are present. A comprehensive analysis of an LLJ case shows the influence of the surrounding topography, dominated by an open pit mine and a 200-m-high hill, on the wind observed at JOYCE. High-resolution large-eddy simulations that complement the observations show that the spatial distribution of the wind field exhibits variations connected with the orographic flow depending on the wind direction, causing high variability in the long-term measurements of the vertical velocity.

1. Introduction

One of the dominant nocturnal atmospheric boundary layer processes over land areas is the decoupling of the lower troposphere from the friction-governed surface layer, leading to the formation of a distinct maximum in the vertical profile of the horizontal wind speed, called a low-level jet (LLJ). The nighttime development of a stable surface layer results in a decrease in surface friction in the decoupled residual layer above and hence an inertial oscillation (Blackadar 1957). The wind speed maximum of LLJs is typically found between 100 and 1000 m (Tuononen et al. 2015), and the wind shear below this jet maximum leads to the generation of turbulence (Banta et al. 2002). Turbulent motions related to the LLJs are often intermittent and highly energetic, which is crucial for wind-energy applications (Emeis et al. 2007; Peña et al. 2016). Especially in the region of the rotor height, LLJ events can have an impact on the performance and lifetime of a wind turbine (Zhou and Chow 2012). On the other hand, the increased wind speed makes places with frequently occurring LLJs, such as the Great Plains region, favorable for wind-energy production (Storm et al. 2009).

LLJs can also be associated with local transport of aerosols and water vapor, controlling the evolution of clouds and precipitation by horizontal convergence and uplifting of atmospheric constituents (Su et al. 2016). The transferring motions and moisture transport between the surface and the atmosphere also directly affect synoptic-scale systems, leading to changes in precipitation patterns (Higgins et al. 1997). At the surface, the momentum decoupling during nighttime LLJs can reduce surface fluxes, leading to an accumulation of atmospheric gases (Mathieu et al. 2005). This process is limited by intermittent turbulence that reaches the surface and hence weakens the stabilization and depth of

Corresponding author: Tobias Marke, tmarke@meteo.uni-koeln.de

DOI: 10.1175/JAMC-D-17-0341.1

the nocturnal boundary layer. The correct representation of LLJ-related turbulence effects is therefore crucial for predictions in atmospheric weather and climate models at different resolutions (Stensrud 1996; Holtslag et al. 2013).

The forcing mechanisms of continental LLJs in the midlatitudes have been extensively studied, especially in the Great Plains (Mitchell et al. 1995; Zhong et al. 1996), and a more complete review can be found in Stensrud (1996). The identification of LLJs in earlier studies was based on radiosonde observations (Bonner 1968; Whiteman et al. 1997) or meteorological-tower measurements (Dörenkämper et al. 2015). Even though these observations provide good vertical resolution, they are lacking in temporal resolution (radiosondes) and vertical extent (towers). Therefore, many previous studies have utilized remotely sensing radio acoustic or (ultra–high frequency) radar wind profilers to obtain detailed case analyses and continuous long-term records of LLJs (e.g., Baas et al. 2009; Lampert et al. 2016; Mitchell et al. 1995). Doppler wind lidars (DWLs), which are an emerging tool in ground-based remote sensing networks such as the European Earth System Science and Environmental Management European Cooperation in Science and Technology (COST) Action ES1303 network or the ground-based remote sensing network in Finland (Hirsikko et al. 2014), show considerable potential for observing winds and turbulent parameters at high spatial and temporal resolution. The study by Tuononen et al. (2017) showed the capability of a DWL to identify LLJs for a multiyear dataset, and Lampert et al. (2015) used a 1-yr dataset to derive statistics related to LLJ occurrence and parameters of the Weibull distribution. By continuously providing accurate estimates of the vertical wind component, DWLs are furthermore able to quantify turbulent motions (O'Connor et al. 2010) and detect clouds and the aerosol layer.

In this study, long-term (2012–16) DWL measurements at the Jülich Observatory for Cloud Evolution (JOYCE; Löhnert et al. 2015) in western Germany are used together with a detailed case analysis, combining ground-based remote sensing, radiosondes (RS), and large-eddy simulation (LES) model output, to investigate local nocturnal boundary layer processes. The research focus of this study encompasses the climatological behavior (or "climatology") of LLJs, their turbulence characteristics, and their influence on the surface fluxes using a long-term record of DWL, tower, and eddy-covariance (EC) measurements. A detailed case analysis reveals the local LLJ effects related to the topography by observations and LES. The chosen case analysis was carried out during the High Definition Cloud and Precipitation for Advancing Climate Prediction [HD(CP)^2] Observational Prototype Experiment (HOPE) field campaign in April and May of 2013 (Macke et al. 2017). The HOPE campaign was conducted to provide ground-based information on land surface–atmosphere interactions including clouds and precipitation in the boundary layer and to evaluate the LES extension of the atmospheric Icosahedral Nonhydrostatic (ICON) model (Dipankar et al. 2015).

This article is built in the following way. Section 2 describes the measurement site, including the deployed instruments utilized in this study. Subsequently in section 3 the dataset of the DWL is introduced together with the LLJ identification and the model setup. The results of the LLJ climatology, the turbulence characteristics, and the surface fluxes are presented and discussed in section 4, followed by the case analysis during the HOPE campaign that investigates topographic effects supported by LES in section 5. A summary is given and conclusions about the presented results are drawn in section 6.

2. Description of measurement site and instruments

a. JOYCE site and supporting instruments

The observational data are provided by the JOYCE site located in western Germany (50°54′31″N, 6°24′49″E at 111 m MSL; Fig. 1a), which is operated jointly by the Institute for Geophysics and Meteorology at the University of Cologne, the Meteorological Institute of the University of Bonn, and the Institute of Energy and Climate Research (IEK-8) at the Forschungszentrum Jülich. The JOYCE supersite is embedded in a rural environment with different crop types and provides a constantly growing multiyear dataset for detailed insight into boundary layer processes and patterns related to surface conditions (Löhnert et al. 2015). The mostly flat topography is dominated by two open-pit mines east and southwest of the site and a mine dump hill (Sophienhöhe), 200 m higher than the JOYCE site, to the northeast (Fig. 1c). A plain at around 100 m MSL stretches from southeast to northwest, including a riverbed of the Rur River and with a slight slope to the northwest. Together with the Eifel region, which is approximately 20 km to the south with hills of around 800 m MSL (Fig. 1b), the valley shows a potential channeling effect of the wind, with the Sophienhöhe as a northeast border. In a circle of 1 km around the JOYCE site, the topography shows a maximum height of 120.3 m MSL and a standard deviation of 5.7 m. The maximum height increases to 296.6 m MSL with a standard deviation of 48.9 m for a 5-km circle.

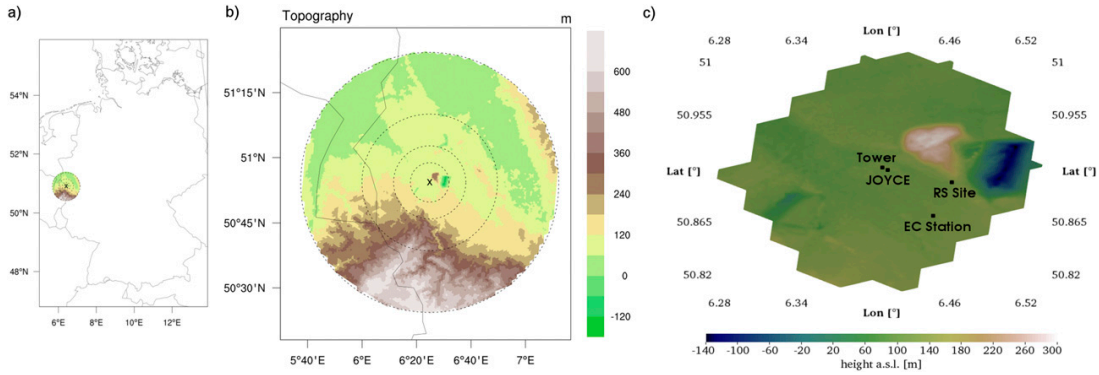

FIG. 1. (a) Location and (b) topographic maps of the ICON-LEM circular domains and the position of the JOYCE site (black X) within Germany. (c) A segment of the innermost domain (10-km radius and 78-m horizontal resolution) centered around the JOYCE site, also indicating the measurement sites and instruments deployed in this study.

The majority of the JOYCE instrumentation has been operational since 2012 and includes a DWL, cloud radar, microwave radiometer, and ceilometer. The long-term and continuous dataset of JOYCE provides temporal highly resolved cloud micro- and macrophysical observations, as well as a characterization of the environment in which they evolve. As an additional observational support during the HOPE campaign, from two to seven radiosonde launches per day were conducted from a nearby station. The launch site of the radiosondes (labeled as ''RS Site'' in Fig. 1) is located 3.8 km east of the site at the southeastern corner of the Sophienhöhe.

A 120-m-high meteorological tower is located approximately 330 m northwest of JOYCE (labeled as ''Tower'' in Fig. 1). The tower is equipped with cup anemometers and wind vanes at 30, 50, and 120 m, allowing simultaneous measurement of the wind speed and the wind direction. To observe the atmosphere–land surface interactions, several EC stations are deployed around JOYCE. For this study, the EC station at the agricultural flatland site Selhausen is used, which is located 5 km southeast of the JOYCE site (labeled as ''EC Station'' in Fig. 1). The measurement devices (sonic anemometer and open-path gas analyzer) are deployed at a height of 2.46 m above the ground. The averaging interval of the data obtained with a measurement frequency of 20 Hz is set to 30 min, and the quality assessment and quality control of the measurements, together with the instrument setup, are explained in Mauder et al. (2013).

b. *Doppler wind lidar*

The Halo Photonics Streamline DWL (Pearson et al. 2009), the main instrument for this study, was installed on the roof of the IEK-8 building, which is referred to as the JOYCE site. The DWL measures the backscattered light from an emitted laser beam at 1.5 μm. The analysis of the Doppler shift provides an estimate of the wind speed along the line of sight. The combination of several inclined beams allows the derivation of the three components of the wind vector and therefore also the wind direction. The attenuated backscatter coefficient can be calculated by the amount of received backscattered light, which mainly depends on the number and size of aerosol and/or cloud particles in the measured volume.

At JOYCE the DWL operational schedule consists of four conical scans per hour with 36 beams at 75° elevation and a duration of approximately 3 min. This velocity azimuth display method provides accurate wind estimates, even in turbulent situations (Päschke et al. 2015). For the remainder of the hour, the instrument points vertically, with a temporal resolution of 1.67 s. The vertical measurements provide profiles of the vertical velocity, which in turn can be used for turbulence estimates by calculating the standard deviation for each range gate (Schween et al. 2014). The vertical resolution is 30 m, with the first reliable range gate, as determined by the signal-to-noise ratio, usually at 105 m above the instrument (fourth range gate).

3. Data and methods

The DWL at JOYCE has been measuring continuously since March of 2012, and the LLJ classification, described in the following section, was applied through the end of 2016. Because of measurement gaps, the resulting dataset contains 1518 days of DWL observations that are analyzed in this study. The HOPE campaign at JOYCE was conducted from 3 April to 31 May 2013 to study the frequently occurring formation of boundary layer cloud during the spring season.

a. Low-level jet detection

In previous studies various criteria were used to detect LLJs in long-term observations to compile an LLJ climatology. In the study by Bonner (1968), LLJs are identified by detecting a wind speed maximum and a 50% decrease above the jet in the lowest 3 km. The LLJ detection algorithm of Baas et al. (2009) uses an absolute and relative criterion for the wind speed maximum and the corresponding minimum above, which is also used in a similar way in Lampert et al. (2015).

In this study, the LLJ identification of Tuononen et al. (2017) is applied to the DWL measurements between 2012 and 2016. In addition, tower measurements at 30 and 50 m are used to fill the observational gap of the DWL below 105 m. A comparison of hourly averaged wind speed measurements during nighttime at 120 m from the tower and the DWL vertical profile reveals a high correlation of 0.95 during the observational period (not shown). Despite the high correlation, the tower measurements are only used when the wind speed difference to the DWL at 120 m does not exceed 2 m s^{-1}. In this way, false classifications due to large deviations between the tower and DWL can be avoided, as a smooth transition of the wind speed between the tower and DWL is ensured and about 13% of the otherwise detected LLJs are neglected.

The LLJ identification algorithm requires a relative and an absolute criterion to be fulfilled to detect an LLJ. The maximum wind speed in each profile must be at least 2 m s^{-1} higher and 25% stronger than the minimum above and below the jet between 30 and 1485 m. In this way small variations in weak wind situations and turbulent fluctuations for stronger winds are prevented from being falsely identified as an LLJ.

After this first step of LLJ identification, the following consistency checks are applied to distinguish between a temporal and spatial continuation of an LLJ and a newly formed LLJ. For an LLJ continuation, the strength and direction of the LLJ maximum should not change by more than 30% and 45°, respectively, between two consecutive profiles measured every 15 min and the LLJ height should stay within four range gates (120 m). In addition to the algorithm of Tuononen et al. (2017), it is required that no data gaps occur between two detected wind speed maxima. Only coherent LLJs that are persistent for at least 1 h are considered. The LLJ speed and direction in this study refer to the measured value at the location of the wind speed maximum, which is referred to as the LLJ height or jet nose.

b. ICON-LEM

The ICON model (Zängl et al. 2015) was developed in a collaboration between the German Weather Service [Deutscher Wetterdienst (DWD)] and the Max Planck Institute for Meteorology (MPI-M) as a new modeling system. Within the framework of the HD(CP)^2 project, the ICON Large-Eddy Model (ICON-LEM) was designed to conduct LES over the whole of Germany to improve moist processes in climate prediction models (Heinze et al. 2017) and is still under development. In this study, the ICON-LEM simulation of one day (2 May 2013) is used to compare with measurements obtained from the HOPE campaign in Jülich and to provide a spatial representation of the wind field. ICON-LEM has already proven to be in agreement with HOPE observations concerning turbulence, column water vapor, and cumulus clouds (when compared with satellite observations), especially for higher grid resolutions (Heinze et al. 2017).

Here, a setup that is similar to that of Heinze et al. (2017) is used and includes four nests with circular domains centered around JOYCE (Fig. 1b). The nests start with a radius of 110 km and a horizontal resolution of 624 m and end with a radius of 10 km and a horizontal resolution of 78 m, which is used in this study. The vertical extent of the simulated domain is about 20 km, with a minimal layer thickness of 20 m and 33 levels in the lowest 2 km. The operational COSMO model covering the German domain (COSMO-DE), as described in Baldauf et al. (2011), is used as forcing data. The utilized model domain with the highest horizontal resolution (78 m), together with the implementation of the topography, can be seen in Fig. 1. The simulation is stored as profiles for the JOYCE site with a 9-s output time and as 3D fields for the whole domain every 10 min. The simulations of this study were conducted on the general purpose Jülich Research on Exascale Cluster Architectures (JURECA) supercomputer, which is operated by the Jülich Supercomputing Centre (JSC) at Forschungszentrum Jülich (Krause and Thörnig 2016). The visualizations of the ICON-LEM model domain are realized using the ParaView software package (Ayachit 2015).

4. Statistical analysis of LLJs

Before evaluating specific nocturnal boundary layer processes related to the presence of LLJs measured by an EC station in section 4b, the climatology and statistics of LLJs and their turbulent properties are analyzed.

a. Climatology of LLJs and their turbulent characteristics

The application of the LLJ detection to the DWL measurements (1518 analyzed days) results in 1020 days

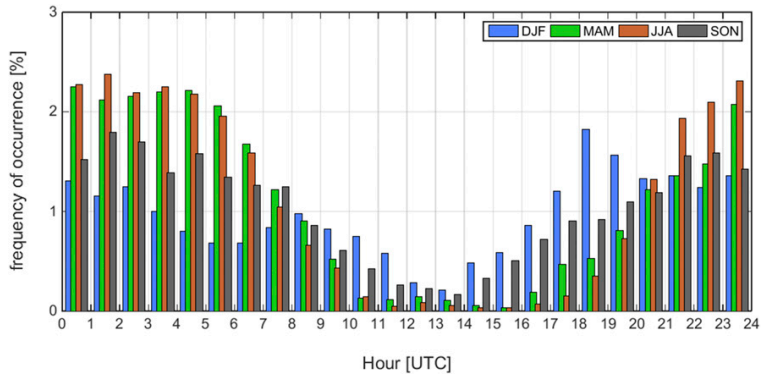

FIG. 2. LLJ frequency of occurrence per hour of the day and for each season relative to the total amount of detected LLJs at JOYCE [local time = UTC + 1 h (winter) or 2 h (summer)]. For an equal number of the different seasons, only LLJs between March 2012 and February 2015 are considered. Total frequencies of occurrence per season are 23% for DJF, 26% for MAM, 26% for JJA, and 25% for SON.

with a detected LLJ of more than 1 h. The data sample includes 1958 periods of continuously detected LLJs, encompassing 17 987 vertical wind profiles and a total frequency of occurrence of 13% during the observational period. In general, the relative occurrence of LLJs reveals a clear diurnal cycle with fewer LLJs during daytime (Fig. 2). The median LLJ height and wind speed during the observational period are 375 m and 8.8 m s^{-1}, respectively.

When sorting all detected LLJs according to the different seasons between March 2012 and February 2015 for an equality of the seasons, it is evident from Fig. 2 that the lowest occurrence of LLJs (23%) is during the winter months [December–February (DJF)]. This result is probably due to a weaker diurnal cycle and therefore a less pronounced temperature difference between day and night, which hampers the jet formation. Also, cloud occurrence is higher in winter, as determined by a 905-nm Vaisala, Inc., CT25k ceilometer at JOYCE, with a mean daily cloud cover of 0.62 as compared with 0.50 for March–May (MAM), 0.47 for June–August (JJA), and 0.55 for September–November (SON). The higher cloud occurrence leads to less radiative cooling in the evening, which is necessary for a decoupling from the friction-governed surface layer and leads to fewer LLJs on winter nights. Between sunrise and sunset, however, the higher cloud cover reduces convective motions and thus the coupling strength, which in turn increases the chance of an LLJ to form. During the shorter daylight period in DJF and SON, LLJ occurrence is increased relative to the summer season, and the peak in wintertime LLJs appears during the evening transition time around 1800 UTC.

The spring (MAM), summer (JJA), and autumn (SON) diurnal cycles are similar, with a slight shift in the decrease in LLJ occurrence in the morning hours and an increase during the evening transition as a result of the different sunrise and sunset times. The relative occurrence in SON is less than in spring and summer during the night, whereas MAM and JJA have the fewest daytime appearances of LLJs. This seasonal difference in LLJ occurrence is in agreement with the LLJ climatology of Baas et al. (2009) at a topographically flat site approximately 200 km away from JOYCE. The differences are explained by a stronger coupling of the boundary layer and the surface in summer during daytime, resulting in a larger amplitude of the nocturnal inertial oscillation. In winter, the higher frequency of cloudy periods with more geostrophic forcing and weaker stable stratification leads to a lower occurrence of LLJs. The results in Fig. 2 are also in good agreement with those from the study by Lampert et al. (2015) for a 1-yr dataset obtained from a similar site that is located 300 km northeast of JOYCE. Note that even such details as the early-morning and late-evening relative maxima in winter occur (see Fig. 5 in Lampert et al. 2015).

A further distinction in the forcing mechanisms of the LLJs is reflected in the distribution of the LLJ direction in comparison with the prevailing wind direction at the median height of all LLJs (375 m). In DJF (and in a similar way for SON) a bimodal distribution of southwesterly–westerly (220°–280°; 55% of all DJF cases) and southeasterly (105°–165°; 25% of all DJF cases) jets can be identified (Fig. 3d), with southwest being the main wind direction at JOYCE in summer and winter (Figs. 3a,b). To relate the observed LLJ wind directions

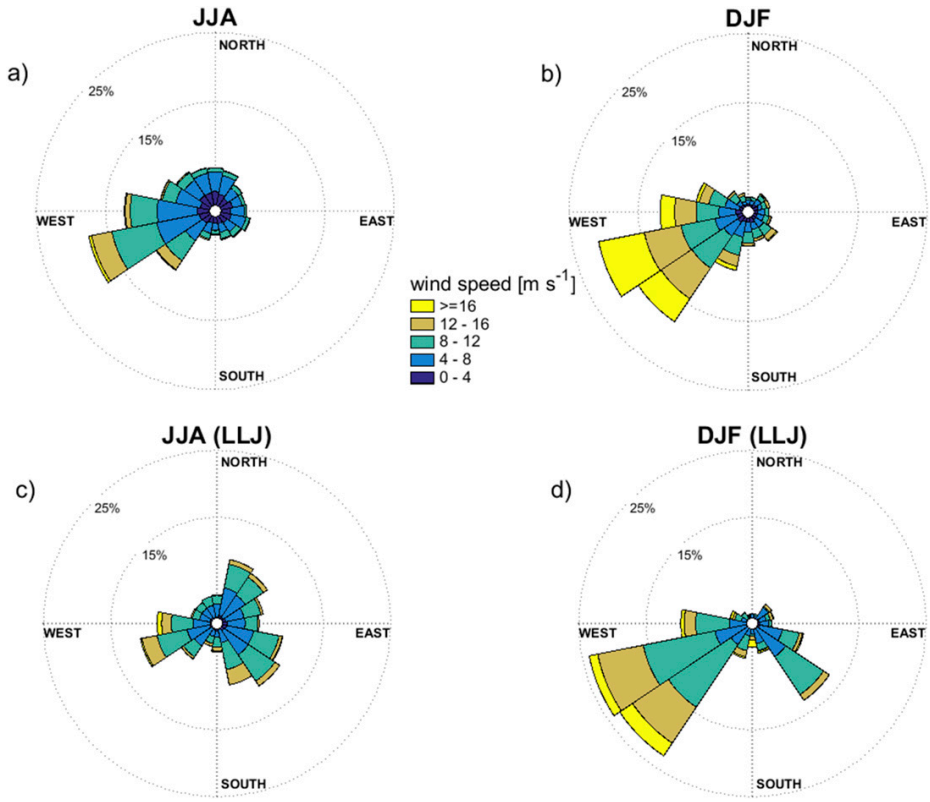

FIG. 3. Wind direction (wind rose) and wind speed (color code) measured at (a),(b) 375 m and (c),(d) the LLJ core at JOYCE between March 2012 and December 2016. The wind roses show results for (left) JJA and (right) DJF.

to the synoptic situation, the 975-hPa geopotential height of the reanalysis product known as ERA-Interim (Dee et al. 2011) is implemented in the Jenkinson–Collison circulation weather type (CWT) classification (Jenkinson and Collison 1977) using the "COST 733" software (Philipp et al. 2016). The CWT model estimates the prevailing wind direction (W, NW, N, NE, E, SE, S, or SW) or the type of circulation [cyclonic (C) or anticyclonic (AC)] four times per day (0000, 0600, 1200, and 1800 UTC). The CWTs are estimated on the basis of the variability of 16 grid points around the JOYCE site with an extent of 5° east–west × 3° north–south.

Overall, about 50% of the CWT classes are detected as W and SW, which is in agreement with the wind roses in Figs. 3a and 3b. The southwest LLJs can therefore be related to the forcing of common southwesterly winds with low pressure to the northwest and high pressure to the southeast. Only 6% of all CWT classes are identified as SE for all wintertime LLJs and 9% for the summertime LLJs. The LLJs originating from this sector (Figs. 3c,d) thus cannot be explained by synoptic forcing, but are most probably connected to a channeling effect by the wide Rur River valley from southeast to northwest. For JJA (and similar for MAM) the distribution of the LLJ direction is broader (Fig. 3c), with a third peak in the northeast (10°–70°; 21% of all JJA cases) connected to an NE circulation weather type, detected in 15% of the summertime LLJ cases. It is also evident that the months DJF have higher wind speeds, since the LLJ speed is higher than 12 m s^{-1} in 26% of all cases in DJF and only in 12% of all cases in JJA. The median jet speeds are 8.3 m s^{-1} for JJA and 9.8 m s^{-1} for DJF, and the median LLJ heights in JJA (375 m) and DJF (345 m) only differ by one DWL range gate.

For the height of the LLJ maximum in the whole observational time period of March 2012–December 2016, 87% of the LLJs have their wind speed maximum below 600 m (Fig. 4a) and 2965 (16%) LLJs occurred below 200 m, which is within the range of wind-turbine rotors. Intermittent turbulence in this region could increase turbine loading through wind shear over the area of the rotor (Peña et al. 2016). For the purpose of

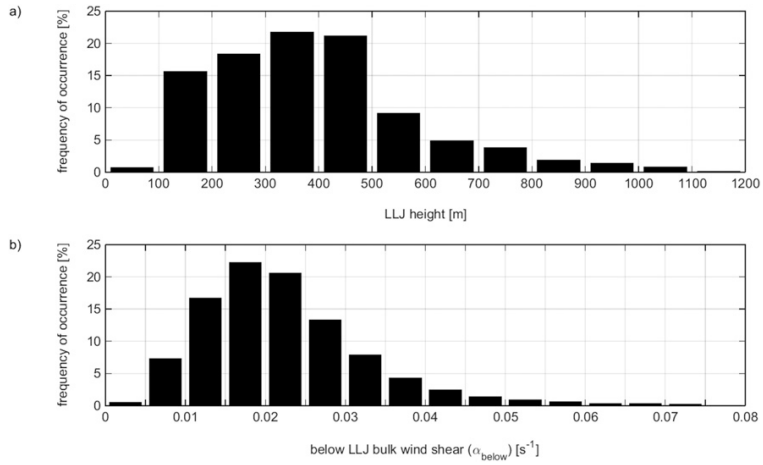

FIG. 4. (a) Height of the LLJ maximum wind speed (bin size = 100 m) and (b) below-LLJ bulk wind shear α_{below} (bin size = 0.005 s^{-1}). The data sample contains all detected LLJs between March 2012 and December 2016 at JOYCE.

analyzing the generation of turbulence below the LLJ as an important attribute for wind-energy applications, the dataset is classified according to the bulk wind shear below the jet, similar to Tuononen et al. (2017):

$$\alpha_{\text{below}} = \frac{U_{\text{LLJ}} - U_{\text{min,below}}}{h_{\text{LLJ}} - h_{\text{min,below}}}, \tag{1}$$

where U_{LLJ} is the wind speed maximum at the height h_{LLJ} and $U_{\text{min,below}}$ is the detected wind speed minimum below the jet with the height $h_{\text{min,below}}$.

To investigate the directional shear, vertical profiles of the vector wind shear U_{shear} can be derived as

$$U_{\text{shear}} = \frac{(\delta u^2 + \delta v^2)^{1/2}}{\delta z}, \tag{2}$$

with differences of the south-to-north v and west-to-east u wind components over a height range δz of 60 m (two range gates).

From Eq. (1), high values of α_{below} represent rapidly increasing wind speeds within a short vertical distance from the surface to the jet nose and therefore a strong gradient (and vice versa). To investigate the turbulence characteristics depending on α_{below}, 30-min standard deviations σ_w of the vertical wind speed around the time of occurrence of the LLJ are derived as an indicator for turbulence. This can be accomplished because of the high temporal resolution of the vertical measurements. In addition, profiles of the horizontal wind speed and vector wind shear U_{shear} [Eq. (2)] of the LLJ periods are extracted from the dataset. The profiles are averaged and scaled by the LLJ speed and height of the LLJ (Fig. 5).

The dataset of wind speed, wind shear, and σ_w profiles during LLJ periods is classified according to the median of the α_{below} distribution (0.02 s^{-1}; Fig. 4b) into low-gradient ($\alpha_{\text{below}} < 0.02\,s^{-1}$) jets (Figs. 5a–d) and strong-gradient jets, with α_{below} being higher than the median (Figs. 5e–h). The low-gradient jets reveal a median jet-nose height of 465 m and a median wind speed of 8.7 m s^{-1}. In comparison, the strong-gradient LLJs with $\alpha_{\text{below}} > 0.02\,s^{-1}$ show not only a lower jet-nose height (315 m) but also higher wind speeds (10.2 m s^{-1}). The strong winds inhibit a further vertical growth of the stable layer and are caused by high nocturnal cooling rates and low geostrophic forcing (Baas et al. 2009). Also the stratification is more stable, resulting in a stronger decoupling; according to Emeis (2017) the magnitude of the wind shear in the subjet layer depends on the vertical temperature gradient below the jet.

For the low-gradient jets, U_{shear} also remains small (Fig. 5b), which is expected because U_{shear} and α_{below} are related to each other. Despite there being some variations in U_{shear} with height, however, no significant turbulence can be seen below and above the jet (Fig. 5c). The strong-gradient LLJs in contrast show high averaged vector wind shear values (U_{shear} up to 0.04 s^{-1}) below the jet nose in the region of strongly decreasing wind speeds with height. This result supports the findings of Svensson and Holtslag (2009), who showed a stronger turning of the wind for a shallower boundary layer height, which is here assumed to be related to the LLJ height. The strongest averaged turbulence (up to

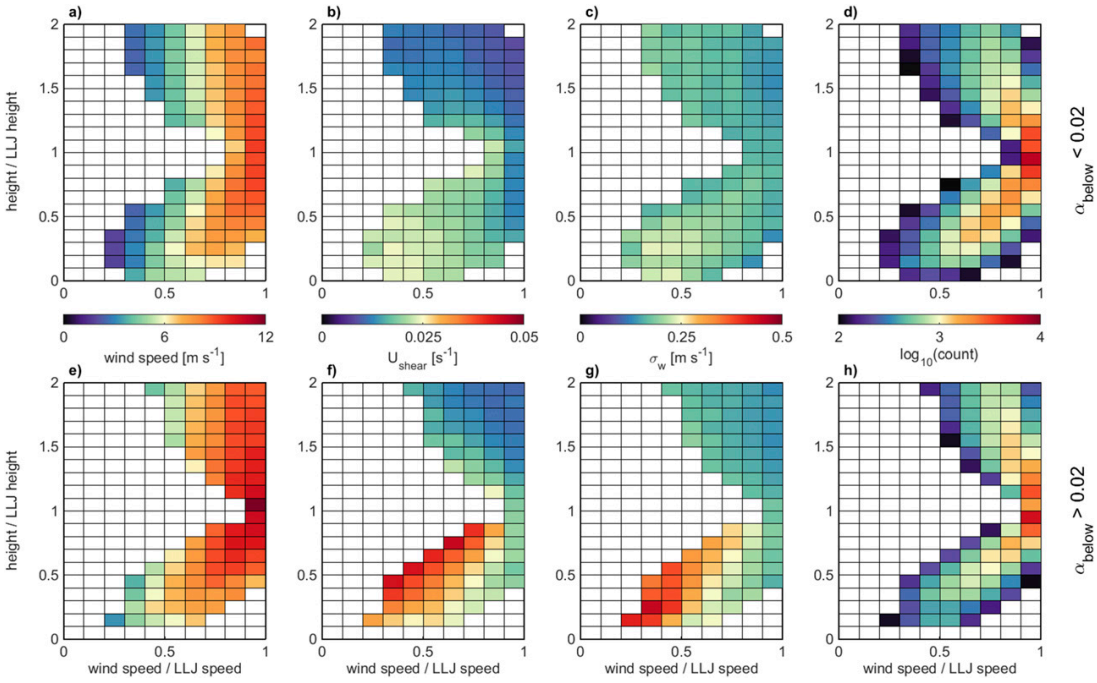

FIG. 5. Distributions of (a),(e) average wind speed, (b),(f) vector wind shear U_{shear}, (c),(g) vertical velocity standard deviation σ_w calculated over 30 min, and (d),(h) number of observations as a function of normalized wind speed (abscissa) and height (ordinate) of the LLJ for cases with (top) low and (bottom) strong wind shear. Only pixels with at least 100 measurements are shown.

$0.4\,m\,s^{-1}$) can be found close to the surface below the region of high U_{shear} values (Fig. 5g). Because of the low LLJ heights in this class, the mean height in the 0.1–0.2 height bin is 117.2 m, which is within the rotor height of wind turbines.

b. *Influences on the surface fluxes*

Note that the lowest 105 m cannot be captured by the DWL. To get information about the differences in turbulence and transport processes closer to the surface, measurements from the EC station 5 km to the southeast of the JOYCE site are evaluated for nocturnal LLJ and no-LLJ periods when no clouds are detected by the DWL (Table 1). The cloud detection is based on a threshold value ($10^{-4}\,m^{-1}\,sr^{-1}$) of the attenuated backscatter measured by the DWL. The largest, statistically significant spread between the two data samples of LLJ and no-LLJ periods is observed during DJF, when there is less influence from the vegetation (maximum vegetation height of 0.4 m) on the surface fluxes. The surface friction is also smaller, leading to decreased turbulent exchange processes.

The LLJ develops above the barrier for heat and momentum fluxes formed by the stable surface layer, as described in Businger (1973). Thereafter, the turbulence near the surface dissipates and strong wind shear associated with a generation of turbulence is present above the surface layer. This is shown in Fig. 5, where the turbulence occurs below the largest shear.

TABLE 1. Median flux values of latent and sensible heat, as well as the net ecosystem CO_2 exchange, friction velocity, Monin–Obukhov stability parameter, standard deviation of the vertical velocity, air pressure, and CO_2 content during periods without LLJs (second column) and with LLJs (third column). The data are obtained at a height of 2.46 m from the EC station using 30-min means during nighttime (from 1 h after sunset until 1 h before sunrise) in DJF between 2012 and 2016. Only times with no clouds identified by the DWL are considered. All distributions are statistically different as based on a 99% confidence interval.

	No LLJ (4039 cases)	LLJ (698 cases)
LH ($W\,m^{-2}$)	6.25	0.65
SH ($W\,m^{-2}$)	−23.97	−11.73
NEE ($\mu mol\,m^{-2}\,s^{-1}$)	0.94	0.74
u_* ($m\,s^{-1}$)	0.18	0.11
z/L	0.06	0.16
σ_w ($m\,s^{-1}$)	0.07	0.02
p_{air} (hPa)	1006.61	1008.79
CO_2 (ppm)	401.2	411.6

The decoupling and reduction of turbulence at the surface during LLJ periods is reflected in the EC measurements by a decrease in the friction velocity u_* and in the vertical velocity standard deviation relative to no-LLJ periods. Also, the higher median value of 0.16 of the Monin–Obukhov stability parameter z/L indicates a more stable regime during the presence of LLJs than during the no-LLJ cases (0.06), which reduces the exchange processes and increases the concentration of emitted gases. This is evident with regard to the increased CO_2 value measured by the EC station during the LLJ periods (411.6 ppm). The increase of 10.4 ppm relative to the no-LLJ periods accounts for more than 40% of the complete CO_2 data-sample standard deviation. The accumulation of near-surface CO_2 during the presence of an LLJ through an elevated wind shear layer acting as a barrier for surface–atmosphere exchange processes is in agreement with the findings of Mathieu et al. (2005).

Also, the latent heat flux LH of 0.65 W m^{-2} during the LLJ periods is much smaller than for the no-LLJ cases (6.25 W m^{-2}). The sensible heat flux SH being closer to zero during LLJ cases and a decrease of more than 20% in the median net ecosystem CO_2 exchange (NEE) supports the assumption of a decoupled surface layer in which all fluxes are reduced. The higher air pressure indicates a synoptic feature of a higher occurrence of LLJs during anticyclonic high pressure flow at this site between December and February.

The turbulence during the LLJ periods is not totally diminished because of an intermittent downward transport of momentum and turbulence, which was also found in EC measurements during LLJs in the study of Prabha et al. (2007). This interaction of the surface layer with the upper-level flow is defined by Mahrt and Vickers (2002) as an upside-down boundary layer. For a detailed study of these interaction processes, as well as a possible recoupling of the layers, tower measurements of the vertical turbulence structure below 100 m could be beneficial.

5. LLJ interaction with the topography

Because the influence of the surrounding topography is of high interest for the interpretation of wind measurements and their representativeness, the hypothesis of a significant effect on the wind field caused by small deviations from flat terrain is investigated in the following. The most prominent feature of the orography in the vicinity of the JOYCE site is a mine dump hill at a distance of approximately 1.8 km to the northeast of the DWL and around 200 m higher than the measurement site. Together with the open-pit mine, which is connected to the southeast of the hill, a heterogeneous orographic surrounding is present. The influence of the hill on the wind field is investigated by means of a case analysis during the HOPE campaign on 2 May 2013, where radiosondes and the ICON-LEM simulation are available for comparison with the DWL measurements.

On this day, with a sunset time of 1851 UTC, an easterly CWT is classified at 1800 UTC. After the breakdown of the convective boundary layer around 1630 UTC, the wind speed measured by the DWL increases below 600 m (Fig. 6a). After 1815 and 2130 UTC two LLJ periods are detected by the DWL, whereas from 1945 until 2130 UTC no further LLJs periods of at least 1 h are detected, since the coherence checks in the algorithm are not fulfilled. In this case the LLJ height between two consecutive profiles differs by more than 120 m. Although the high wind speed is contained throughout the shown time period, the wind direction changes from northeast to southeast (Fig. 7). Therefore, the two detected LLJs can be seen as separate events.

The LLJ classification is also applied to the profiles of the ICON-LEM simulation. The coherence check of the time step between two consecutive wind speed maxima needs to be modified because of the different temporal resolution of the model. A new jet in the ICON-LEM LLJ detection is labeled when a gap of more than 18 s occurs, which is 2 times the output time and similar to the DWL LLJ detection, as described in section 3a. In that way, an LLJ is identified continuously from 1730 to 2200 UTC (Fig. 6b), which is more than 1 h earlier and more persistent than the DWL observations. When bringing the model data to the DWL resolution and applying the same thresholds as for the DWL, the coherent LLJ detection ends at 2015 UTC (Fig. 6c).

In general, the vertical extent and growth of the layer with increased wind speeds between 1730 and 1830 UTC is larger in ICON-LEM. The wind maximum is also sharper and higher in the model. ICON-LEM still captures the main features of the observed wind profiles, however, especially between 1815 and 1945 UTC, when an LLJ is detected by using the DWL observations and the model simulations. This motivates us to use the ICON-LEM simulations as a tool for the investigation of the spatial structure of the wind field.

a. *Influence of a scaled topography on the wind field in ICON-LEM*

Scaling the topography in the ICON-LEM simulations provides a valuable tool for analyzing the sensitivity of the wind field to heterogeneous terrain.

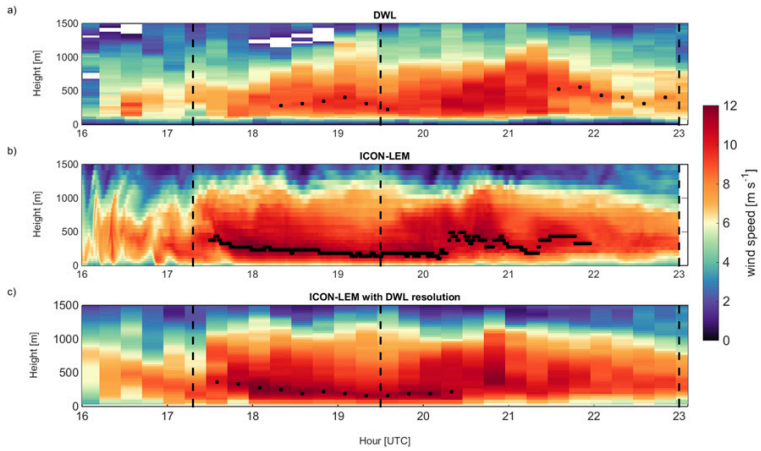

FIG. 6. Wind speed (a) measured by the DWL and tower and (b) simulated by ICON-LEM with an output every 9 s and (c) with the DWL resolution on 2 May 2013 [local time = UTC + 1 h (winter) or 2 h (summer)]. The location of the LLJ height, detected by the LLJ classification, is marked with black dots. The vertical black dashed lines show the selected times for the case analysis in section 5c. Note that on this day the ICON-LEM simulation and the tower measurements are only available until 2300 UTC.

Therefore, streamlines are calculated on 2 May 2013 (2300 UTC) for the lowest 10 model levels of the 3D ICON-LEM simulations with the original topography, but also scaled by factors of 0.5 and 1.5. The scaling factors are a reduction and increase, respectively, of 50% to ensure a significant difference in the model simulations with respect to the topographic effect on the wind field, which is still reasonable for the model setup. More extreme factors might enhance the spinup time or introduce artificial perturbations (because the initial data still include the orography implicitly), whereas less-strong scaling factors might not show any significant difference. During this time a southeasterly LLJ is present, which is shown to be likely connected to a channeling effect as described in section 4a.

When scaling down the topography by a factor of 0.5, it is evident from Fig. 8b that the wind field is less influenced by the orography across the whole domain. The wind speed increases faster with height than in the original simulation (Fig. 8a). The upscaled simulation shows a significant reduction in wind speed, however, especially close to the surface in the region of the

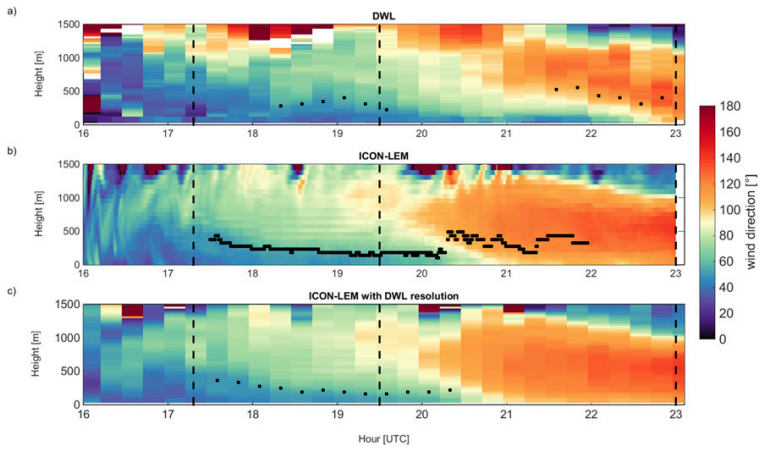

FIG. 7. As in Fig. 6, but for wind direction.

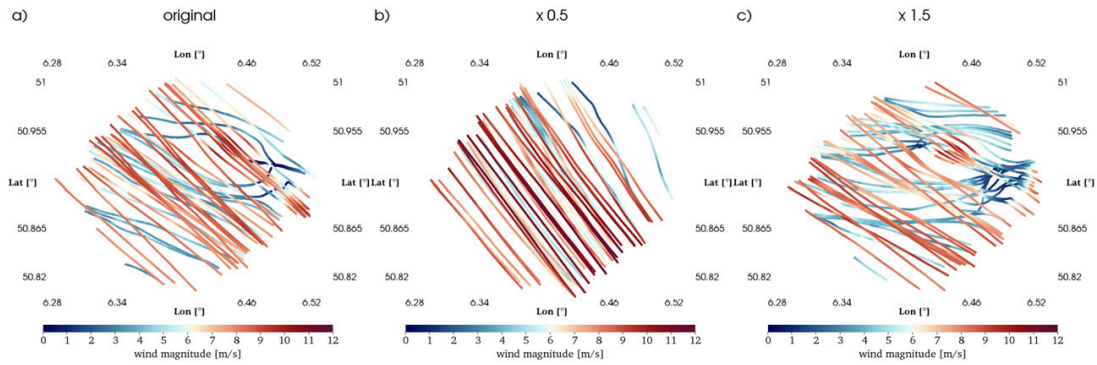

FIG. 8. Streamlines for the 3D ICON-LEM domain snapshot on 2 May 2013 (2300 UTC; southeasterly wind direction). The lowest 10 model levels (up to 790 m MSL) are shown, with the lowest wind speeds (blue) occurring close to the surface and increasing with height. Three simulations are conducted using (a) the original topography and topography that is scaled by factors of (b) 0.5 and (c) 1.5.

open-pit mine (Fig. 8c). The wind speed then increases again over the top of the hill. The topography is also influencing the wind direction by up to 45° for the lower elevations, which can be seen by the more easterly streamlines in the upscaled and original simulations. This finding indicates that the small but close hill to the northeast of the JOYCE site can act as an additional barrier to the channeling effect induced by the large-scale topography surrounding the site.

b. *Comparison of observations and ICON-LEM for a nocturnal LLJ*

For a better comparison of the measurements and model output, profiles of wind speed, wind direction, vertical wind speed, and potential temperature around the time of the LLJ presence are shown in Fig. 9. Because the vertical velocity is highly variable in both space and time, the ICON-LEM and DWL profiles need to be averaged. The DWL vertical velocity measurements are therefore averaged to 30 min. To account for a similar variability in the ICON-LEM vertical wind, but also to obtain simulated quantities that are comparable to the DWL scans, a spatial average of the model output is calculated. The $1.9 \times 1.9\,\mathrm{km}^2$ area around the JOYCE site (see the black-outlined square in Fig. 10) is selected such that it covers the same area as the DWL scan during 30 min: winds with an average speed of $8\,\mathrm{m\,s^{-1}}$ (which is found during this time period) would travel 14 km during 30 min. At 470 m, which is approximately in the middle of the considered height range, the diameter of the DWL scan at 75° elevation is 250 m. This results in the same surface area as chosen for averaging the ICON-LEM output ($14\,\mathrm{km} \times 0.25\,\mathrm{km} = 3.61\,\mathrm{km}^2 = 1.9 \times 1.9\,\mathrm{km}^2$). Three times are considered in the case analysis, including the LLJ initiation phase at 1720 UTC, the developed LLJ at 1930 UTC, and a weaker LLJ phase with a change of direction at 2300 UTC. For the times 1720 and 2300 UTC profiles from radiosonde ascents are also available.

In general, the wind speed and direction profiles show good agreement (Figs. 9a,b,e,f,i,j), with only ICON-LEM overestimating the wind speed. In the evening transition period around 1720 UTC, turbulence is still present up to the mixing height at 285 m (dashed lines in Figs. 9a–d), defined as the height at which the standard deviation of the vertical velocity over 30 min drops below $0.4\,\mathrm{m\,s^{-1}}$, which can be used as an indicator for vertical mixing (Schween et al. 2014). Therefore, the 30-min standard deviation of the DWL is highest within the mixing layer (Fig. 9c). The turbulent motion, as well as the distance of the radiosonde launch site to the DWL, can explain parts of the deviations between the wind speed profiles below 300 m. In addition, the launch site is located at the southeastern corner of the hill and is therefore not shaded from the northeasterly wind.

During the LLJ period at 1930 UTC (Figs. 9e–h) the turbulence only reaches up to 135 m and the LLJ has formed with a maximum wind speed of $9.8\,\mathrm{m\,s^{-1}}$ at 225 m, as determined by the DWL (Fig. 9e). The wind direction close to the ground is still northeasterly, and it turns clockwise toward the geostrophic wind with height (Fig. 9f). For the ICON-LEM potential temperature profile, stable stratification can be identified, especially above the mixing-layer height from the DWL (Fig. 9h). The DWL shows increased positive vertical velocity values of up to $0.5\,\mathrm{m\,s^{-1}}$ around 600 m, a result that is not captured by ICON-LEM.

With a change in near-surface wind direction to southeasterly at 2300 UTC (Fig. 9j), the distinct LLJ profile vanishes together with the vertical updraft (Figs. 9i,k). The potential temperature profile measured by the RS shows a stable surface layer up to about 150 m and a neutral stratified layer until 600 m, followed again

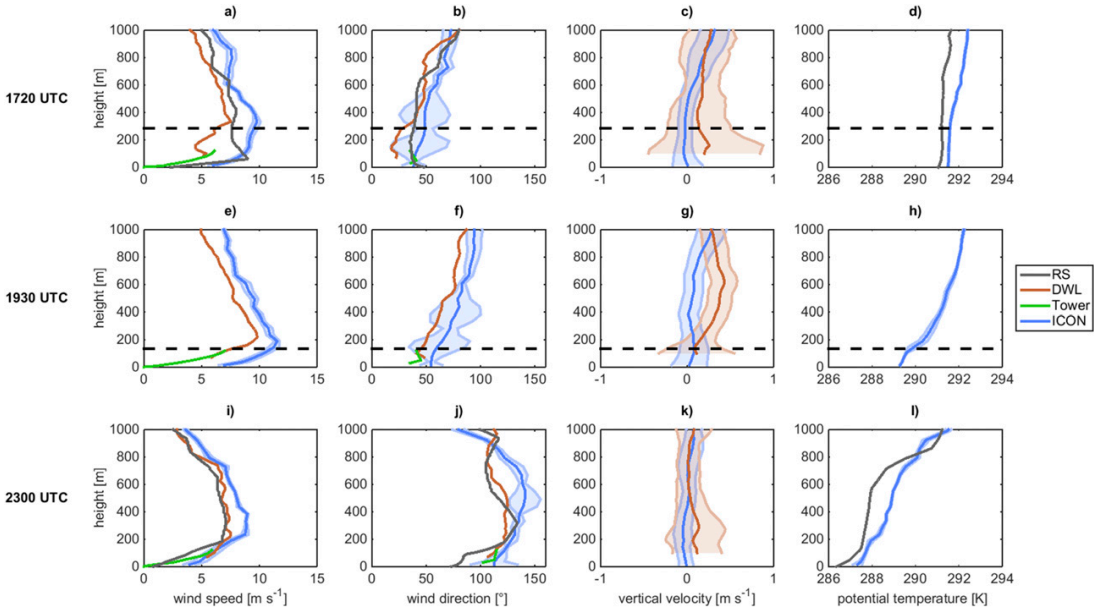

FIG. 9. Case analysis on 2 May 2013 with profiles of (a),(e),(i) wind speed, (b),(f),(j) wind direction, (c),(g),(k) vertical velocity, and (d),(h),(l) potential temperature. The measurements from RSs (gray line), DWL (red line), and the tower (green line), as well as the ICON-LEM output (blue line), are shown for (top) 1720, (middle) 1930, and (bottom) 2300 UTC. The ICON-LEM profiles are spatially averaged over 1.9 km × 1.9 km and the standard deviation [for wind direction calculated with the method of Yamartino (1984)] is shaded in light blue. The DWL vertical velocity is temporally averaged over 30 min, with the standard deviation given in reddish shading. The mixing-layer height after Schween et al. (2014) is shown by a black dashed line.

by a stable layer. This might indicate a decoupling at the surface from the adjacent residual layer reaching up to 600 m. These are favorable conditions for an LLJ, which is also detected using the DWL measurements.

c. *Topographic influence on the vertical wind*

To understand the differences in the vertical wind between ICON-LEM and the DWL, the vertical velocity of the 3D ICON-LEM domain is evaluated at 300 m MSL (Fig. 10). This height is chosen to be above the highest surface point in the model domain. During the LLJ period at 1930 UTC the vertical velocities simulated by ICON-LEM reveal updrafts on the windward side and downdraft motions leeward of the hill with the wind coming from the northeast (Fig. 10b). Thus, the orographic disturbance induces vertical wind

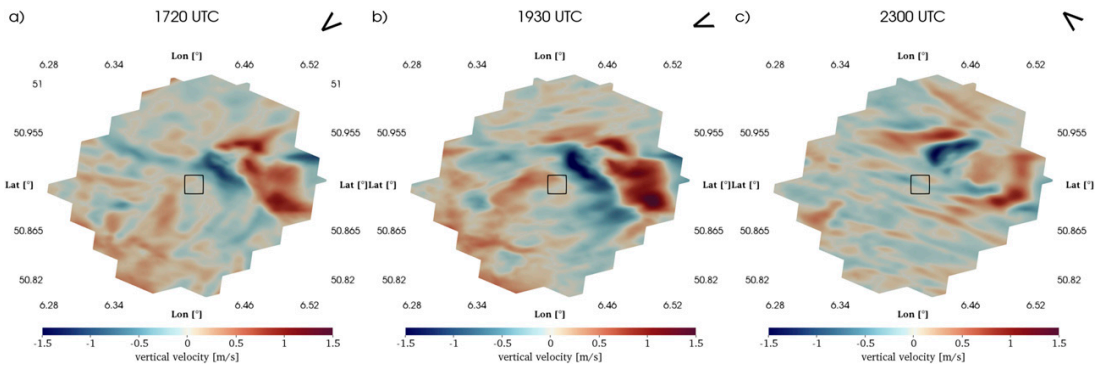

FIG. 10. Vertical velocity at 300 m MSL of the ICON-LEM domain snapshots at (a) 1720, (b) 1930, and (c) 2300 UTC 2 May 2013. The black-outlined square denotes the 1.9 km × 1.9 km area around the JOYCE site, where the average vertical velocity profiles from Fig. 9 are calculated. The black arrow in the top-right corner of (a)–(c) shows the wind direction at JOYCE around 300 m.

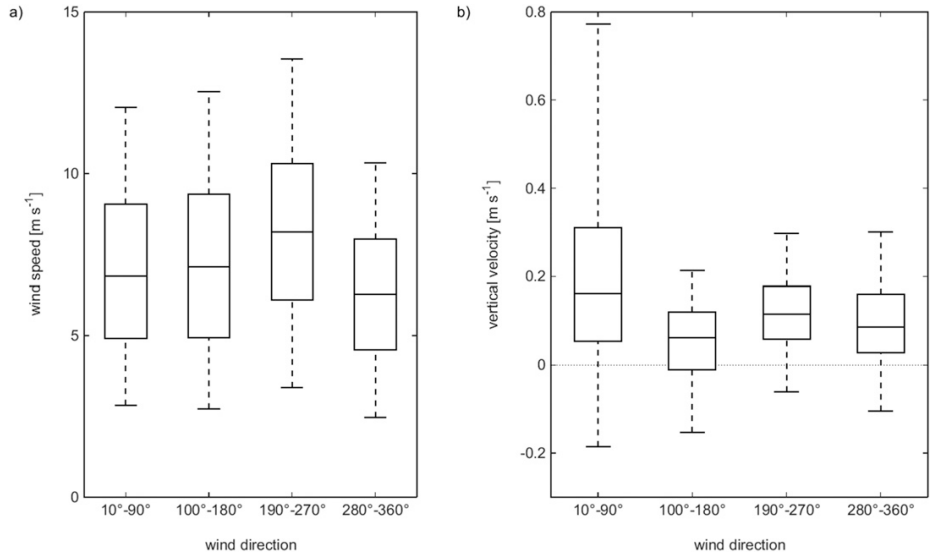

FIG. 11. Box plots showing the 5th, 25th, 50th, 75th, and 95th percentiles of (a) wind speed and (b) 30-min averages of the vertical velocity measured by the DWL between 225 and 705 m. Only LLJs below 500 m during nighttime (from 1 h after sunset until 1 h before sunrise) and clear-sky (DWL backscatter $< 10^{-4}\,\mathrm{m^{-1}\,sr^{-1}}$) conditions are included. The wind speed between 105 and 225 m needs to be above $4\,\mathrm{m\,s^{-1}}$, and the data are binned according to the wind direction (bin size = 80°) in this range with 10° separation. The numbers of cases are 1310 (10°–90°), 2564 (100°–180°), 2142 (190°–270°), and 525 (280°–360°).

variations up to approximately $3\,\mathrm{m\,s^{-1}}$, with the JOYCE site located in an updraft region, as also was seen by the DWL (Fig. 9g). The strong gradients in the ICON-LEM vertical wind field can explain the deviations to the observations by a slight spatial displacement. At 2300 UTC the simulated spatial pattern in the vertical velocity (Fig. 10c) is changed according to the turning of the wind direction and a wavelike structure is visible, caused by the wind first flowing down the depression of the pit mine and then uphill.

The results of the case analysis suggest that the updrafts measured at the JOYCE site are caused by the topography for northeasterly winds. In the following, we investigate if this statement can be verified using long-term measurements. Therefore, the DWL dataset from 2012 to 2016 is sampled for LLJs below 500 m during clear-sky conditions, since drizzle events could influence the vertical velocity estimates. Furthermore, it is required that the wind speed between 105 and 225 m exceeds $4\,\mathrm{m\,s^{-1}}$ to ensure a sufficiently strong updraft. Convective motions are excluded by only considering nighttime cases. The data sample of wind speed and 30-min averages of the vertical wind above the summit of the hill (from 225 to 705 m) is classified into different directional classes to investigate the effect of the hill to the northeast (10°–90°) relative to the other directions (Fig. 11).

The wind speed distribution of the direction in the range of 190°–270° reveals higher values, with a median value of $8.2\,\mathrm{m\,s^{-1}}$ that exceeds the median values in the other directional classes by $1.1–1.9\,\mathrm{m\,s^{-1}}$ (Fig. 11a). Although the effect is small relative to the range of observed wind speed values (standard deviation around $3\,\mathrm{m\,s^{-1}}$), a possible explanation could be the influence of frontal systems predominantly coming from the southwest.

Despite lower wind speeds, a significant shift to higher positive vertical wind speed values and by far the highest variability can be found in the 10°–90° directional class (Fig. 11b). The 75th percentile ($0.3\,\mathrm{m\,s^{-1}}$) of the 10°–90° class is around or even higher than the 95th percentiles of the other distributions. The longer tail toward negative vertical velocity values observed for the northeasterly wind directions could be explained by a slight shift of the updraft region after the descending motions at the leeward side of the hill, as seen in the ICON-LEM simulation, or a higher degree of turbulence induced by the topography. The overall shift to positive values indicated by all distributions of the vertical velocity is probably due to a small offset of the instrument on the order of a few centimeters per second. It can be conclusively stated from the model simulations and the DWL observations that the moderate topography around JOYCE shows sufficient heterogeneity to cause significant disturbances in the wind field.

6. Summary and conclusions

The LLJ climatology obtained from the long-term observations (March 2012–December 2016) by the Doppler wind lidar at the JOYCE site in western Germany shows a clear diurnal cycle of the occurrence of LLJs, favoring the nighttime appearance of the jets. In total, LLJs are detected in 13% of the observational period. Seasonal differences in the diurnal LLJ frequency of occurrence can mostly be attributed to the length of the day. Fewer but stronger LLJs occur in the winter months, because of the lower temperature gradients between day and night and strong geostrophic forcing. An analysis of the synoptic situation using circulation weather types showed that the predominant southwesterly direction of the jets is in agreement with the general circulation around JOYCE. The southeasterly LLJs cannot be associated with the synoptic forcing but rather are more related to a local channeling effect.

The turbulent characteristics of the LLJs, provided by the Doppler wind lidar, showed notably higher vector wind shear below the jet nose for LLJs with strongly decreasing wind speeds below the jet. When dividing all LLJs according to the bulk wind shear, significant turbulent motions can only be found close to the surface for jets with high bulk wind shear. The characterization of the turbulence associated with LLJs shows the importance for wind-energy production, since a large number of LLJs (2965; 16% of all jets) are detected in the range of the rotor height below 200 m.

Evaluation of the nighttime EC-station measurements proves the concept of Businger (1973) of a decoupled surface layer during LLJ events. The strong wind shear associated with the LLJ together with the nonturbulent stable layer hampers upward mixing, which leads to an accumulation of carbon dioxide (CO_2) and a reduction of the heat and momentum fluxes in the stable surface layer. Turbulent mixing found at the surface might be generated by a recoupling of the flow through intermittent downward transport of jet-induced turbulence. This concept of an upside-down boundary layer is explained by Mahrt and Vickers (2002) and could be further analyzed using detailed measurements of the vertical structure of near-surface turbulence.

In the comprehensive case analysis, a strong interaction of the winds with the topography, dominated by a 200-m-high hill and a pit mine close to the measurement site, can be observed during an LLJ event. The DWL shows high positive vertical velocities for northeasterly LLJs, when the wind is flowing over the hill toward the instrument's field of view. High-resolution simulations of ICON-LEM, as a self-consistent representation of the atmosphere, help in the analysis of the spatial variations of the wind field. The vertical velocities reveal a wave structure induced by the hill and pit mine, which are also influencing the wind speed and direction. From a long-term perspective, this influence introduces a much stronger variability in the vertical wind for the location of the DWL, depending on the wind direction.

The results of the long-term assessment, as well as the model simulations presented in this study, stress the importance of analyzing LLJs and their local effects. The LLJ identification algorithm of Tuononen et al. (2017) proved to be able to identify LLJs objectively by utilizing a multiyear dataset of high temporal and vertical resolution Doppler lidar measurements. The method can further be used for evaluating model performance in terms of the correct representation of LLJ characteristics. By including additional information on atmospheric turbulence, which can be derived from Doppler wind lidars, the impact of LLJs on wind turbines can be examined.

Acknowledgments. The authors acknowledge the Transregional Collaborative Research Centre (TR32) ''Patterns in Soil-Vegetation-Atmosphere Systems'' funded by the German Science Foundation (DFG), which has continuously contributed to the instrumentation of JOYCE and its maintenance as well as funding T. Marke. The measurement infrastructure providing EC data was supported by the Terrestrial Environmental Observatories (TERENO), funded by the Helmholtz Association. Part of the work has been granted by Energy Transition and Climate Change (ET-CC) under DFG Grant ZUK 81. The ICON-LEM simulations are incorporated by the HD(CP)^2 research initiative funded by the German Ministry for Education and Research (BMBF). Furthermore, the authors gratefully acknowledge the computing time granted by the John von Neumann Institute for Computing and provided on the supercomputer JURECA at the JSC. Access to the meteorological tower observations was made possible through Axel Knaps from the Research Centre Jülich. The work of M. Tuonnonen is funded by the Maj and Tor Nessling Foundation (Grants 201500300 and 201600003).

REFERENCES

Ayachit, U., 2015: *The ParaView Guide: A Parallel Visualization Application*. Kitware, Inc., 340 pp.

Baas, P., F. C. Bosveld, H. Klein Baltink, and A. A. M. Holtslag, 2009: A climatology of nocturnal low-level jets at Cabauw. *J. Appl. Meteor. Climatol.*, **48**, 1627–1642, https://doi.org/10.1175/2009JAMC1965.1.

Baldauf, M., A. Seifert, J. Förstner, D. Majewski, M. Raschendorfer, and T. Reinhardt, 2011: Operational convective-scale numerical weather prediction with the COSMO model: Description and sensitivities. *Mon. Wea. Rev.*, **139**, 3887–3905, https://doi.org/10.1175/MWR-D-10-05013.1.

Banta, R., R. K. Newsom, J. K. Lundquist, Y. L. Pichugina, R. L. Coulter, and L. Mahrt, 2002: Nocturnal low-level jet characteristics over Kansas during CASES-99. *Bound.-Layer Meteor.*, **105**, 221–252, https://doi.org/10.1023/A:1019992330866.

Blackadar, A. K., 1957: Boundary layer wind maxima and their significance for the growth of nocturnal inversions. *Bull. Amer. Meteor. Soc.*, **38**, 283–290.

Bonner, W. D., 1968: Climatology of the low level jet. *Mon. Wea. Rev.*, **96**, 833–850, https://doi.org/10.1175/1520-0493(1968)096<0833:COTLLJ>2.0.CO;2.

Businger, J. A., 1973: Turbulent transfer in the atmospheric surface layer. *Workshop on Micrometerology*, D. H. Haugen, Ed., Amer. Meteor. Soc., 67–100.

Dee, D. P., and Coauthors, 2011: The ERA-Interim reanalysis: Configuration and performance of the data assimilation system. *Quart. J. Roy. Meteor. Soc.*, **137**, 553–597, https://doi.org/10.1002/qj.828.

Dipankar, A., B. Stevens, R. Heinze, C. Moseley, G. Zängl, M. Giorgetta, and S. Brdar, 2015: Large eddy simulation using the general circulation model ICON. *J. Adv. Model. Earth Syst.*, **7**, 963–986, https://doi.org/10.1002/2015MS000431.

Dörenkämper, M., M. Optis, A. Monahan, and G. Steinfeld, 2015: On the offshore advection of boundary-layer structures and the influence on offshore wind conditions. *Bound.-Layer Meteor.*, **155**, 459–482, https://doi.org/10.1007/s10546-015-0008-x.

Emeis, S., 2017: Upper limit for wind shear in stably stratified conditions expressed in terms of a bulk Richardson number. *Meteor. Z.*, **26**, 421–430, https://doi.org/10.1127/metz/2017/0828.

——, M. Harris, and R. M. Banta, 2007: Boundary-layer anemometry by optical remote sensing for wind energy applications. *Meteor. Z.*, **16**, 337–347, https://doi.org/10.1127/0941-2948/2007/0225.

Heinze, R., and Coauthors, 2017: Large-eddy simulations over Germany using ICON: A comprehensive evaluation. *Quart. J. Roy. Meteor. Soc.*, **143**, 69–100, https://doi.org/10.1002/qj.2947.

Higgins, R. W., Y. Yao, E. S. Yarosh, J. E. Janowiak, and K. C. Mo, 1997: Influence of the Great Plains low-level jet on summertime precipitation and moisture transport over the central United States. *J. Climate*, **10**, 481–507, https://doi.org/10.1175/1520-0442(1997)010<0481:IOTGPL>2.0.CO;2.

Hirsikko, A., and Coauthors, 2014: Observing wind, aerosol particles, cloud and precipitation: Finland's new ground-based remote-sensing network. *Atmos. Meas. Tech.*, **7**, 1351–1375, https://doi.org/10.5194/amt-7-1351-2014.

Holtslag, A. A. M., and Coauthors, 2013: Stable atmospheric boundary layers and diurnal cycles: Challenges for weather and climate models. *Bull. Amer. Meteor. Soc.*, **94**, 1691–1706, https://doi.org/10.1175/BAMS-D-11-00187.1.

Jenkinson, A. F., and F. P. Collison, 1977: An initial climatology of gales over the North Sea. Met Office Synoptic Climatology Branch Memo. 62, 18 pp.

Krause, D., and P. Thörnig, 2016: JURECA: General-purpose supercomputer at Jülich Supercomputing Centre. *J. Large-Scale Res. Facil.*, **2**, A62, https://doi.org/10.17815/jlsrf-2-121.

Lampert, A., B. Bernalte Jimenez, G. Gross, D. Wulff, and T. Kenull, 2015: One-year observations of the wind distribution and low-level jet occurrence at Braunschweig, north German plain. *Wind Energy*, **19**, 1807–1817, https://doi.org/10.1002/we.1951.

——, and Coauthors, 2016: A study of local turbulence and anisotropy during the afternoon and evening transition with an unmanned aerial system and mesoscale simulation. *Atmos. Chem. Phys.*, **16**, 8009–8021, https://doi.org/10.5194/acp-16-8009-2016.

Löhnert, U., and Coauthors, 2015: JOYCE: Jülich Observatory for Cloud Evolution. *Bull. Amer. Meteor. Soc.*, **96**, 1157–1174, https://doi.org/10.1175/BAMS-D-14-00105.1.

Macke, A., and Coauthors, 2017: The HD(CP)^2 Observational Prototype Experiment (HOPE)—An overview. *Atmos. Chem. Phys.*, **17**, 4887–4914, https://doi.org/10.5194/acp-17-4887-2017.

Mahrt, L., and D. Vickers, 2002: Contrasting vertical structures of nocturnal boundary layers. *Bound.-Layer Meteor.*, **105**, 351–363, https://doi.org/10.1023/A:1019964720989.

Mathieu, N., I. Strachan, M. Leclerc, A. Karipot, and E. Pattey, 2005: Role of low-level jets and boundary-layer properties on the NBL budget technique. *Agric. For. Meteor.*, **135**, 35–43, https://doi.org/10.1016/j.agrformet.2005.10.001.

Mauder, M., M. Cuntz, C. Drüe, A. Graf, C. Rebmann, H. P. Schmid, M. Schmidt, and R. Steinbrecher, 2013: A strategy for quality and uncertainty assessment of long-term eddy-covariance measurements. *Agric. For. Meteor.*, **169**, 122–135, https://doi.org/10.1016/j.agrformet.2012.09.006.

Mitchell, M. J., R. W. Arritt, and K. Labas, 1995: A climatology of the warm season Great Plains low-level jet using wind profiler observations. *Wea. Forecasting*, **10**, 576–591, https://doi.org/10.1175/1520-0434(1995)010<0576:ACOTWS>2.0.CO;2.

O'Connor, E. J., A. J. Illingworth, I. M. Brooks, C. D. Westbrook, R. J. Hogan, F. Davies, and B. J. Brooks, 2010: A method for estimating the turbulent kinetic energy dissipation rate from a vertically pointing Doppler lidar, and independent evaluation from balloon-borne in situ measurements. *J. Atmos. Oceanic Technol.*, **27**, 1652–1664, https://doi.org/10.1175/2010JTECHA1455.1.

Päschke, E., R. Leinweber, and V. Lehmann, 2015: An assessment of the performance of a 1.5 μm Doppler lidar for operational vertical wind profiling based on a 1-year trial. *Atmos. Meas. Tech.*, **8**, 2251–2266, https://doi.org/10.5194/amt-8-2251-2015.

Pearson, G., F. Davies, and C. Collier, 2009: An analysis of the performance of the UFAM pulsed Doppler lidar for observing the boundary layer. *J. Atmos. Oceanic Technol.*, **26**, 240–250, https://doi.org/10.1175/2008JTECHA1128.1.

Peña, A., and Coauthors, 2016: Ten years of boundary-layer and wind-power meteorology at Høvsøre, Denmark. *Bound.-Layer Meteor.*, **158**, 1–26, https://doi.org/10.1007/s10546-015-0079-8.

Philipp, A., C. Beck, R. Huth, and J. Jacobeit, 2016: Development and comparison of circulation type classifications using the COST 733 dataset and software. *Int. J. Climatol.*, **36**, 2673–2691, https://doi.org/10.1002/joc.3920.

Prabha, T. V., M. Y. Leclerc, A. Karipot, and D. Y. Hollinger, 2007: Low-frequency effects on eddy covariance fluxes under the influence of a low-level jet. *J. Appl. Meteor. Climatol.*, **46**, 338–352, https://doi.org/10.1175/JAM2461.1.

Schween, J. H., A. Hirsikko, U. Löhnert, and S. Crewell, 2014: Mixing-layer height retrieval with ceilometer and Doppler lidar: From case studies to long-term assessment. *Atmos. Meas. Tech.*, **7**, 3685–3704, https://doi.org/10.5194/amt-7-3685-2014.

Stensrud, D., 1996: Importance of low-level jets to climate: A review. *J. Climate*, **9**, 1698–1711, https://doi.org/10.1175/1520-0442(1996)009<1698:IOLLJT>2.0.CO;2.

Storm, B., J. Dudhia, S. Basu, A. Swift, and I. Giammanco, 2009: Evaluation of the Weather Research and Forecasting Model on forecasting low-level jets: Implications for wind energy. *Wind Energy*, **12**, 81–90, https://doi.org/10.1002/we.288.

Su, J., M. Felton, L. Lei, M. P. McCormick, R. Delgado, and A. St. Pé, 2016: Lidar remote sensing of cloud formation caused by low-level jets: Cloud formation caused by low-level jets. *J. Geophys. Res. Atmos.*, **121**, 5904–5911, https://10.1002/2015JD024590.

Svensson, G., and A. A. M. Holtslag, 2009: Analysis of model results for the turning of the wind and related momentum fluxes in the stable boundary layer. *Bound.-Layer Meteor.*, **132**, 261–277, https://doi.org/10.1007/s10546-009-9395-1.

Tuononen, M., V. A. Sinclair, and T. Vihma, 2015: A climatology of low-level jets in the mid-latitudes and polar regions of the Northern Hemisphere: A climatology of low-level jets. *Atmos. Sci. Lett.*, **16**, 492–499, https://doi.org/10.1002/asl.587.

——, E. J. O'Connor, V. A. Sinclair, and V. Vakkari, 2017: Low-level jets over Utö, Finland, based on Doppler lidar observations. *J. Appl. Meteor. Climatol.*, **56**, 2577–2594, https://doi.org/10.1175/JAMC-D-16-0411.1.

Whiteman, C. D., X. Bian, and S. Zhong, 1997: Low-level jet climatology from enhanced rawinsonde observations at a site in the southern Great Plains. *J. Appl. Meteor.*, **36**, 1363–1376, https://doi.org/10.1175/1520-0450(1997)036<1363:LLJCFE>2.0.CO;2.

Yamartino, R. J., 1984: A comparison of several single-pass estimators of the standard deviation of wind direction. *J. Climate Appl. Meteor.*, **23**, 1362–1366, https://doi.org/10.1175/1520-0450(1984)023<1362:ACOSPE>2.0.CO;2.

Zängl, G., D. Reinert, P. Rípodas, and M. Baldauf, 2015: The ICON (ICOsahedral Non-hydrostatic) modelling framework of DWD and MPI-M: Description of the non-hydrostatic dynamical core. *Quart. J. Roy. Meteor. Soc.*, **141**, 563–579, https://doi.org/10.1002/qj.2378.

Zhong, S., J. D. Fast, and X. Bian, 1996: A case study of the Great Plains low-level jet using wind profiler network data and a high-resolution mesoscale model. *Mon. Wea. Rev.*, **124**, 785–806, https://doi.org/10.1175/1520-0493(1996)124<0785:ACSOTG>2.0.CO;2.

Zhou, B., and F. K. Chow, 2012: Turbulence modeling for the stable atmospheric boundary layer and implications for wind energy. *Flow Turbul. Combust.*, **88**, 255–277, https://doi.org/10.1007/s10494-011-9359-7.

IV

Atmospheric Chemistry and Physics, 19, 1985–2000,
doi:10.5194/acp-19-1985-2019

Atmos. Chem. Phys., 19, 1985–2000, 2019
https://doi.org/10.5194/acp-19-1985-2019

Atmospheric Chemistry and Physics
Open Access
EGU

Evaluating solar radiation forecast uncertainty

Minttu Tuononen[1], **Ewan J. O'Connor**[1,2], **and Victoria A. Sinclair**[3]

[1]Finnish Meteorological Institute, Helsinki, Finland
[2]Department of Meteorology, University of Reading, Reading, UK
[3]Institute for Atmospheric and Earth System Research/Physics, Faculty of Science, University of Helsinki, Helsinki, Finland

Correspondence: Minttu Tuononen (minttu.tuononen@vaisala.com)

Received: 1 November 2018 – Discussion started: 13 November 2018
Revised: 13 January 2019 – Accepted: 16 January 2019 – Published: 14 February 2019

Abstract. The presence of clouds and their characteristics have a strong impact on the radiative balance of the Earth and on the amount of solar radiation reaching the Earth's surface. Many applications require accurate forecasts of surface radiation on weather timescales, for example solar energy and UV radiation forecasts. Here we investigate how operational forecasts of low and mid-level clouds affect the accuracy of solar radiation forecasts. A total of 4 years of cloud and solar radiation observations from one site in Helsinki, Finland, are analysed. Cloud observations are obtained from a ceilometer and therefore we first develop algorithms to reliably detect cloud base, precipitation, and fog. These new algorithms are widely applicable for both operational use and research, such as in-cloud icing detection for the wind energy industry and for aviation. The cloud and radiation observations are compared to forecasts from the Integrated Forecast System (IFS) run operationally and developed by the European Centre for Medium-Range Weather Forecasts (ECMWF). We develop methods to evaluate the skill of the cloud and radiation forecasts. These methods can potentially be extended to hundreds of sites globally.

Over Helsinki, the measured global horizontal irradiance (GHI) is strongly influenced by its northerly location and the annual variation in cloudiness. Solar radiation forecast error is therefore larger in summer than in winter, but the relative error in the solar radiation forecast is more or less constant throughout the year. The mean overall bias in the GHI forecast is positive ($8\,\mathrm{W\,m^{-2}}$). The observed and forecast distributions in cloud cover, at the spatial scales we are considering, are strongly skewed towards clear-sky and overcast situations. Cloud cover forecasts show more skill in winter when the cloud cover is predominantly overcast; in summer there are more clear-sky and broken cloud situations. A negative bias was found in forecast GHI for correctly forecast clear-sky cases and a positive bias in correctly forecast overcast cases. Temporal averaging improved the cloud cover forecast and hence decreased the solar radiation forecast error. The positive bias seen in overcast situations occurs when the model cloud has low values of liquid water path (LWP). We attribute this bias to the model having LWP values that are too low or the model optical properties for clouds with low LWP being incorrect.

1 Introduction

Accurate forecasts of solar radiation are valuable for solar energy, such as predicting power generation 1 day ahead for energy markets, and for public health reasons, such as forecasting the amount of UV radiation. The amount of solar radiation at the surface is highly dependent on the solar zenith angle and clouds. However, clouds are highly variable in space and time, as are their optical properties, and therefore solar radiation forecasts require accurate cloud forecasts. Many applications only require reliable climatologies of the solar resource, such as solar resource assessments for solar energy installations (Kleissl, 2013). Observed climatologies can be obtained from surface-based instrumentation (Ohmura et al., 1998) and from satellite (Posselt et al., 2012; López and Batlles, 2014; Müller et al., 2015). Climatologies can also be derived from Numerical Weather Prediction (NWP) forecasts and reanalyses, which are attractive from a cost perspective but may display larger uncertainties than observations (Jia et al., 2013; Boilley and Wald, 2015; Frank et al., 2018; Urraca et al., 2018). Climatologies require that the correct amount and type of cloud is predicted on average, whereas a

forecast additionally requires that the cloud is forecast at the right time.

Evaluating cloud forecasts and their impact on solar radiation has been performed using ground-based observations; Ahlgrimm and Forbes (2012) investigated the impact of low clouds on solar radiation in the Integrated Forecast System (IFS) of the European Centre for Medium-Range Weather Forecasts (ECMWF) at the Atmospheric Radiation Measurement (ARM) Southern Great Plains (SGP) site in the US using cloud radar, micropulse lidar, and surface radiation measurements; Van Weverberg et al. (2018) investigated the positive temperature bias in the lower troposphere at SGP in nine different models, which was attributed to an overestimate of the net surface shortwave radiation arising from incorrectly modelled cloud radiative effects. Earlier studies also suggest that supercooled liquid layers are not correctly represented in NWP models (Ahlgrimm and Forbes, 2012; Forbes and Ahlgrimm, 2014).

Continuous verification of the vertical representation of clouds in forecast models is available through Cloudnet (Illingworth et al., 2007); however, this requires comprehensive ground-based cloud observing systems, e.g. ARM (Mather and Voyles, 2013) and Cloudnet, which are sparsely distributed across the globe. Verification of the column-integrated cloud amount (cloud cover) can be performed at many more locations using operational SYNOP and/or ceilometer observations (Mittermaier, 2012). Ceilometers are much more widely distributed than cloud radars as they are also present at airports to detect clouds, especially liquid layers. Operationally most ceilometers only provide cloud base height and cloud amount, but in principle all ceilometers observe the attenuated backscatter profile. This profile can be further processed to yield information on the boundary layer and the presence of aerosol, liquid, ice, and precipitation (Hogan et al., 2003; Morille et al., 2007; Münkel et al., 2007; Van Tricht et al., 2014; Kotthaus and Grimmond, 2018). Manufacturer-provided cloud base algorithms are typically not public and have been developed for aviation purposes based on decreased visibility. Cloud base height has also been derived from a microphysical point of view from the attenuated backscatter profile (e.g. Illingworth et al., 2007; Martucci et al., 2010; Van Tricht et al., 2014). Our goal is to increase the cloud information available from the ceilometer attenuated backscatter profile and combine this with surface radiation measurements.

Ceilometers are often operated in large networks (e.g. by national weather services; Illingworth et al., 2015), which are now being incorporated within harmonized pan-continental networks such as E-PROFILE (Illingworth et al., 2019), through which the profile is being recorded. Thus, implementing ceilometer methods for evaluating cloud and radiation model forecasts would be a beneficial addition to the more comprehensive but sparse cloud profiling.

Our aim is to understand how the forecast of low and mid-level clouds in an NWP model impacts the forecast of solar radiation at the surface. Moreover, our goal is a methodology that can be implemented rapidly at numerous sites with autonomous and robust instrumentation, i.e. combining ceilometer and solar radiation observations (Sect. 2) with single-level fields from NWP models ("single level" refers to surface fields and column-integrated fields). This requires accurate detection of liquid water clouds, precipitation, ice, and fog. In Sect. 3, we detail how we improved liquid cloud detection, and developed precipitation and fog identification algorithms, for ceilometers. In this study, we concentrated on evaluating the ECMWF IFS. Details on the model and the forecast cloud and solar radiation parameters investigated are described in Sect. 4. Since we are comparing point measurements from the ceilometer and ground-based solar radiation instruments with the single-level output from gridded model data, both observations and forecast model parameters require post-processing before model evaluation. This post-processing methodology is presented in Sect. 5 and would be applicable to a wide range of NWP models and at hundreds of observation sites globally. We use 4 years of cloud cover and solar radiation observations from Helsinki, Finland (Sect. 6), to investigate the skill of the IFS in forecasting clouds and radiation using our methodology (Sects. 7–9), whereby we explicitly examine how the skill in forecasting cloud is related to the solar radiation forecast error.

2 Ceilometer and solar radiation observations

A ceilometer is an active instrument, which sends very short light pulses produced by a laser into the atmosphere and detects the backscattered signal from aerosol particles, cloud droplets, and ice crystals. In this study we use a Vaisala CL51 ceilometer for observing clouds, which has a wavelength close to 910 nm. Operationally, the instrument reports cloud base heights and cloudiness values (oktas), but the internal algorithms do not determine cloud type, such as whether the cloud contains liquid or ice or both, and therefore we do not use these values. In addition to the standard cloud reporting, ceilometers can also provide the attenuated backscatter profile, from which it is possible to distinguish liquid layers, ice clouds, fog, and precipitation; we describe the algorithms developed for this in Sect. 3. In this study, the vertical range resolution of the ceilometer is 10 m, with attenuated backscatter profiles output every 15 s and a maximum range of 15 km. The calibration of the raw attenuated backscatter profiles is performed using the method of O'Connor et al. (2004), and the background noise is identified and removed based on the signal-to-noise ratio. The noise is calculated from the furthest range gates and assumed to be constant over the profile. The identification of high ice clouds is improved through temporal and spatial averaging to increase sensitivity; however, there are still challenges in identifying high ice clouds, especially during the day when the solar background noise is

high. Note that we take into account the ceilometer data post-processing methods recommended by Kotthaus et al. (2016).

The ceilometer is suited to the identification of liquid clouds and precipitation in the vertical profile; however, the measurement is usually limited to the lowest liquid cloud layer due to strong attenuation, and no information is available above this layer. Figure 1a shows an example of calibrated, background-noise-removed ceilometer attenuated backscatter profiles during 9 h at Helsinki, Finland, on 30 March 2016. A fog layer has been identified from 08:00 to 09:45 UTC with no information available above. Liquid cloud layers have been identified between 10:30–11:00 UTC (below 1 km) and 11:00–13:30 UTC (below 2.5 km), again with no information available above, except around 12:30 UTC when the liquid layer is dissipating. The signal is also attenuated in the case of heavy precipitation in which the ceilometer may not detect the cloud base above the precipitation layer. Precipitation, here in the form of ice, is visible in Fig. 1a at 10:00–10:30, 13:30–16:00, and after 16:30 UTC and does not reach the ground. Weak backscatter from aerosol in the boundary layer (orange colour) is visible when there is no precipitation, fog, or liquid layers close to the ground. Since the ceilometer reliably detects the first cloud layer, we can use the data to derive robust cloud cover quantities even though we cannot say if there is any more cloud above the first layer detected.

Solar radiation, specifically global horizontal irradiance (GHI), is measured with a Kipp & Zonen CM11 Secondary Standard pyranometer. Automated quality control has been applied by the Finnish Meteorological Institute (FMI) together with a visual check to ensure the data quality. The automated quality control is based on the Baseline Surface Radiation Network (BSRN) quality control procedure (Long and Shi, 2008) with small modifications to be more suitable for Finnish conditions (Rontu and Lindfors, 2018). GHI measurements are stored as 1 min averages in the FMI database.

3 Ceilometer algorithm development

3.1 Liquid layer identification improvements

In this study, we develop an algorithm to detect liquid cloud layers. The Cloudnet (Illingworth et al., 2007) approach for detecting the liquid cloud base is used as a starting point. The Cloudnet approach relies on the shape of the attenuated backscatter profiles, as it is known that the liquid droplets result in a high backscatter signal and the signal attenuates in the liquid layer (Fig. 1c). Thus, liquid layers display local peaks of stronger signal in the vertical profile of attenuated backscatter coefficient β. The Cloudnet approach searches for the lowest height range gate at which the attenuated backscatter value exceeds the given threshold ($\beta = 2 \times 10^{-5}\,\mathrm{m^{-1}\,sr^{-1}}$, representing liquid and called a pivot) and the signal is attenuated 250 m above the pivot value. If the signal attenuates above the pivot value, the cloud base is found below the pivot value based on the gradient in the β profile. Multiple liquid cloud bases are allowed in the Cloudnet method. This method is part of the Cloudnet approach for identifying "droplet bits" within the categorization process (Illingworth et al., 2007) and is described in detail here: http://www.met.rdg.ac.uk/~swrhgnrj/publications/categorization.pdf (last access: 1 November 2018), under the section "3.4.2 Droplet bit".

The Cloudnet approach is skilful in situations when there is no precipitation. During strong precipitation the attenuated backscatter coefficient may exceed the given threshold used in the Cloudnet droplet bit algorithm, even if stronger values representing the true liquid layer would be present above. Therefore, the cloud base may incorrectly be identified inside the precipitation layer below the true liquid cloud base (Fig. 2a). The liquid cloud base might not be always visible due to the attenuation of the signal in a heavy precipitation layer. We improved the method to enable reliable detection in all cases, including heavy precipitation.

The algorithm for finding liquid layers relies on the same principles as the Cloudnet approach. However, our approach for finding the strong β value (pivot), representing the liquid layer, differs. Our updated liquid layer identification relies more on the shape of the profile than an absolute threshold value and the fact that a liquid layer exhibits a strong peak in the attenuated backscatter profile. Therefore, the maximum of a localized peak value of β is found (not only the first value above a certain threshold) with the requirement that the magnitude of the local maximum exceeds the same threshold β value as in the Cloudnet approach. An additional requirement is that the peak width is not too broad with the maximum peak width at half-height being set to 150 m. This ensures that the identified peak is attenuating rapidly (O'Connor et al., 2004) rather than the relatively weak attenuation expected in precipitation so that threshold exceedance found in precipitation is not enough to trigger false liquid layer identification. The cloud base below the strong β value is found using the same method as for the Cloudnet droplet bit algorithm.

Visual validation of our updated algorithm is shown in Fig. 2, which confirms that liquid cloud layer identification during precipitation is more accurate. The Cloudnet processing suite will soon be updated with this new algorithm, which will also improve Cloudnet-derived products. This new algorithm can be used for other applications such as the identification of liquid layers for in-cloud icing detection for wind turbine operators and aviation.

3.2 Precipitation and fog identification

In addition to liquid layers, we require fog, precipitation, and ice cloud identification. The profiles in these conditions show particular characteristics (Fig. 1b–d). Precipitation, including ice (we assume that all ice is falling), is identified from

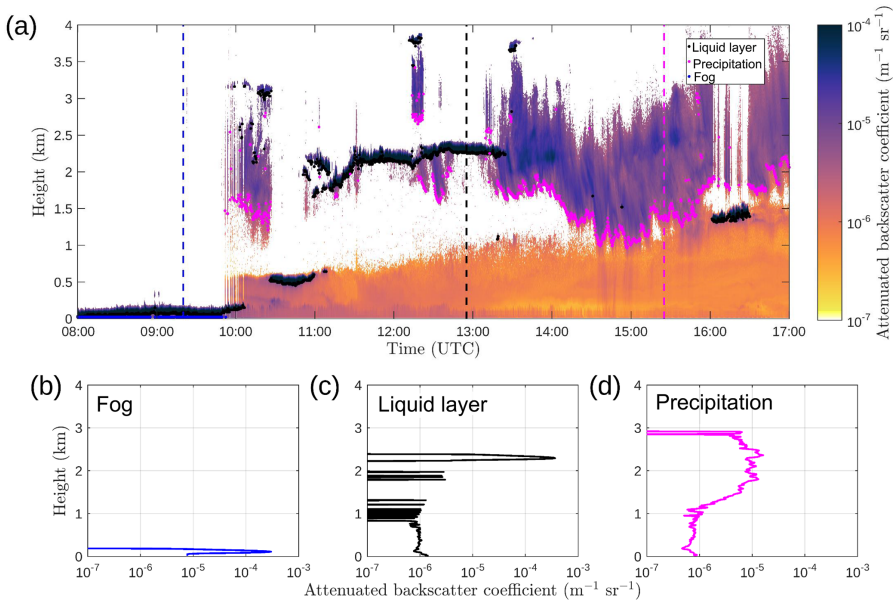

Figure 1. Time–height cross section of attenuated backscatter profiles from a Vaisala CL51 ceilometer on 30 March 2016 at Helsinki, Finland **(a)**. Overplotted are the results from our identification algorithms: fog (blue dots), liquid cloud base (black dots), and precipitation base (magenta dots). Sample attenuated backscatter profiles are also shown for fog **(b)**, liquid cloud layer **(c)**, and precipitation **(d)**. Dashed lines in **(a)** show the time when the profiles **(b)**–**(d)** are measured.

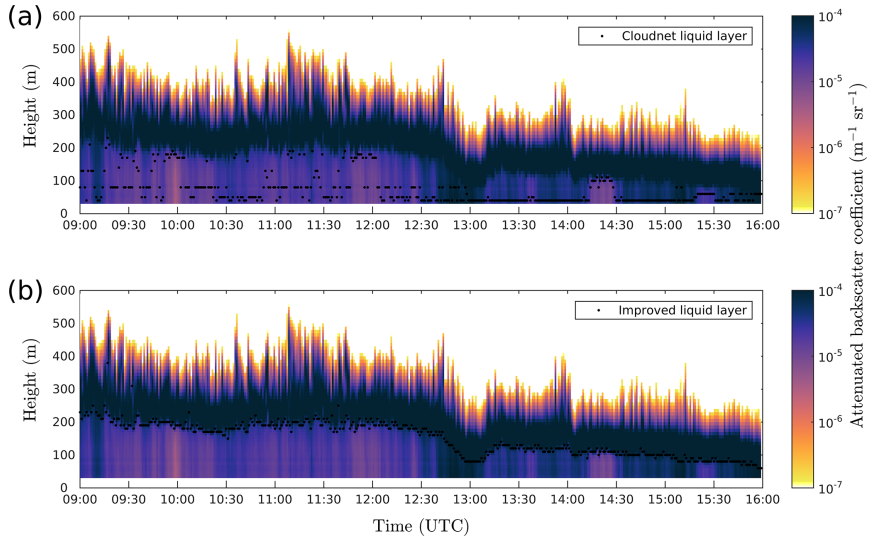

Figure 2. Time–height cross section of attenuated backscatter profiles from a Vaisala CL51 ceilometer on 27 October 2016 at Helsinki, Finland, with the Cloudnet approach **(a)** and with our updated algorithm **(b)** for obtaining liquid layer base. A major improvement is seen during precipitation events.

the shape of the attenuated backscatter profile (Fig. 1d). We identify the base of the precipitating layer, which in practice means the altitude at which the precipitation is either evaporating or reaching the ground. Typically, attenuated backscatter coefficient values are lower for precipitating rain and ice relative to liquid droplets. This is due to their much lower number concentrations even though the particle sizes are larger. The ceilometer signal is not attenuated as rapidly during precipitation and the ceilometer can "see" further into the precipitation. The precipitation algorithm uses a threshold value of $\beta = 3 \times 10^{-6}\,\mathrm{m^{-1}\,sr^{-1}}$, determined to be suitable in this study, together with a layer thickness greater than 350 m (i.e. the ceilometer backscatter signal is not attenuated within 350 m). We determined these thresholds by visual analysis. The layer base is simply the lowest range gate at which these two conditions are satisfied. Both precipitation and a liquid layer can be identified within the same profile.

Fog at the surface cannot always be identified using the liquid layer identification method, which relies on finding a local maximum in the β profile. An example of fog is given in Fig. 1b in which there are already high β values in the first range gate. Here we check the rate of the attenuation above the fog layer maximum as it may not be possible to define a peak. The threshold for fog is set as $\beta = 10^{-5}\,\mathrm{m^{-1}\,sr^{-1}}$, with a β value 250 m above the instrument of $\beta < 3 \times 10^{-7}\,\mathrm{m^{-1}\,sr^{-1}}$.

4 Model data

4.1 The Integrated Forecast System (IFS)

Forecasts produced by the Integrated Forecast System (IFS), run operationally by the European Centre for Medium-Range Weather Forecasts (ECMWF), are analysed in this study. The IFS is a global numerical weather prediction (NWP) system which includes observation processing and data assimilation in addition to the forecast system. The IFS is used to produce a range of different forecasts, from medium-range to seasonal predictions, and both deterministic and ensemble forecasts. In this study we only consider the high-resolution deterministic medium-range forecasts (referred to as HRES) which have a horizontal resolution of approximately 9 km and 137 vertical levels. The vertical grid spacing is non-uniform and below 15 km varies from 20 to 300 m with higher resolution closer to the ground. The temporal resolution of the model output is 1 h and forecasts up to 10 days in length are run every 12 h. A full description of the IFS can be found from ECMWF documentation: https://www.ecmwf.int/en/forecasts/documentation-and-support/changes-ecmwf-model/ifs-documentation (last access: 1 November 2018).

The IFS is under constant development and typically a new version becomes operational every 6–12 months. Therefore, unlike reanalysis, which is based on a static model system, the archived forecasts from the operational IFS reflect changes in the model. Although the aim of this paper is not to quantify how changes to the IFS affect the cloud and solar radiation forecasts, a brief overview of model updates is given here.

Several upgrades have been implemented into the IFS during the 4-year (2014–2017) data period that is used in this study (all are described in the IFS documentation: https://www.ecmwf.int/en/forecasts/documentation-and-support/changes-ecmwf-model/ifs-documentation.) A major upgrade occurred in March 2016 when the horizontal grid was changed from a cubic-reduced Gaussian grid to an octahedral-reduced Gaussian grid, resulting in an increase in horizontal resolution from 16 to 9 km. The cloud, convection, and radiation parameterization schemes strongly influence the forecast of clouds and radiation and all of these schemes have undergone updates during the 4-year period considered here. Notably, the radiation scheme was updated from the McRad scheme (Morcrette et al., 2008) to the scientifically improved and computationally cheaper ECRAD scheme (Hogan and Bozzo, 2016) in 2016. Aerosols also impact radiation forecasts and are represented in the IFS by a seasonally varying climatology. In July 2017 the aerosol climatology was updated to one derived from the aerosol model developed by the Copernicus Atmospheric Monitoring Service and coupled to the IFS (Bozzo et al., 2017). Note that in the current version of the IFS aerosol and clouds do not interact.

4.2 Model output used in this study

We use day-ahead forecasts, which have been initialized at 12:00 UTC the previous day and correspond to forecast hours t+12 to t+35, obtained from the closest land grid point to the measurement site 2.1 km away. Day-ahead forecasts are commonly used in the solar energy field for estimating daily production for the energy market. A list of the model variables we use is given in Table 1.

One goal is to develop simple and robust methods for evaluating the skill that the model has in forecasting clouds and solar radiation, which can be rapidly applied to numerous sites globally. Therefore, we take the single-level cloud forecast variables: low cloud cover (LCC) and medium cloud cover (MCC). These are defined in the IFS as follows: low is model levels with a pressure greater than 0.8 times the surface pressure (from the ground to approximately 2 km in altitude); medium encompasses model levels with a pressure between 0.45 and 0.8 times surface pressure (approximately 2–6 km). For IFS, the cloud layer overlap is also taken into account when calculating LCC and MCC, and the degree of randomness in cloud overlap is a function of the separation distance between layers (the greater the distance between layers, the more randomly overlapped they are; Hogan and Illingworth, 2000). For solar radiation forecasts, we use the surface solar radiation downward (SSRD), which is a single-

Table 1. ECMWF IFS model variables. Model-level fields have a vertical dimension. Single-level fields have no vertical dimension; this includes surface fields and column-integrated fields. Obtained via the Meteorological Archival and Retrieval System (MARS) at ECMWF using a grid resolution of 0.125°.

Variable	Short name	Unit	Variable type	Other
Low cloud cover	LCC	0–1	single level	instant
Medium cloud cover	MCC	0–1	single level	instant
Specific cloud liquid water content	CLWC	$\mathrm{kg\,kg^{-1}}$	model level	instant
Temperature	T	K	model level	instant
Pressure	PRES	Pa	model level	instant
Surface pressure	SP	Pa	single level	instant
Surface solar radiation downward	SSRD	$\mathrm{J\,m^{-2}}$	single level	cumulative
TOA incident solar radiation	TISR	$\mathrm{J\,m^{-2}}$	single level	cumulative

level parameter output hourly as an accumulated value (from the start of the forecast) in units of $\mathrm{J\,m^{-2}}$.

Other model variables are also downloaded for further calculation and for more detailed investigation of the sources of forecast error. Pressure (PRES) on model levels and surface pressure (SP) are used to determine the altitude levels for low and medium cloud cover classes for ceilometer data post-processing. Temperature (T) on model levels is used for classifying warm and cold (supercooled) liquid clouds. Specific cloud liquid water content on model levels (CLWC), provided as a mixing ratio, is used to calculate the total cloud liquid water path (LWP).

5 Methods for evaluating the model performance

Some further calculation is needed in order to evaluate the model output against the observations, as the variables obtained from the model and observations are not directly comparable. The forecast cloud cover is a single-level variable representing instantaneous values of column-integrated cloud coverage over an area (model grid of approximately 16×16 km before the resolution upgrade and 9×9 km area after the resolution upgrade) with hourly resolution. The ceilometer attenuated backscatter profile observations are point measurements with high temporal resolution (15 s), from which cloud occurrence can be derived. The forecast solar radiation is an accumulated value in $\mathrm{J\,m^{-2}}$ since the beginning of the forecast, whereas the observed GHI (in $\mathrm{W\,m^{-2}}$) is a point measurement averaged to 1 min resolution. Post-processing of both forecast and observations is required to obtain a comparable dataset, as discussed in the following subsections. After further post-processing, skill scores are then used to evaluate the cloud cover forecasts, and different error metrics are used to calculate the solar radiation forecast error.

In this study, we only consider daytime hours for model evaluation as our focus is on solar radiation forecasts. Therefore, hours with hourly-averaged GHI measurements less than $5\,\mathrm{W\,m^{-2}}$ are removed. For northern latitudes, this results in a range from 2 to $19\,\mathrm{h\,day^{-1}}$, depending on the season (short days in winter and long days in summer). Furthermore, it is required that the data availability of observations over each hour is at least 75 %; otherwise the hour is discarded from the analysis.

5.1 Post-processing of cloud cover forecasts and ceilometer observations

The difference arising from the fundamental differences in cloud information obtained from the model (grid value) and observations (point measurement) must be compensated for. As the clouds are advected over the measurement site, the temporal average of the point measurements of cloud occurrence is correlated with the cloud cover over an area. Therefore, averaging the ceilometer observations over a certain time window is assumed to correspond to cloud cover represented in grid space. The suitable averaging time window for cloud cover may not be easy to define; here 1 h averages are used as this is the temporal resolution of the model output. The horizontal resolution of the model is 16 km/9 km, and therefore 1 h averaging corresponds to advection speeds of 4.5 or $2.5\,\mathrm{m\,s^{-1}}$. However, we are aware that this averaging procedure may not always be appropriate for comparison and is kept in mind when analysing the results.

High and thin ice clouds are not reliably detected with ceilometers (see Sect. 2), and therefore we only consider clouds at low to medium altitudes in both the model and observations. We do not evaluate the model total cloud cover (TCC), as this contains contributions from high clouds.

The model variables LCC and MCC account for cloud within their relevant height ranges regardless of whether there is cloud in a lower level. In contrast, the ceilometer usually only detects the base of the first cloud layer. For example, the ceilometer may detect a cloud base to be below 2 km, hence defining it as low cloud, but the cloud may also contribute significantly to mid-level cloud cover, which is not captured by the ceilometer. In strong precipitation, the lidar signal may be sufficiently attenuated so that the liquid cloud base can no longer be detected above the precipitation. In

these cases, the bottom of the precipitation layer is treated as a cloud base, even though in reality the cloud producing the rain is at higher altitude. Thus, we combine low and medium cloud cover, rather than investigating them separately.

Cloud cover is estimated from the ceilometer data as follows: first, the attenuated backscatter profiles are averaged over 1 min before applying the algorithms described in Sect. 3. Then, liquid layers, precipitation (including ice clouds), and fog are identified for each 1 min profile. The forecast pressure on model levels is interpolated to the ceilometer range gate heights using the model height (ECMWF uses a terrain-following eta coordinate system). Cloud cover at each level (low and medium, defined in terms of pressure as for the model) is calculated as the percentage of cloud occurrence (occurrence of liquid cloud, precipitation or ice cloud, or fog) within each level over each hour. Finally, the observed cloud cover is the hourly sum of the observed low and medium cloud cover. Note that here the observed cloud cover is a summation since it is calculated from time series of independent columns for which only the first cloud layer contributes to the cloud cover calculation (the lowest layer).

The forecast LCC and MCC represent the fractional cloud cover (from 0 to 1) over the grid point, and combining these requires an assumed overlap factor. In this study we use the random overlap assumption, which may result in a slight overestimate (Hogan and Illingworth, 2000).

5.2 Post-processing of solar radiation forecasts and solar radiation observations

Forecast surface solar radiation (SSRD) is compared against the observed global horizontal irradiance (GHI). Values of SSRD require de-accumulating to hourly averages as the forecast solar radiation is an accumulated field from the beginning of the forecast and is transformed from $\mathrm{J\,m^{-2}}$ to $\mathrm{W\,m^{-2}}$. Observed 1 min averaged GHI measurements ($\mathrm{W\,m^{-2}}$) are averaged over 1 h for comparison. It should be noted that the model radiative transfer scheme is unlikely to completely account for the three-dimensional nature of radiative transfer as experienced by the observations.

5.3 Skill scores for cloud cover forecasts and error metrics for solar radiation forecast error

Cloud cover forecasts are evaluated with 2-D histograms and skill scores. We use the mean absolute error skill score (MAESS; Hogan et al., 2009) and mean squared error skill score (MSESS; Murphy, 1988), which compare the occurrence of a cloud separately in observations and in forecasts, and take into account the magnitude of the difference. MAESS uses the absolute difference between the forecast and observed value, and MSESS uses the squared difference, which for two forecasts with the same absolute error will penalize the forecast with one or two large errors more than the forecast with many small errors. The skill scores are based on the contingency table (Table A1 in Appendix A1), in which the occurrence of hits, false alarms, misses, and correct negative values by a given cloud cover threshold are calculated. For example, a hit occurs when both forecast and observed cloud cover are above a given cloud cover threshold. Here, the threshold for cloud cover is set to 0.05, following the method used by Hogan et al. (2009). Therefore, a hit means that some amount of cloud is both forecast and observed; however, a hit does not yet imply a perfect forecast. For both MAESS and MSESS, the skill of a random forecast is 0 and a perfect forecast 1. The equation for MAESS and MSESS is given in Appendix A1.

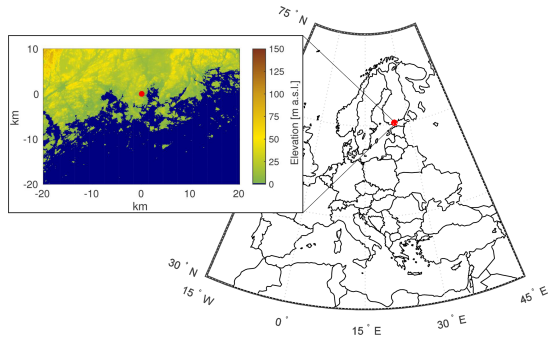

Figure 3. Measurement site at Helsinki, Finland (60.204° N, 24.961° E).

The error metrics mean absolute error (MAE), mean absolute percentage error (MAPE), mean error or bias (ME), and root mean square error (RMSE) are used to evaluate the solar radiation forecast errors. These error metrics are defined in Appendix A2. MAE, RMSE, and ME are absolute error metrics and result in forecast error in $\mathrm{W\,m^{-2}}$, whereas MAPE is a relative error given in percent. ME is the only error metric that shows the sign of the error. A positive bias is seen when the model overestimates the incoming surface solar radiation, whereas a negative bias is when the model underestimates the incoming solar radiation.

6 Site characteristics and cloud and radiation climatology

The measurement site is located on the roof of FMI in Helsinki, Finland (60.204° N, 24.961° E; Fig. 3, measurements at 26 m above sea level), located less than 10 km from the coastline of the Gulf of Finland. Coastal effects, such as sea breezes, are common. There are no large variations in topography around the site.

We investigate the cloudiness and solar resource at this site using 4 years of ceilometer observations and solar radiation measurements. There is an annual variation in the

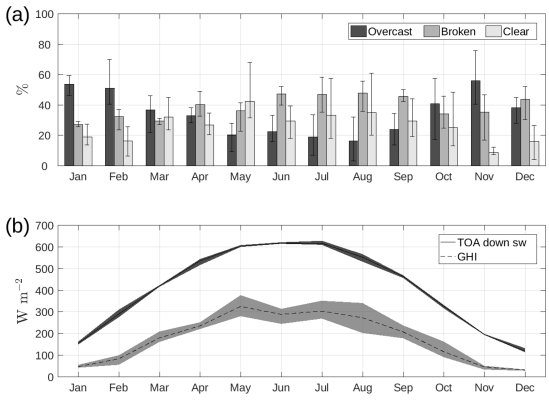

Figure 4. Relative occurrence of overcast, broken cloud, and clear-sky conditions **(a)**. Bars show yearly variation (min, max). Annual variation in observed GHI and forecast top-of-atmosphere downwelling shortwave radiation **(b)**. Shaded area represents the year-to-year variation in monthly means.

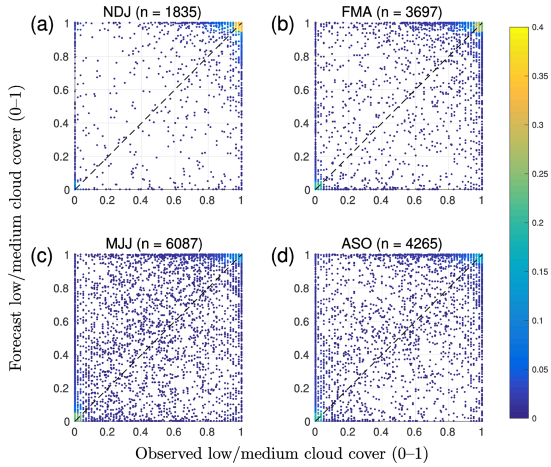

Figure 5. Seasonal normalized density scatter plots of observed and forecast cloud cover (total counts for each season are given in the titles). Seasons are defined based on the annual distribution of incoming solar radiation: **(a)** winter (November to January), **(b)** spring (February to April), **(c)** summer (May to July), and **(d)** autumn (August to October).

observed cloudiness at the site (Fig. 4a) with overcast conditions (cloud cover ≥ 0.95) being more common in winter and less common in summer. In contrast, broken cloud ($0.05 <$ cloud cover < 0.95) and clear (cloud cover ≤ 0.05) conditions are most common in summer and least common in winter. The variation in cloudiness is quite high from year to year, especially in summer, but in winter the most probable sky condition contains cloud.

In addition to the observed annual variation of cloudiness, the observed annual variation of incoming solar radiation is strongly influenced by the northern location of the site (60° N). Due to the change in the solar zenith angle, the length of the shortest day of the year (winter solstice on 21 or 22 December) is less than 6 h and the length of the longest day (summer solstice between 20 and 22 June) is almost 19 h. The amount of solar radiation at the top of the atmosphere is much higher during summer when the solar zenith angle is also much higher (Fig. 4b, solid line). This signal is also clear in the amount of solar radiation reaching the ground, the measured GHI (Fig. 4b, dashed line), which is dependent on both the incoming solar radiation at the top of atmosphere and the attenuation of the downward flux due to clouds, aerosols, and atmospheric gases. The year-to-year variation in the monthly mean of measured GHI is much greater during summer months (lighter shaded area in Fig. 4b), with variations reaching 140 W m^{-2} in August, which is larger than the monthly mean GHI during winter months.

To investigate the seasonal variation, we define seasons based on the annual variation in the solar resource (Fig. 4b). The summer season is defined as May to July when the solar resource is at a maximum, and winter is defined as November to January when the solar resource is at a minimum (spring is February to April, autumn is August to October).

7 Forecast skill in predicting clouds and radiation

7.1 How well are clouds forecast?

We now investigate how well the IFS forecasts clouds over our site in Helsinki, Finland. Since we are interested in the solar resource we only evaluate time steps in which the hourly-averaged observed GHI is greater than 5 W m^{-2} to link the skill in forecasting clouds to the skill in forecasting radiation (Sect. 7.3).

In Fig. 5 we compare the observed and forecast cloud cover for each season. For a perfect forecast, all values would lie on the diagonal (dashed line) in each scatter plot. For all seasons, the majority of cloud cover values are concentrated around clear conditions (pair 0; 0) and overcast conditions (pair 1; 1) for both observations and forecasts. This suggests that not only are clear and overcast conditions the most commonly observed, but also most skilfully forecast in all seasons. During winter the vast majority of cloud cover observations and forecasts are at (or close to) overcast (Fig. 5a). Clear-sky conditions are more common in other seasons (both observations and model). The large spread for both observed and forecast cloud cover values between 0.1 and 0.9 indicates that partly cloudy conditions are challenging for the IFS to correctly predict. However, these cases are not as common as clear and overcast cases, which is a result of observed and forecast cloud cover distributions being strongly U-shaped for typical NWP model grid sizes (Hogan et al., 2009; Mittermaier, 2012; Morcrette et al., 2014). It is

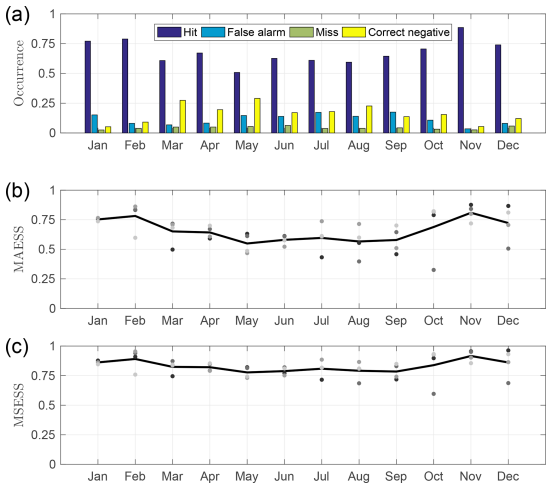

Figure 6. Relative occurrence of elements in the contingency table (hit, false alarm, miss, and correct negative) for each month with a cloud cover threshold of 0.05 **(a)**. Monthly mean skill scores for cloud cover: MAESS **(b)** and MSESS **(c)**, individual monthly mean for each year (dots), and 4-year average (line).

also notable that, during all seasons, there are values on the boundaries of the scatter plot away from the diagonal, for example, where the model is incorrectly forecasting clear sky during cloudy conditions or overcast conditions during clear or broken skies. Summer and autumn seasons (Fig. 5c, d) display more broken cloud conditions, as also seen in Fig. 4a, when the solar resource is high (Fig. 4b).

Skill scores represent the model's ability to forecast a given variable. To calculate skill scores, we generate a contingency table for cloud cover. This requires a binary forecast so we use a threshold cloud cover value of 0.05 as in Hogan et al. (2009) to define the presence of cloud: a hit is cloud observed and forecast; a false alarm is cloud not observed but forecast; a miss is cloud observed but not forecast; and a correct negative is cloud not observed or forecast.

The annual relative occurrences of contingency table elements (hit, false alarm, miss, correct negative) are shown in Fig. 6a. During all months, hit has the highest relative occurrence (mean 68 %), indicating that the model usually contains some low or mid-level cloud when cloud is also observed at these levels. The hit occurrence is greatest between October and February when overcast conditions are also most common (Fig. 4a). Note that a hit requires that both observations and model have some cloud, but it does not necessarily represent a perfect forecast. Similarly, the relative occurrence of correct negative is highest during spring and summer months. False alarms are most common in summer and autumn when their relative occurrence reaches 17 %. The relative occurrence of missed clouds is low (mean 4 %) for all months and there is no clear seasonal cycle.

Skill scores are then generated from the contingency table; we use MAESS and MSESS as these take into account the magnitude of the difference between the observed and forecast cloud cover (Fig. 6b, c). MAESS and MSESS both show annual variation, being highest during winter months and lowest during summer months. This information is important, especially for solar energy purposes, as it shows that clouds are forecast less skilfully in summer, which is when the solar resource is greatest. There are also notable variations in skill scores from year to year, especially in October and December. MSESS is greater than MAESS, especially during summer when more broken cloud conditions are expected.

7.2 How well is solar radiation forecast?

As expected, there is a large seasonal variation in observed GHI: up to 900 $\mathrm{W\,m^{-2}}$ in summer (Fig. 7c) and less than 300 $\mathrm{W\,m^{-2}}$ in winter (Fig. 7a). The absolute error in the solar radiation forecast can therefore potentially be much higher in summer and is evident in the potential range of scatter between observed GHI and forecast GHI for each season (Fig. 7). The forecast of solar radiation is usually overestimated in all seasons (Fig. 8), especially for low irradiance values for which the positive bias is more obvious. Solar radiation forecast MAE (Fig. 8a, solid line) is greater in summer than in winter, as is the year-to-year variation in monthly absolute errors (shaded area in Fig. 8a). There is no clear seasonal cycle in the variation in the relative error (MAPE) from year to year; however, MAPE itself peaks in February and November.

The mean error (ME) in the solar radiation forecast is positive when the model overestimates solar radiation at the surface. Figure 8b shows separate calculations of the monthly mean positive (red) and negative (blue) bias in forecast GHI. Throughout the year, the positive bias (both absolute and relative) is greater than the negative bias, and thus the model overestimates solar radiation more than it underestimates. The year-to-year variation in relative positive bias is also larger than the relative negative bias. For example, the relative positive bias in solar radiation forecast ranges between 50 % and 125 %, whereas the relative negative bias is rather constant at around 25 %. Overestimates are also more common than underestimates (not shown). The result is an overall positive bias in forecast GHI. Both positive bias metrics (relative and absolute) show the same seasonal response as the corresponding MAE/MAPE metric and the negative bias metric shows the same summer enhancement as the positive bias but with the opposite sign.

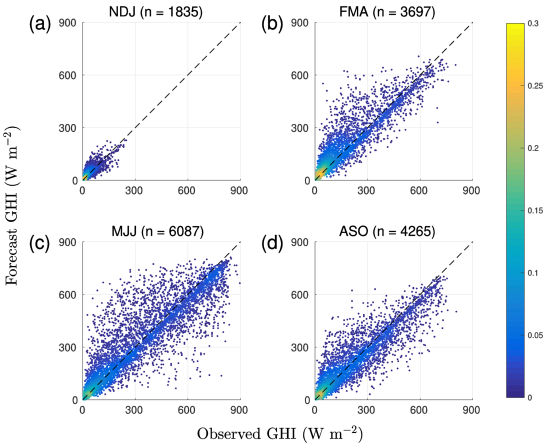

Figure 7. Seasonal normalized density scatter plots of observed and forecast GHI (total counts for each season are given in the titles). Seasons are defined based on the annual distribution of incoming solar radiation: **(a)** winter (November to January), **(b)** spring (February to April), **(c)** summer (May to July), and **(d)** autumn (August to October).

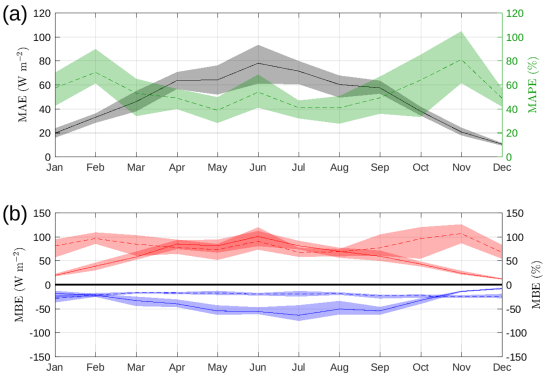

Figure 8. Monthly MAE (black solid line) and MAPE (green dashed line) in solar radiation forecast **(a)**. Monthly absolute (solid line) and relative (dashed line) ME **(b)**. Positive bias (red) and negative bias (blue) are shown separately; shaded area represents year-to-year variation.

7.3 How do errors in cloud cover impact the solar radiation forecast?

Assuming the correct representation of radiative transfer in the atmosphere, with only the forecast of cloud impacting the solar radiation forecast at the surface (no change in aerosol or humidity), then an increase in forecast cloud cover would be expected to result in a reduction in the amount of forecast solar radiation. However, the amount of cloud may be

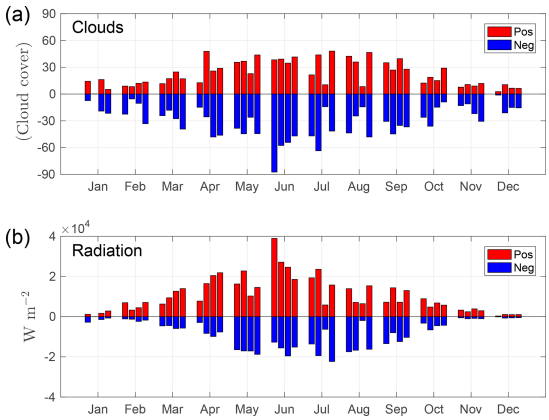

Figure 9. Monthly accumulated positive (red) and negative (blue) bias in cloud cover forecast **(a)** and solar radiation forecast **(b)**. The four bars in each month represent individual years (2014–2017).

correctly forecast, but not the cloud properties. Since cloud properties are directly responsible for the cloud radiative effect, both cloud amount and properties should be correctly forecast in order to obtain a reliable solar radiation forecast.

Figure 9 shows the annual cycle of accumulated positive and negative bias in the cloud cover forecast and solar radiation forecast. It can be seen that months with a large accumulated negative bias in cloud cover forecasts (e.g. June 2014) show a notably large accumulated positive bias in the solar radiation forecast. However, not all months show a clear correlation between a negative bias in the cloud cover forecast and a positive bias in the solar radiation forecast. This is most probably due to compensating effects whereby, for example, the cloud cover forecast could be overestimated (positive bias in cloud cover) but the liquid water content forecast is underestimated (which would result in positive bias in solar radiation forecasts).

To investigate how well the forecast cloud cover corresponds to the observed cloud cover, the counts of hourly observed and forecast cloud cover values are paired together in 2-D histograms (Fig. 10a). For perfect forecasts, all counts would lie on the diagonal. Figure 10a shows that there are many correctly forecast situations for clear sky (0; 0) and overcast (1; 1). However, it is clear that there are many values on the boundaries, which means that cloud is either observed and not forecast (miss) or cloud is forecast but not observed (false alarm). At 1 h resolution, 47 % of the total number of counts is above the diagonal, and thus the forecast cloud cover is overestimated on average. The forecast underestimates cloud cover 34 % of the time. Note that changing the overlap assumption from random to maximum when calculating the combined cloud cover (LCC + MCC) changes these values by 3 %.

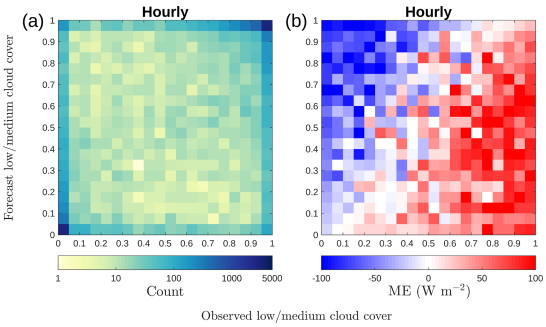

Figure 10. 2-D histogram of observed and forecast cloud cover **(a)**, with colours representing counts on a logarithmic scale, and ME in solar radiation forecast **(b)** for each cloud cover pair in **(a)**.

The solar radiation forecast ME for concurrent pairs of cloud cover values in Fig. 10a is presented in Fig. 10b. ME values below the diagonal, for which the forecast cloud cover is underestimated, are mostly positive; similarly, ME values above the diagonal are mostly negative, and the forecast cloud cover is overestimated. Note that the change from positive to negative ME does not quite follow the diagonal, with minimal bias appearing to follow a line from $(0.1; 0)$ to $(0.8; 1)$; i.e. observed cloud cover greater than 0.9 shows a positive solar radiation forecast ME ($27\,\mathrm{W\,m^{-2}}$) and observed cloud cover less than 0.1 shows negative ME ($-16\,\mathrm{W\,m^{-2}}$). This negative bias during clear-sky situations over Helsinki was also observed by Rontu and Lindfors (2018) and is most likely due to the aerosol climatology implemented in the model having too much aerosol. Another possible source of negative bias during clear-sky situations would be too much water vapour in the atmosphere. There are earlier studies showing similar results elsewhere (Ahlgrimm and Forbes, 2012; Frank et al., 2018). Overcast situations occur more frequently than clear sky (23 % of the time), resulting in the overall positive bias in the solar radiation forecast.

8 Impact of temporal averaging

Forecasting individual clouds in the right place at the right time is challenging and here we investigate whether temporal averaging improves the cloud forecast and therefore the radiation forecast. Different averaging windows (3-hourly, 6-hourly, 12-hourly, daily) are used in preparing the data for evaluation in the same manner as for Fig. 10a and the results for selected averaging windows are shown in Fig. 11a–c. The agreement between observed and forecast cloud cover improves with increasing averaging windows, and the number of cases of extreme misses and false alarms (corners $(1; 0)$ and $(0; 1)$) decreases.

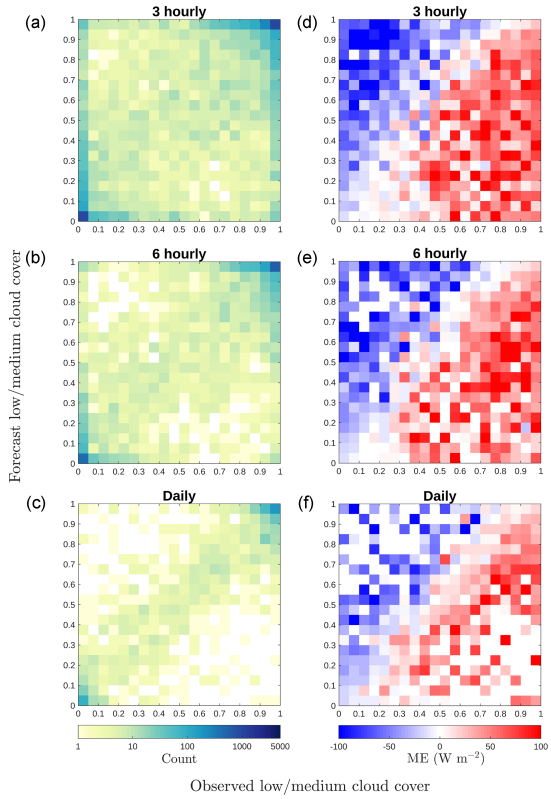

Figure 11. Same plots as Fig. 10, except for different averaging time windows (3 hourly, 6 hourly, and daily). 2-D histograms of observed and forecast cloud cover **(a–c)**, with colours representing counts on a logarithmic scale, and ME in solar radiation forecast **(d–f)** for each cloud cover pair in **(a–c)**.

When calculated separately, the magnitudes of the positive and negative solar radiation forecast biases for concurrent pairs of cloud cover values decrease with increasing averaging time. The mean positive bias decreases from $65\,\mathrm{W\,m^{-2}}$ when averaging over 1 h to $35\,\mathrm{W\,m^{-2}}$ when averaging over 1 day, and the mean negative bias reduces from -46 to $-27\,\mathrm{W\,m^{-2}}$. The overall bias remains around $8\,\mathrm{W\,m^{-2}}$. Increasing the averaging window does not alter the pattern in which the change from positive to negative ME is away from the diagonal. The negative bias in clear-sky conditions and positive bias in overcast conditions are still present, suggesting that the bias is likely to be due to cloud properties rather than the cloud presence.

Figure 12 summarizes the impact of temporal averaging on the skill in forecasting cloud cover and the error in forecasting solar radiation, with skill clearly increasing and error decreasing as the averaging window is lengthened. Extreme misses and false alarms for cloud cover are reduced, and for

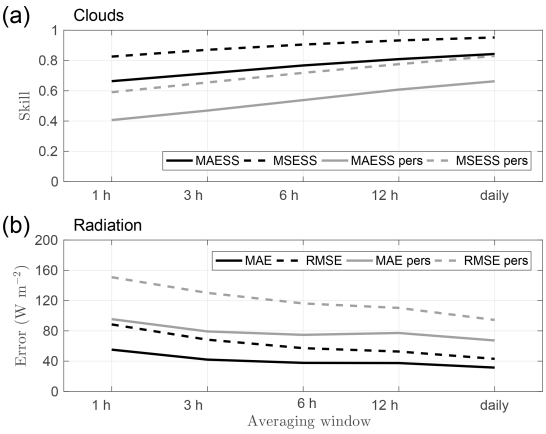

Figure 12. Cloud cover forecast skill scores **(a)** and error in solar radiation forecast **(b)** for different averaging time windows, including persistence forecasts (grey lines). Note the non-linear x axis.

GHI MAE, the individual absolute errors are reduced with temporal averaging. Persistence forecasts were also investigated; a persistence forecast uses the hourly forecast values from the day before. The skill for the cloud cover persistence forecast also increases with increasing temporal averaging, as does the reduction of error in the persistence GHI forecast; however, these are not as good as the actual forecasts at this location.

9 Overcast analysis

Figures 10 and 11 show a positive bias in the solar radiation forecast, even when overcast conditions are correctly forecast, for all averaging windows. As the cloud amount is correctly forecast, this suggests that the bias must be due to cloud properties. We investigate the forecast cloud base temperature and cloud liquid water path (LWP). Previous studies have shown that clouds containing supercooled liquid ($T < 0\,°\mathrm{C}$) are poorly forecast (Forbes and Ahlgrimm, 2014; Barrett et al., 2017), and LWP is one parameter that contains information on the amount of liquid water in a cloud, directly impacting how much solar radiation is transmitted through the cloud.

We consider correctly forecast overcast cases (observed and forecast cloud cover > 0.9) containing liquid. The clouds are classified as warm or cold (supercooled), depending on their cloud base temperature, using the temperature profile from the IFS as no observed temperature profiles are available. We then bin the clouds based on their forecast cloud LWP obtained by integrating the forecast cloud liquid water content (CLWC; Table 1). We selected three bins representing relatively high (LWP $> 0.2\,\mathrm{kg\,m^{-2}}$), moderate ($0.2\,\mathrm{kg\,m^{-2}} \geq$ LWP $\geq 0.05\,\mathrm{kg\,m^{-2}}$), and low (LWP $< 0.05\,\mathrm{kg\,m^{-2}}$) cloud liquid water content. These values were selected based on the range of optical depths that would be expected for each LWP range bin. Unfortunately, there was no observed LWP available for this measurement site.

Figure 13 shows that the positive bias in the solar radiation forecast increases with decreasing LWP. Note that the response is similar for both warm and cold liquid clouds. For warm clouds, the ME in GHI increases from $16\,\mathrm{W\,m^{-2}}$ for clouds with high LWP to $70\,\mathrm{W\,m^{-2}}$ for clouds with low LWP. For cold clouds, the ME in GHI increases from $15\,\mathrm{W\,m^{-2}}$ for clouds with high LWP to $36\,\mathrm{W\,m^{-2}}$ for clouds with low LWP. This suggests that either forecast clouds do not have enough LWP or that the optical properties of clouds with low LWP are not properly modelled. The first conclusion, that forecast clouds do not have enough LWP, is consistent with the findings of Ahlgrimm and Forbes (2012). They found a positive radiation bias in ECMWF IFS for overcast situations with low cloud at the Atmospheric Radiation Measurement site in the Southern Great Plains. Furthermore, they found that IFS overestimates the occurrence of clouds with low LWP and underestimates the number of clouds with high LWP, which also results in a positive bias in solar radiation forecasts. Challenges in correctly modelling supercooled liquid clouds have previously been reported, but our results suggest that the issue of a positive bias in GHI is more pronounced for warm clouds and not just an issue for supercooled liquid clouds.

Also of interest is that the relative bias in GHI is constant across a wide range of GHI values. This implies that a simple LWP-dependent correction factor could be applied to the GHI forecast to remove the bias.

10 Conclusions

We have used ceilometer and solar radiation measurements to evaluate the cloud cover and solar radiation forecasts in the ECMWF operational IFS model over Helsinki, Finland. To obtain reliable cloud cover information from the ceilometer attenuated backscatter profiles, we took the Cloudnet liquid bit algorithm (Illingworth et al., 2007) as a starting point, updated the liquid cloud detection, especially during precipitation events, and developed additional algorithms for discriminating fog, precipitation, and ice. The new algorithms are widely applicable for both operational use and research, e.g. in-cloud icing detection for the wind energy industry and for aviation. The updated algorithm will also be implemented operationally throughout the ACTRIS–Cloudnet network.

Over Helsinki, both observed and forecast cloud cover distributions are U-shaped, indicating that most of the time the sky is either clear or overcast. Overcast conditions are most common in winter, whereas clear (and broken cloud) conditions are more common in summer. Cloud cover is better forecast in winter; however, this is when the solar resource is lower. The measured GHI is strongly influenced by the an-

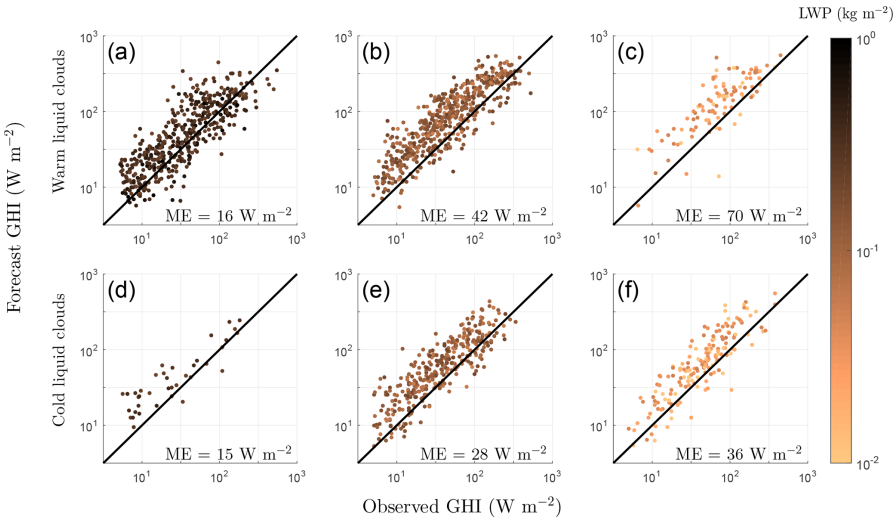

Figure 13. Solar radiation forecast ME versus forecast LWP for different LWP and temperature classes: warm clouds **(a)–(c)** with cloud base temperature above 0 °C and cold (supercooled) clouds **(d)–(f)** with cloud base temperature less than 0 °C; LWP $> 0.2\,\mathrm{kg\,m^{-2}}$ **(a)**, **(d)**; $0.2\,\mathrm{kg\,m^{-2}} \geq \mathrm{LWP} \geq 0.05\,\mathrm{kg\,m^{-2}}$ **(b)**, **(e)**; LWP $< 0.05\,\mathrm{kg\,m^{-2}}$ **(c)**, **(f)**. Colour scale indicates LWP values.

nual solar resource characterized by the northern latitude and annual variations in cloudiness; the absolute solar radiation forecast error tracks GHI, but the relative error is more or less constant throughout the year.

As expected, the bias in forecast GHI is negative when the model overestimates cloud cover (incoming solar radiation is underestimated by the model) and positive when the model underestimates cloud cover. Temporal averaging of the data improves the cloud cover forecasts and decreases the solar radiation forecast errors, as was shown by Hogan et al. (2009). The mean overall bias in the GHI forecast is positive ($8\,\mathrm{W\,m^{-2}}$). However, there is a negative bias in forecast GHI for correctly forecast clear cases and a positive bias in correctly forecast overcast cases. A mean overall positive bias would be expected if, on average, the forecast cloud cover was being underestimated, but the forecast cloud cover is usually overestimated on average. This is because the positive GHI bias for the very frequent overcast situations dominates the overall bias. This positive bias occurs for cases in which the model cloud has low values of LWP, and we attribute this bias to the model having LWP values that are too low or the model optical properties for clouds with low LWP being incorrect.

In the future, these methods and analysis can be extended to hundreds of sites across Europe which are now producing ceilometer attenuated backscatter profiles. This analysis will also be performed at Cloudnet stations, which have the advantage in that they have observations of LWP, together with full cloud profiling, enabling the source of the positive bias in clouds with low LWP to be investigated further.

Data availability. The data used in this paper are available on request from FMI (ewan.oconnor@fmi.fi).

Table A1. Contingency table for skill score calculation. Total number of counts, $n = a+b+c+d$, where a, b, c, and d are the number of counts for each situation.

	Observed cloud cover > 0.05	Observed cloud cover ≤ 0.05
Forecast cloud cover > 0.05	a = Hit	b = False alarm
Forecast cloud cover ≤ 0.05	c = Miss	d = Correct negative

Appendix A: Skill scores and error metrics

A1 Skill score calculation

The skill scores in this study are calculated using the generalized skill score equation (Hogan et al., 2009), which for MAESS and MSESS can be simplified to

$$S = 1 - \frac{x}{x_\mathrm{r}}, \tag{A1}$$

where $x = (\mathrm{frc} - \mathrm{obs})^2$ for MSESS and $x = |\mathrm{frc} - \mathrm{obs}|$ for MAESS, and the values for the random forecast, x_r, are calculated from elements of the contingency table $x_\mathrm{r} = \frac{a+b}{n} \cdot \frac{a+c}{n} + \frac{d+c}{n} \cdot \frac{d+b}{n}$ for both MSESS and MAESS. The values obs and frc refer to the observed and forecast values of the variable of interest, e.g. cloud cover.

A2 Error metrics

$$\mathrm{MAE} = \frac{1}{n}\sum_{t=1}^{n} |\mathrm{frc} - \mathrm{obs}|, \tag{A2}$$

$$\mathrm{MAPE} = \frac{1}{n}\sum_{t=1}^{n} \frac{\mathrm{frc} - \mathrm{obs}}{\mathrm{obs}} \cdot 100, \tag{A3}$$

$$\mathrm{ME} = \frac{1}{n}\sum_{t=1}^{n} (\mathrm{frc} - \mathrm{obs}), \tag{A4}$$

$$\mathrm{RMSE} = \sqrt{\frac{1}{n}\sum_{t=1}^{n} (\mathrm{frc} - \mathrm{obs})^2}. \tag{A5}$$

Author contributions. All authors conceived and designed the analysis. MT and EOC obtained the data, and MT performed the analysis. MT wrote the paper with input from all authors. EOC and VS conceived the study and were in charge of overall direction and planning.

Competing interests. The authors declare that they have no conflict of interest.

Acknowledgements. This work was supported by the Maj and Tor Nessling Foundation (grant 201700032) and by the European Commission via project ACTRIS2 (grant agreement no. 654109). Victoria A. Sinclair is funded by the Academy of Finland (project no. 307331). We acknowledge ECMWF for providing model output from IFS and FMI for providing ceilometer and solar radiation observations.

Edited by: Jui-Yuan Christine Chiu
Reviewed by: three anonymous referees

References

Ahlgrimm, M. and Forbes, R.: The impact of low clouds on surface shortwave radiation in the ECMWF model, Mon. Weather Rev., 140, 3783–3794, https://doi.org/10.1175/MWR-D-11-00316.1, 2012.

Barrett, A. I., Hogan, R. J., and Forbes, R. M.: Why are mixed-phase altocumulus clouds poorly predicted by large-scale models? Part 1. Physical processes, J. Geophys. Res.-Atmos., 122, 9903–9926, https://doi.org/10.1002/2016JD026321, 2017.

Boilley, A. and Wald, L.: Comparison between meteorological reanalyses from ERA-Interim and MERRA and measurements of daily solar irradiation at surface, Renew. Energ., 75, 135–143, https://doi.org/10.1016/j.renene.2014.09.042, 2015.

Bozzo, A., Remy, S., Benedetti, A., Flemming, J., Bechtold, P., Rodwell, M., and Morcrette, J.-J.: Implementation of a CAMS-based aerosol climatology in the IFS, ECMWF, Technical Memorandum, 801, https://doi.org/10.21957/84ya94mls, 2017.

Forbes, R. M. and Ahlgrimm, M.: On the representation of high-latitude boundary layer mixed-phase cloud in the ECMWF global model, Mon. Weather Rev., 142, 3425–3445, https://doi.org/10.1175/MWR-D-13-00325.1, 2014.

Frank, C. W., Wahl, S., Keller, J. D., Pospichal, B., Hense, A., and Crewell, S.: Bias correction of a novel European reanalysis data set for solar energy applications, Sol. Energy, 164, 12–24, https://doi.org/10.1016/j.solener.2018.02.012, 2018.

Hogan, R. and Bozzo, A.: ECRAD: A new radiation scheme for the IFS, ECMWF, Technical Memorandum, 787, https://doi.org/10.21957/whntqkfdz, 2016.

Hogan, R. J. and Illingworth, A. J.: Deriving cloud overlap statistics from radar, Q. J. Roy. Meteorol. Soc., 126, 2903–2909, https://doi.org/10.1002/qj.49712656914, 2000.

Hogan, R. J., Illingworth, A. J., O'connor, E. J., and Baptista, J. P. V. P.: Characteristics of mixed-phase clouds. II: A climatology from ground-based lidar, Q. J. Roy. Meteorol. Soc., 129, 2117–2134, https://doi.org/10.1256/qj.01.209, 2003.

Hogan, R. J., O'Connor, E. J., and Illingworth, A. J.: Verification of cloud–fraction forecasts, Q. J. Roy. Meteorol. Soc., 135, 1494–1511, https://doi.org/10.1002/qj.481, 2009.

Illingworth, A. J., Hogan, R. J., O'Connor, E., Bouniol, D., Brooks, M. E., Delanoé, J., Donovan, D. P., Eastment, J. D., Gaussiat, N., Goddard, J. W. F., Haeffelin, M., Baltink, H. K., Krasnov, O. A., Pelon, J., Piriou, J.-M., Protat, A., Russchenberg, H. W. J., Seifert, A., Tompkins, A. M., van Zadelhoff, G.-J., Vinit, F., Willén, U., Wilson, D. R., and Wrench, C. L.: Cloudnet, B. Am. Meteor. Soc., 88, 883–898, https://doi.org/10.1175/BAMS-88-6-883, 2007.

Illingworth, A. J., Cimini, D., Gaffard, C., Haeffelin, M., Lehmann, V., Löhnert, U., O'Connor, E. J., and Ruffieux, D.: Exploiting existing ground-based remote sensing networks to improve high-resolution weather forecasts, B. Am. Meteor. Soc., 96, 2107–2125, https://doi.org/10.1175/BAMS-D-13-00283.1, 2015.

Illingworth, A. J., Cimini, D., Haefele, A., Haeffelin, M., Hervo, M., Kotthaus, S., Löhnert, U., Martinet, P., Mattis, I., O'Connor, E. J., and Potthast, R.: How can existing ground-based profiling instruments improve European weather forecasts?, B. Am. Meteor. Soc., https://doi.org/10.1175/BAMS-D-17-0231.1, 2019.

Jia, B., Xie, Z., Dai, A., Shi, C., and Chen, F.: Evaluation of satellite and reanalysis products of downward surface solar radiation over East Asia: Spatial and seasonal variations, J. Geophys. Res.-Atmos., 118, 3431–3446, https://doi.org/10.1002/jgrd.50353, 2013.

Kleissl, J.: Solar energy forecasting and resource assessment, Academic Press, 1–462, 2013.

Kotthaus, S. and Grimmond, C. S. B.: Atmospheric boundary-layer characteristics from ceilometer measurements. Part 1: A new method to track mixed layer height and classify clouds, Q. J. Roy. Meteorol. Soc., 144, 1525–1538, https://doi.org/10.1002/qj.3299, 2018.

Kotthaus, S., O'Connor, E., Münkel, C., Charlton-Perez, C., Haeffelin, M., Gabey, A. M., and Grimmond, C. S. B.: Recommendations for processing atmospheric attenuated backscatter profiles from Vaisala CL31 ceilometers, Atmos. Meas. Tech., 9, 3769–3791, https://doi.org/10.5194/amt-9-3769-2016, 2016.

Long, C. N. and Shi, Y.: An automated quality assessment and control algorithm for surface radiation measurements, Open Atmos. Sci. J., 2, 23–37, https://doi.org/10.2174/1874282300802010023, 2008.

López, G. and Batlles, F. J.: Estimating solar radiation from MODIS data, Energy Proced., 49, 2362–2369, https://doi.org/10.1016/j.egypro.2014.03.250, 2014.

Martucci, G., Milroy, C., and O'Dowd, C. D.: Detection of cloud-base height using jenoptik CHM15K and Vaisala CL31 ceilometers, J. Atmos. Ocean. Tech., 27, 305–318, https://doi.org/10.1175/2009JTECHA1326.1, 2010.

Mather, J. H. and Voyles, J. W.: The Arm climate research facility: A review of structure and capabilities, B. Am. Meteor. Soc., 94, 377–392, https://doi.org/10.1175/BAMS-D-11-00218.1, 2013.

Mittermaier, M.: A critical assessment of surface cloud observations and their use for verifying cloud forecasts, Q. J. Roy. Meteorol. Soc., 138, 1794–1807, https://doi.org/10.1002/qj.1918, 2012.

Morcrette, C. J., O'Connor, E. J., and Petch, J. C.: Evaluation of two cloud parametrization schemes using ARM and CloudNet observations, Q. J. Roy. Meteorol. Soc., 138, 964–979, https://doi.org/10.1002/qj.969, 2014.

Morcrette, J.-J., Barker, H. W., Cole, J. N. S., Iacono, M. J., and Pincus, R.: Impact of a new radiation package, McRad, in the ECMWF Integrated Forecasting System, Mon. Weather Rev., 136, 4773–4798, https://doi.org/10.1175/2008MWR2363.1, 2008.

Morille, Y., Haeffelin, M., Drobinski, P., and Pelon, J.: STRAT: An automated algorithm to retrieve the vertical structure of the atmosphere from single-channel lidar data, J. Atmos. Ocean. Tech., 24, 761–775, https://doi.org/10.1175/JTECH2008.1, 2007.

Münkel, C., Eresmaa, N., Räsänen, J., and Karppinen, A.: Retrieval of mixing height and dust concentration with lidar ceilometer, Bound.-Lay. Meteorol., 124, 117–128, https://doi.org/10.1007/s10546-006-9103-3, 2007.

Müller, R., Pfeifroth, U., Träger-Chatterjee, C., Trentmann, J., and Cremer, R.: Digging the METEOSAT treasure – 3 decades of solar surface radiation, Remote Sens.-Basel, 7, 8067–8101, https://doi.org/10.3390/rs70608067, 2015.

Murphy, A. H.: Skill scores based on the mean square error and their relationships to the correlation coefficient, Mon. Weather Rev., 116, 2417–2424, https://doi.org/10.1175/1520-0493(1988)116<2417:SSBOTM>2.0.CO;2, 1988.

O'Connor, E. J., Illingworth, A. J., and Hogan, R. J.: A technique for autocalibration of cloud lidar, J. Atmos. Ocean. Tech., 21, 777–786, https://doi.org/10.1175/1520-0426(2004)021<0777:ATFAOC>2.0.CO;2, 2004.

Ohmura, A., Dutton, E. G., Forgan, B., Fröhlich, C., Gilgen, H., Hegner, H., Heimo, A., König-Langlo, G., McArthur, B., Müller, G., Philipona, R., Pinker, R., Whitlock, C. H., Dehne, K., and Wild, M.: Baseline Surface Radiation Network (BSRN/WCRP): New precision radiometry for climate research, B. Am. Meteor. Soc., 79, 2115–2136, https://doi.org/10.1175/1520-0477(1998)079<2115:BSRNBW>2.0.CO;2, 1998.

Posselt, R., Mueller, R., Stöckli, R., and Trentmann, J.: Remote sensing of solar surface radiation for climate monitoring – the CM-SAF retrieval in international comparison, Remote Sens. Environ., 118, 186–198, https://doi.org/10.1016/j.rse.2011.11.016, 2012.

Rontu, L. and Lindfors, A. V.: Comparison of radiation parametrizations within the HARMONIE–AROME NWP model, Adv. Sci. Res., 15, 81–90, https://doi.org/10.5194/asr-15-81-2018, 2018.

Urraca, R., Huld, T., Gracia-Amillo, A., de Pison, F. J. M., Kaspar, F., and Sanz-Garcia, A.: Evaluation of global horizontal irradiance estimates from ERA5 and COSMO-REA6 reanalyses using ground and satellite-based data, Sol. Energy, 164, 339–354, https://doi.org/10.1016/j.solener.2018.02.059, 2018.

Van Tricht, K., Gorodetskaya, I. V., Lhermitte, S., Turner, D. D., Schween, J. H., and Van Lipzig, N. P. M.: An improved algorithm for polar cloud-base detection by ceilometer over the ice sheets, Atmos. Meas. Tech., 7, 1153–1167, https://doi.org/10.5194/amt-7-1153-2014, 2014.

Van Weverberg, K., Morcrette, C. J., Petch, J., Klein, S. A., Ma, H.-Y., Zhang, C., Xie, S., Tang, Q., Gustafson, W. I., Qian, Y., Berg, L. K., Liu, Y., Huang, M., Ahlgrimm, M., Forbes, R., Bazile, E., Roehrig, R., Cole, J., Merryfield, W., Lee, W.-S., Cheruy, F., Mellul, L., Wang, Y.-C., Johnson, K., and Thieman, M. M.: CAUSES: Attribution of surface radiation biases in NWP and climate models near the U.S. Southern Great Plains, J. Geophys. Res.-Atmos., 123, 3612–3644, https://doi.org/10.1002/2017JD027188, 2018.

ILMATIETEEN LAITOS
METEOROLOGISKA INSTITUTET
FINNISH METEOROLOGICAL INSTITUTE

FINNISH METEOROLOGICAL INSTITUTE
Erik Palménin aukio 1
P.O. Box 503
FI-00560 HELSINKI
tel. +358 29 539 1000
WWW.FMI.FI

FINNISH METEOROLOGICAL INSTITUTE
CONTRIBUTIONS No. 155
ISSN 0782-6177
ISBN 978-952-336-082-2 (paperback)
ISBN 978-952-336-083-9 (pdf)
https://doi.org/10.35614/isbn.9789523360839

Edita Prima Oy
Helsinki 2019